

REPORT DOCUMENTATION PAGE		
Public reporting burden for this collection of information is estimated to average 1 hour per response, including the time for reviewing instructions, searching existing data sources, gathering and maintaining the data needed, and completing and reviewing this collection of information. Send comments regarding this burden estimate or any other aspect of this collection of information, including suggestions for reducing this burden to Department of Defense, Washington Headquarters Services, Directorate for Information Operations and Reports (0704-0188), 1215 Jefferson Davis Highway, Suite 1204, Arlington, VA 22202-4302. Respondents should be aware that notwithstanding any other provision of law, no person shall be subject to any penalty for failing to comply with a collection of information if it does not display a currently valid OMB control number. PLEASE DO NOT RETURN YOUR FORM TO THE ABOVE ADDRESS.		
1. REPORT DATE 28-02-2010	2. REPORT TYPE Final	3. DATES COVERED (From - To) 01-09-2006 – 28-02-2010
4. TITLE AND SUBTITLE High Temperature Oxidation of Superalloys and Intermetallic Compounds		5a. CONTRACT NUMBER N/A
		5b. GRANT NUMBER FA9550-06-1-525
		5c. PROGRAM ELEMENT NUMBER N/A
6. AUTHOR(S) A. Martinez-Villafañe, G. Vazquez-Olvera, A. Borunda Terrazas, V.M. Orozco-Carmona, J.M. Lugo-Cuevas, J. G. Chacon-Nava, C. Gaona-Tiburcio and F. Almeraya-Calderon		5d. PROJECT NUMBER N/A
		5e. TASK NUMBER N/A
		5f. WORK UNIT NUMBER N/A
7. PERFORMING ORGANIZATION NAME(S) AND ADDRESS(ES) AND ADDRESS(ES) Centro de Investigaciones en Materiales Avanzados S.C Miguel de Cervantes #120 , Complejo Industrial Chihuahua, Chihuahua, Chihuahua, Mexico ,CP 31109		8. PERFORMING ORGANIZATION REPORT NUMBER
9. SPONSORING / MONITORING AGENCY NAME(S) AND ADDRESS(ES) Air Force Office of Scientific Research (AFOSR) Latin American Initiative		10. SPONSOR/MONITOR'S ACRONYM(S) Dr. Jaimie Tiley AFOSR/NA Mr. James M. Fillerup ASFOR proposal Manager Joan Fuller ASFOR Deputy Director Directorate of aerospace chemistry and material sciences
		11. SPONSOR/MONITOR'S REPORT NUMBER(S)

20100316226

12. DISTRIBUTION / AVAILABILITY STATEMENT							
Only after publication of articles							
13. SUPPLEMENTARY NOTES							
14. ABSTRACT <p>Intermetallic aluminides are currently being considered for a variety of high temperature applications, i.e. gas turbine engines, fluidized bed combustors, in the aerospace, automotive and turbine power generation markets. Aircraft engine manufacturers are pursuing the implementation of these alloys in aircraft engines. This is because aluminides offer a possible combination of creep resistance and low density which is superior to that provided by state-of-the-art, coated superalloys. The long-range ordering in the lattice structure produces stronger bonding and closer packing between atoms mobility generally leads to slower diffusion processes and better creep resistance in ordered structure. Unlike conventional metallic alloys, the yield stress of most intermetallics increases substantially with the increasing temperature.</p> <p>The main conclusions reached in the present work provided a detailed comparison of oxidation performance of intermetallic aluminides with and without Nd and Pr in air at temperature range of 800–1100°C. The results based on specimen weight gain and microstructural characterizations indicated that Nd and Pr additions significantly improved the oxidation resistance of these alloys. The oxidation behaviors of an intermetallic aluminides in still air at 800, 900, 1000 and 1100°C followed a parabolic kinetic behavior. The kinetic constants for intermetallic aluminides without the addition of Nd and Pr were about twenty to fifty times higher than those with these elements regardless the temperature. Nd and Pr additions improved the adherence of the α-Al₂O₃ scale. The morphology of the oxides formed on specimens with and without REEs varies significantly from fine-grained, platelet-like and ridges-like to convoluted oxide.</p>							
15. SUBJECT TERMS Intermetallic alloys , high temperature oxidation, hot corrosion							
16. SECURITY CLASSIFICATION OF:			17. LIMITATION OF ABSTRACT	18. NUMBER OF PAGES <div style="text-align: center;">92</div>			
<table border="1" style="width: 100%; border-collapse: collapse;"> <tr> <td style="width: 33%; padding: 2px;">a. REPORT</td> <td style="width: 33%; padding: 2px;">b. ABSTRACT</td> <td style="width: 33%; padding: 2px;">c. THIS PAGE</td> </tr> </table>			a. REPORT	b. ABSTRACT	c. THIS PAGE		19a. NAME OF RESPONSIBLE PERSON Dr. Alberto Matinez-Villafane 19b. TELEPHONE NUMBER (include area code)+52(614)4391145
a. REPORT	b. ABSTRACT	c. THIS PAGE					

Standard Form 298 (Rev. 8-98)
Prescribed by ANSI Std. Z39.18



DEFENSE TECHNICAL INFORMATION CENTER

Information for the Defense Community

DTIC® has determined on 4/12/2018 that this Technical Document has the Distribution Statement checked below. The current distribution for this document can be found in the DTIC® Technical Report Database.

☒ **DISTRIBUTION STATEMENT A.** Approved for public release; distribution is unlimited. *per AFOSR*

☐ **© COPYRIGHTED;** U.S. Government or Federal Rights License. All other rights and uses except those permitted by copyright law are reserved by the copyright owner.

☐ **DISTRIBUTION STATEMENT B.** Distribution authorized to U.S. Government agencies only (fill in reason) (date of determination). Other requests for this document shall be referred to (insert controlling DoD office)

☐ **DISTRIBUTION STATEMENT C.** Distribution authorized to U.S. Government Agencies and their contractors (fill in reason) (date of determination). Other requests for this document shall be referred to (insert controlling DoD office)

☐ **DISTRIBUTION STATEMENT D.** Distribution authorized to the Department of Defense and U.S. DoD contractors only (fill in reason) (date of determination). Other requests shall be referred to (insert controlling DoD office).

☐ **DISTRIBUTION STATEMENT E.** Distribution authorized to DoD Components only (fill in reason) (date of determination). Other requests shall be referred to (insert controlling DoD office).

☐ **DISTRIBUTION STATEMENT F.** Further dissemination only as directed by (inserting controlling DoD office) (date of determination) or higher DoD authority.

Distribution Statement F is also used when a document does not contain a distribution statement and no distribution statement can be determined.

☐ **DISTRIBUTION STATEMENT X.** Distribution authorized to U.S. Government Agencies and private individuals or enterprises eligible to obtain export-controlled technical data in accordance with DoDD 5230.25; (date of determination). DoD Controlling Office is (insert controlling DoD office).

Index

Antecedents	4
Chapter 1.....	6
High temperature oxidation behavior of Fe ₃ Al and Fe ₃ AlNdPr intermetallic alloys	
Chapter 2.....	18
High temperature oxidation behavior of Ni ₃ Al and Ni ₃ AlNdPr intermetallic alloys	
Chapter 3.....	31
High temperature oxidation behavior of Ti ₃ Al and Ti ₃ AlNdPr intermetallic alloys	
Chapter 4.....	42
High temperature oxidation behavior of FeAl and FeAlNdPr intermetallic alloys	
Chapter 5.....	54
High temperature oxidation behavior of NiAl and NiAlNdPr intermetallic alloys	
Chapter 6.....	67
High temperature oxidation behavior of TiAl and TiAlNdPr intermetallic alloys	
Chapter 7.....	80
Corrosion behavior of alloy 718 in molten salts at high temperature	

High Temperature Oxidation of Superalloys and Intermetallic Compounds

A. Martinez-Villafañe, G. Vazquez-Olvera, A. Borunda Terrazas, V.M. Orozco-Carmona, J.M. Lugo-Cuevas, J. G. Chacon-Nava, C. Gaona-Tiburcio and F. Almeraya-Calderon.

Centro de Investigación en Materiales Avanzados. S.C. (CIMAV)
Miguel de Cervantes No. 120, Complejo Industrial Chihuahua
C. P. 31109. Chihuahua, Chih. Mexico.

Grant No.: FA9550-06-1-525

Intermetallic aluminides are currently being considered for a variety of high temperature applications, i.e. gas turbine engines, fluidized bed combustors, in the aerospace, automotive and turbine power generation markets. Aircraft engine manufacturers are pursuing the implementation of these alloys in aircraft engines. This is because aluminides offer a possible combination of creep resistance and low density which is superior to that provided by state-of-the-art, coated superalloys. The long-range ordering in the lattice structure produces stronger bonding and closer packing between atoms mobility generally leads to slower diffusion processes and better creep resistance in ordered structure. Unlike conventional metallic alloys, the yield stress of most intermetallics increases substantially with the increasing temperature.

Rare-earth elements were originally added to alloys as deoxidizers or, in the form of oxides, as high-temperature strengtheners. For more than 60 years, it has been known that the presence of rare-earth oxides (e.g. CeO_2) dispersed in alloys could also improve oxidation resistance and improve scale adherence. Similar beneficial effects on oxidation behavior have been observed for the addition of small amounts of rare-earth elements in Cr_2O_3 -forming and Al_2O_3 -forming alloys. Later, it was found that the addition of oxygen-active elements such as Y, Hf, Th, Zr, Nb and Ti or their stable oxides to metals and high-temperature alloys also improves oxidation resistance and scale adherence.

In the absence of reactive elements the major difference in the scale growth process between Cr_2O_3 is that, in the former, outward diffusion of chromium cations through oxide grain boundaries is considered to predominate at temperatures below 1000°C . However, in Al_2O_3 , grain boundary diffusion of oxygen is considered the fastest. In the present work the effect of rare earth elements (REE's) i.e. Neodymium (Nd) and Praseodymium (Pr) on the oxidation behavior of a aluminide intermetallic alloys with and without rare earths has been evaluated, and its role on the oxidation rate, oxide morphology and formation is discussed. Specimens were isothermally oxidized in air at 800, 900, 1000, and 1100°C for 48 h. It was found that a simultaneous addition ($\leq 0.03\text{wt.}\%$) of both Nd and Pr, reduced the oxidation rate of the intermetallic aluminides. Analysis by scanning electron microscopy (SEM) revealed that the morphology of oxides formed on intermetallic aluminides specimens with and without REE's was very

different. For these alloys mainly, aluminum enrichment at the metal/scale interface was observed.

The objective of this project was to analyze the high temperature oxidation behavior of superalloys and intermetallics compounds, to identify both detrimental and beneficial factors that influence adherence and spallation of the protective oxide, and to correlate these different factors. This should lead to a deeper insight into the complex processes occurring concurrently during high temperature oxidation, and conclusions that will help to improve actual material systems for applications beyond today limits.

A literature search was performed to determine which FeAl Rare Earth (RE), NiAlRE and TiAlRE intermetallic alloys would be used in this project. Corrosion resistance and spallation were the two confining variables, while alloy cost was also a consideration. Twelve intermetallic alloys were selected and starting with its manufacturing in an Arc Furnace.

FeAl
FeAlNdPr
Fe3Al
Fe3AlNdPr

NiAl
NiAlNdPr
Ni3Al
Ni3AlNdPr

TiAl
TiAlNdPr
Ti3Al
Ti3AlNdPr

The main conclusions reached in the present work provided a detailed comparison of oxidation performance of intermetallic aluminides with and without Nd and Pr in air at temperature range of 800–1100°C. The results based on specimen weight gain and microstructural characterizations indicated that Nd and Pr additions significantly improved the oxidation resistance of these alloys. The oxidation behaviors of an intermetallic aluminides in still air at 800, 900, 1000 and 1100°C followed a parabolic kinetic behavior. The kinetic constants for intermetallic aluminides without the addition of Nd and Pr were about twenty to fifty times higher than those with these elements regardless the temperature. Nd and Pr additions improved the adherence of the α -Al₂O₃ scale. The morphology of the oxides formed on specimens with and without REEs varies significantly from fine-grained, platelet-like and ridges-like to convoluted oxide.

The corrosion behavior in molten salts of Inconel 718 (IN 718) superalloy was investigated by Electrochemical Impedance Spectroscopy (EIS). The corrosion test temperatures used were salt melting points of Na₂SO₄, 80V₂O₅-20Na₂SO₄, NaVO₃ and natural ash (collected in a power plant). Different experimental runs were made attempting to establish the material behavior. The results showed that the corrosion process was controlled by activation and in some cases by diffusion. The aggressiveness of the salts increased with temperature, as indicated for the corrosion rates values derived. On the whole, the corrosion rates were somewhat similar at the lowest test temperatures. However at 588°C the 80V₂O₅-20Na₂SO₄ salt showed a much higher corrosion rate than that recorded for Na₂SO₄ or natural ash. The results obtained from electrochemical measurements correlated well with those corrosion degradation observed by SEM, and comments on the behavior found are made.

CHAPTER 1

HIGH TEMPERATURE OXIDATION BEHAVIOR OF Fe_3Al AND Fe_3AlNdPr INTERMETALLIC ALLOYS.

ABSTRACT

The effect of rare earth elements (REE's) i.e. Neodymium (Nd) and Praseodymium (Pr) on the oxidation behavior of a Fe_3Al intermetallic alloy with and without rare earths has been evaluated, and its role on the oxidation rate and oxide morphology and formation has been discussed. Specimens were isothermally oxidized in air at 800, 900, 1000, and 1100°C during 48 h. It was found that a simultaneous addition (≤ 0.03 wt.%) of both Nd and Pr, reduced the oxidation rate of the Fe_3Al intermetallic alloy. Analysis by scanning electron microscopy (SEM) revealed that the morphology of oxides formed on Fe_3Al intermetallic alloy specimens with and without REE's was very different. For these alloys mainly, aluminum enrichment at the metal/scale interface was observed.

INTRODUCTION

For more than 50 years, iron-aluminum intermetallic has received special interest because of their potentially high oxidation resistance at high temperature.[1] They offer a good alternative for use in automotive parts, chemical processing, and gas turbine technologies since they possess a high melting point, high thermal conductivity, excellent oxidation resistance, low density, and low cost.[2]

Iron aluminides, based around the stoichiometric compositions of Fe_3Al and FeAl , offer excellent resistance to oxidation and sulphidation at high temperatures, with low material cost and density than austenitic and ferritic stainless steels [3,4]. They contain enough aluminum to form a thin film of aluminum oxide (in oxidizing environments) that is often compact and protective. They possess relatively high specific strengths and suitable mechanical properties at elevated temperatures. They have, therefore, undergone extensive development, in the recent past, exclusively for high temperature applications. However, their potential use as structural materials at elevated temperatures has been hindered by limited ductility

at room temperature and sharp drop in strength above 600°C. It is well established that the poor room temperature ductility of iron aluminides is due to hydrogen embrittlement [5,6]. Considerable efforts have been devoted to understand and improve their mechanical properties

Iron aluminides are receiving special attention because they have a good yielding point between 600 and 800°C, and even up to 1000°C when they are alloyed with low expansion fibers such as alumina (Al_2O_3).[7] The charpy impact energy is satisfactory at room temperature, and, depending on the grain size, the FeAl(40 at.%) offers a yielding point between 250 and 600 MPa, which can be increased with additions of Hf or B.[8] Also, ingot iron aluminides have a lower density (5.6 g/cm^3) compared that for stainless steels and some nickel-based alloys, and a relatively high melting point (1237°C). Their main disadvantage is their poor ductility at room temperature. In the last few years, some new processing routes have been tried to improve their ductility [9] together with the addition of fibers and some microalloying elements.[10]

The good oxidation resistance of these materials is based on their ability to develop a protective alumina layer (Al_2O_3) on their surface in many high-temperature environments. Because alloys based on Fe_3Al and FeAl form Al_2O_3 during exposure to oxidizing gases, they typically display low oxidation rates when compared to iron-based and other alloys that do not form alumina in similar conditions. Recent studies on Fe_3Al alloys containing 2 to 5 at.% and various minor additions of oxygen-active elements have shown that their long-term oxidation performance approximately matches that of FeCrAlY alloys and NiAl at 1000°C, but it is inferior at 1200 and 1300°C.[11,12]

Another work has suggested that oxidation of iron aluminides without these oxygen-active elements is worse in air than in oxygen, particularly at 1000 and 1100°C, due to internal nitridation below a defective scale. The Fe_3Al alloys produced by ingot-metallurgy processes tended to have worse oxidation behavior,

since they had greater spallation than oxide-dispersion-strengthened iron aluminides of similar composition.[11] In this work, a study of the oxidation behavior of ingot-metallurgy processes iron aluminides in air has been carried out.

EXPERIMENTAL PROCEDURE

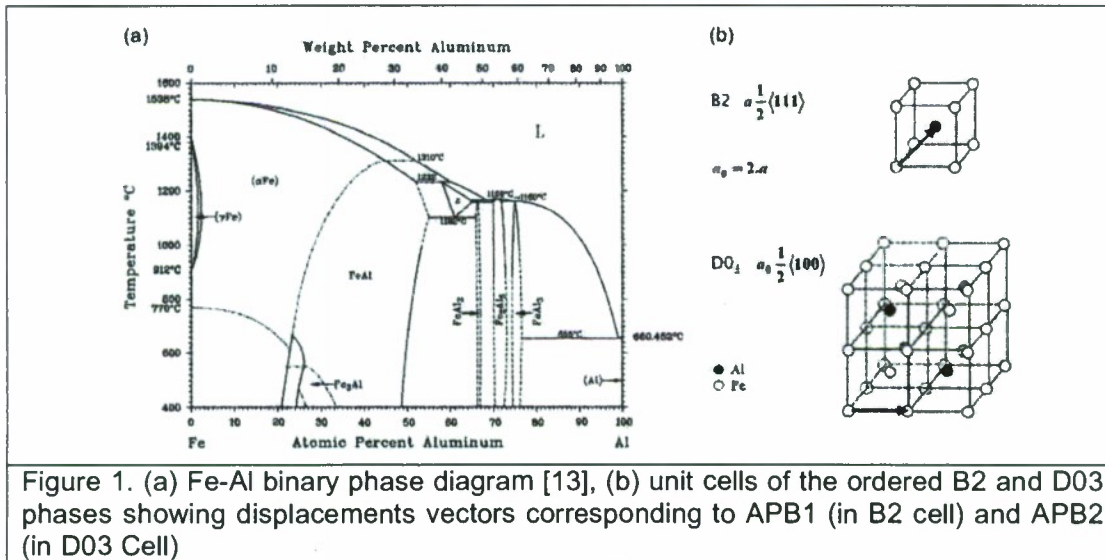
Fe-18wt.%Al (Fe_3Al) and Fe-18wt.%Al-0.01wt.%Nd-0.01wt.%Pr (Fe_3AlNdPr), intermetallic alloys were prepared from high purity Fe, Al, Nd and Pr elements (99.99%) in an electrical arc furnace using a purified argon atmosphere, from which rectangular strips of approximately 1.0 x 0.5 x 0.1 cm size were sectioned. The samples were cleaned and degreased. Afterwards, the surfaces were ground to 1200 grit paper, rinsed with distilled water and degreased with acetone. Each specimen was set on a platinum plate for weight-gain measurements in an electronic microbalance (sensitivity 10^{-6}g). Experiments were conducted in an atmosphere of air, a fixed temperature of 800, 900, 1000 and 1100°C ($\pm 2^\circ\text{C}$) and an exposure time of 48 h. The oxidized samples were analyzed using a scanning electron microscope (SEM-Jeol JSM-5800LV microscope) coupled with energy dispersive x-ray spectroscopy (EDS). These techniques are useful in understanding the oxidation phenomena in terms of scale morphology and distribution products.

RESULTS AND DISCUSSION

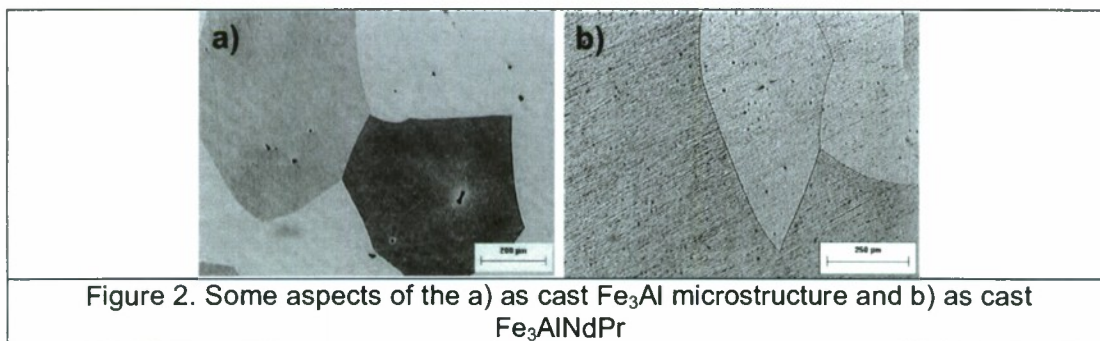
Structure and Microstructure

Iron aluminides exhibit ordered-disorder transformations and large concentrations of defects that depend upon both temperature and composition [13,14]. In the Fe-rich portion of the FeAl binary diagram exist the disordered A2 and the ordered B2 (FeAl) and D03 (Fe_3Al) phases [15], as shown in Fig. 1a. It is accepted since long that the ordering transformations begin with the formation of small ordered nuclei, which eventually grow until they occupy the entire volume of the crystal, resulting in an anti-phase domain structure that is usually characterized by transmission electron microscopy [16]. Different types of antiphase boundaries are present in the ordered alloys depending on their structure. In B2 ordered alloys only one type

of antiphase boundary is found, the B2-type APB (or APB1) that is formed through the A2→B2 ordering transformation and that has a fault vector $\frac{a}{2}\langle 111 \rangle$ (where a is the lattice parameter of the B2 unit cell). In ordered D0₃ two types of anti-phase boundaries can appear: the APB1 that forms as above, with a fault vector $\frac{a_0}{4}\langle 111 \rangle$ (where a_0 is the lattice parameter of the D0₃ unit cell) and the D0₃-type APB (or APB2) related to the B2→D0₃ transformation with a fault vector $\frac{a_0}{2}\langle 100 \rangle$ [17-20]. The unit cell and the fault vectors are shown in figure 1b.



Microstructural examination of the compact in the as-cast condition revealed a no homogeneous grain size distribution, Fig. 2, with an average size of about 400 and 300μm for as cast Fe₃Al and Fe₃AlNdPr respectively.



Kinetics

Figures 3 and 4 shows the weight gain per unit area against time for Fe₃Al and Fe₃AlNdPr respectively; in samples oxidized in air at 800, 900, 1000 and 1100°C

for a period of 48 hours. In all cases, a parabolic behavior was found and the rate constants derived for all temperatures are shown in table 1.

The kinetic results confirmed the beneficial effect of Nd-Pr addition on the oxidation behavior of the Fe_3Al intermetallic alloys. Thus, the weight change observed for Fe_3AlNdPr at 800, 900, 1000 and 1100°C was negligible (about 0.21, 0.31, 0.37 and 0.45 mg/cm^2 , respectively) as compared to that for Fe_3Al at 800, 900, 1000 and 1100°C (3.00, 6.60, 8.11 and 9.65 mg/cm^2 , respectively). Fe_3Al specimens showed cracking on the scale surface under exposition during 48 h. Regardless the temperature, the kinetic constants in this work were about twenty times lower for the alloys without the addition of Nd and Pr, on the oxidation behavior of Fe_3Al intermetallic alloys. Thus, according with the present results, the addition of Nd-Pr helped to decrease the oxidation kinetics, probably by avoiding massive diffusion of Al towards the intermetallic/environment interface. Values of k_p were calculated from plots of square weight-change data versus time. Activation energy for were determined from the plot of parabolic rate law constants (k_p) in an Arrhenius diagram. The weight gain per unit area as a function of time, i.e. ($\Delta W/A$) versus t , constituted the primary data and curves are shown in fig.3 and 4 for Fe_3Al and Fe_3AlNdPr respectively. The parabolic rate law was first considered as the basis of data processing and interpretation of results in this research work.

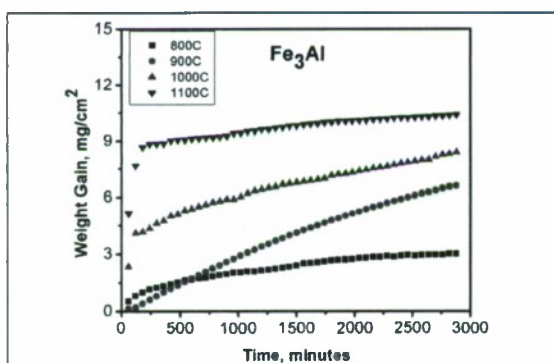


Fig.3. Kinetic data for the isothermal oxidation of Fe_3Al intermetallic alloy during oxidation at 800, 900, 1000 and 1100°C during 48h in air.

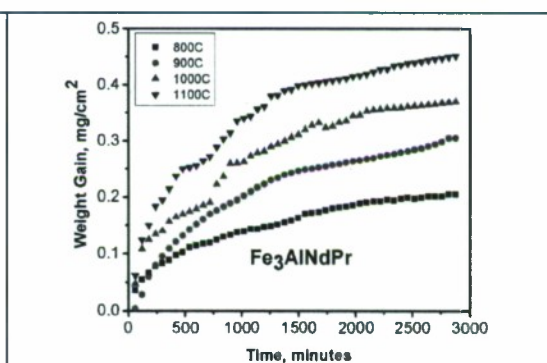


Fig.4. Kinetic data for the isothermal oxidation of Fe_3AlNdPr intermetallic alloy during oxidation at 800, 900, 1000 and 1100°C during 48h in air.

The parabolic rate constant (K_p) is related to the weight gain ($\Delta W/A$) and exposure time (t) by the following relation:

$$(\Delta W/A)^2 = K_p t + c \quad (1)$$

where c is a constant. The rate constant K_p was obtained from the slope of the linear regression-fitted line of $(\Delta W/A)^2$ vs t plot. The rate constants are provided in table 1 for the experiments performed in this study.

Table 1. Oxidation rate constant k_p of alloy at different temperatures

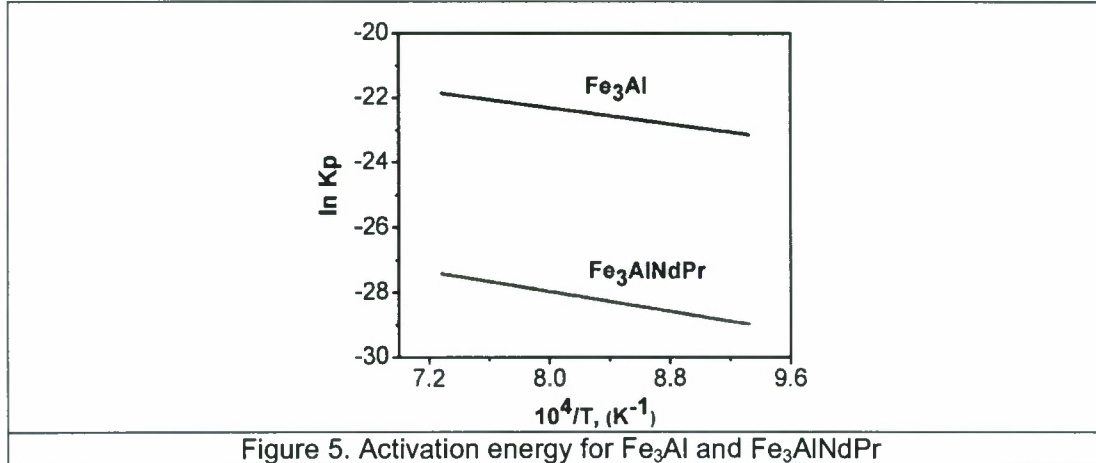
Intermetallic Alloys	$K_p, g^2cm^{-4}s^{-1}$	$K_p, g^2cm^{-4}s^{-1}$	$K_p, g^2cm^{-4}s^{-1}$	$K_p, g^2cm^{-4}s^{-1}$
	800°C	900°C	1000°C	1100°C
Fe ₃ Al	5.23×10^{-11}	2.78×10^{-10}	3.12×10^{-10}	1.70×10^{-10}
Fe ₃ AlNdPr	2.42×10^{-13}	5.33×10^{-13}	8.26×10^{-13}	1.15×10^{-12}

Fig. 5 shows the change in the experimentally determined values of K_p with the temperature for Fe₃Al and Fe₃AlNdPr intermetallic alloys respectively. It is a normal practice to correlate the overall parabolic rate constant (K_p) and temperature through an Arrhenius-type equation:

$$K_p = K_0 \exp(-Q/RT) \quad (2)$$

Where R is the universal gas constant, K_0 the pre-exponential factor. T is the absolute temperature and Q is the activation energy.

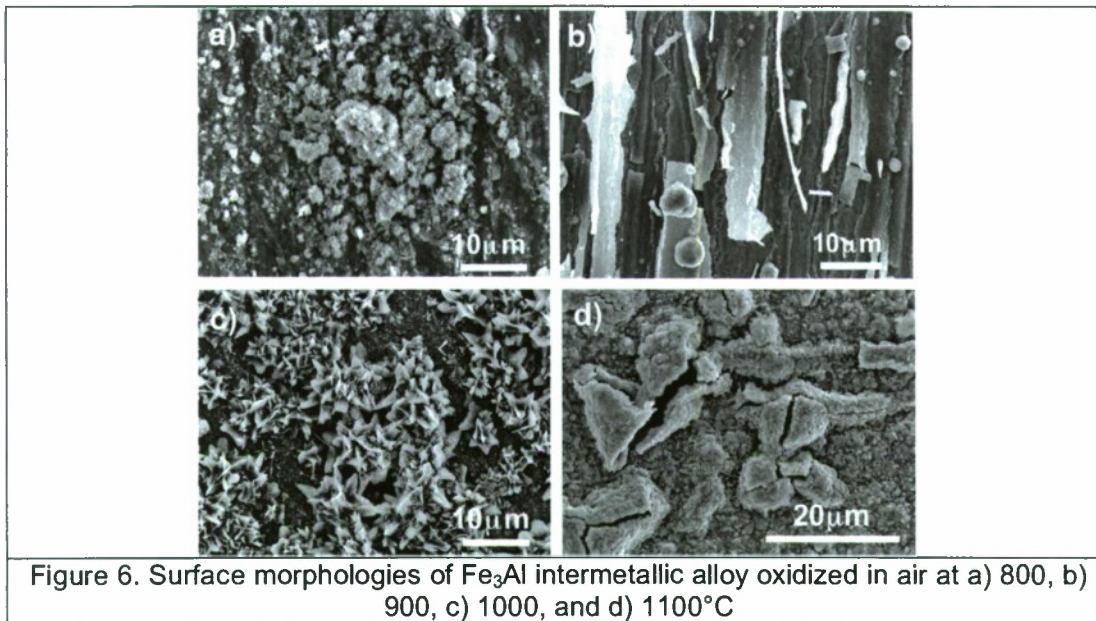
The activation energies for this system were $Q_{Fe_3Al}=52$ and $Q_{Fe_3AlNdPr}=63$ KJ/mol. The values appear somewhat different than the values generally obtained for alumina-formation kinetics around $250 kJmol^{-1}$ [21]. Babu et al. found an activation energy of 92 kJ/mol for oxidation kinetics of Fe₂₅Al [22]. The activation energy values collected from the present kinetics data are in agreement with Babu's values.



Morphology

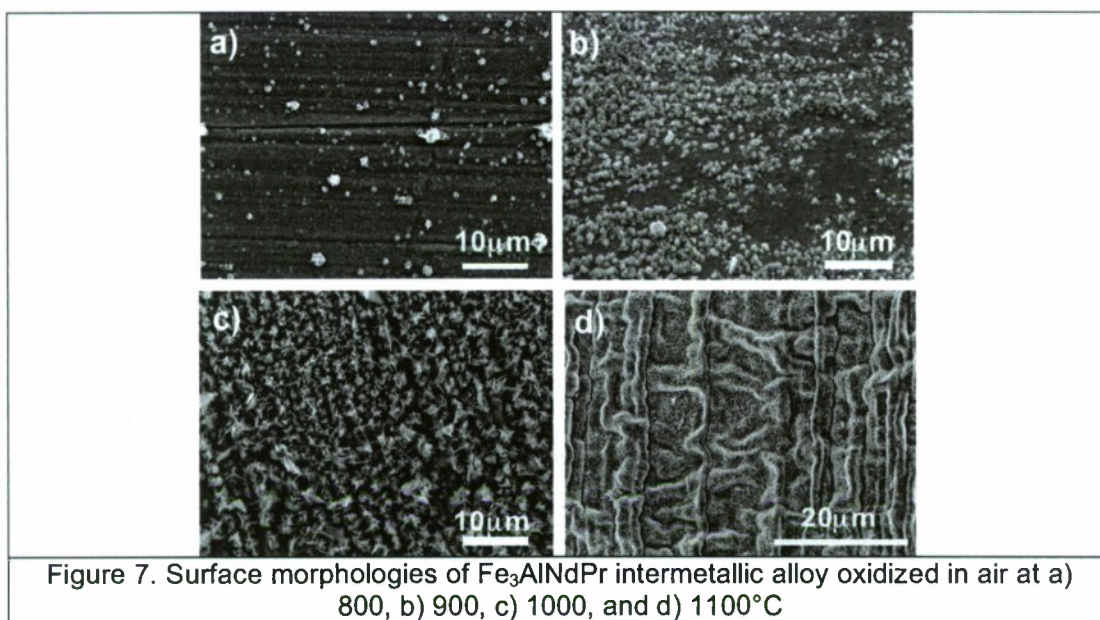
In the present study, it was clearly observed that the nature of the formed scale on the binary intermetallic alloy changed with temperature. This was also evident from morphological observations in the SEM after the Fe_3Al specimens had been oxidized during 48h (fig. 6), Spalling of scale was more pronounced at 900 and 1100°C oxidation temperatures. After oxidation at 800°C, the surface oxide morphology consisted mainly of granular oxides with some whiskers in a few places (fig. 6a) while, after 900°C oxidation spalling of scales was observed and some granular aluminum oxide were founded on the top surface. (fig.6b). At 1000°C the scale was covered with platelet-like oxides and at 1100°C was covered with convoluted oxides. Morphological observations of the oxide layers indicated that the poor oxidation resistance was mainly evidenced by scale failure, especially cracking and severe spallation.

Microalloying of REE's can significantly improve the oxidation resistance of Fe_3Al based alloy. Compared with REE's-free alloys, the oxidation rate of REE's-containing alloys was sharply reduced and slight spallation signs existed on the surfaces of oxide scales. Scales were sometimes granular, ridges-like (fig. 7a and b). At 1000°C the scale was covered with thin platelet-like oxides and at 1100°C was covered with fine convoluted oxides (Figs. 7c and d).



Comparing with others researchers results like Piotr Juzon et al. [23]. It can be confirm the complexity of the oxidation behavior of Fe_3Al intermetallics. They established that Zr addition improved the adherence of the $\alpha\text{-Al}_2\text{O}_3$ scale, while the pack cementation process increased the surface availability of aluminum. Moreover, it has been suggested that Zr-rich precipitates in the grain-boundary region of the alumina layer reduced the rate of scale growth by blocking the outward diffusion of Al cations. Fedotova et al.[24] pointed out that Fe_3Al oxidation was characterized by selective growth of very rough alumina layer containing only transient aluminum oxides. In addition to these transient oxides, $\alpha\text{-Al}_2\text{O}_3$ stable phase was formed at 1000°C. At the highest temperature (1100°C), continuous and relatively smooth alumina layer mainly contained fine crystallites of $\alpha\text{-Al}_2\text{O}_3$. The initial lamellar structure and phase inhomogeneity in as-Hipped Fe_3Al samples are supposed to be the main factors that determine observed peculiarities after Fe_3Al oxidation at 900 °C and 1000°C. B.A. Pint et al. [25]. The oxidation behavior of two iron aluminides was investigated in various environments at 900–1200°C. The effect of water vapor on total specimen mass gain was not significant. However, a Zr addition to Fe_3Al produced a lower mass gain than measured on undoped Fe_3Al . For one heat of undoped Fe_3Al at 1000 and 1100°C, there was a

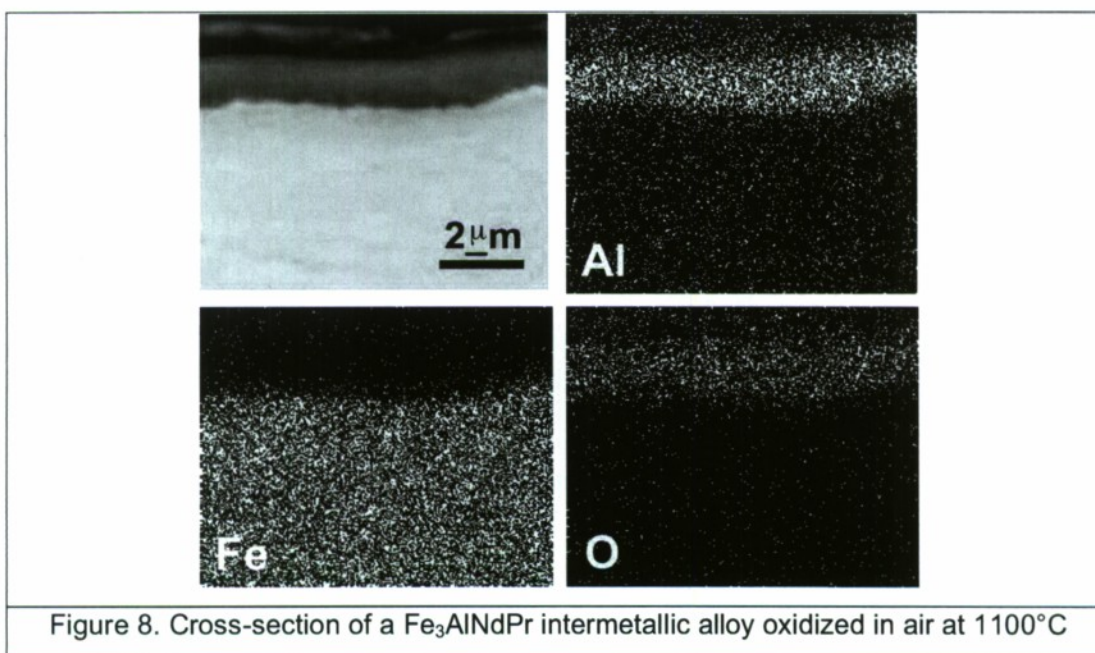
factor of 2 or more increase in mass gain in air compared to oxygen or Ar–20%O₂, but this effect was not reproduced in a second heat. Nitrogen appeared to accelerate the oxidation rate and aluminum nitrides were observed after these and other exposures.



According to Xinquan Yu et al. [26], the oxidation resistance of the binary Fe₃Al decreased rapidly as the temperature increased, above 1000°C. Morphological observations of the oxide layers indicate that the poor oxidation resistance is mainly manifested by scale failure, especially cracking and severe spallation. Microalloying of REE's can improve the oxidation resistance of Fe₃Al based alloy significantly. Compared with REE's-free alloys, the oxidation rate of REE's-containing alloys was sharply reduced and slight spallation signs existed on the surfaces of oxide scales. Scales are sometimes smooth and convoluted at 1100°C during 48 h (figure 7d).

Iron aluminides depend on the formation of an alumina scale for their oxidation and corrosion resistance. At low concentrations of Al, internal oxidation of Al occurs and Fe₂O₃ and Fe₃O₄ form on the exterior of the alloys. At intermediate Al

concentrations, although a transient alumina layer is formed, it tends to be disrupted by iron nodules. Approximately 15 at% Al must be added to Fe to produce a continuous layer of Al_2O_3 during oxidation. Small Cr additions reduce the aluminum requirement, but Ni additions require increased amounts of Al to avoid the formation of nodules of Fe-rich oxides that disrupt the alumina scale. In fig.8 is shown the cross-section of a Fe_3AlNdPr intermetallic alloy oxidized in air at 1100°C , as we can see a compact and continuous alumina scale was formed on the surface at this temperature and no internal oxidation or void formation were observed.



CONCLUSIONS

The present work provided a detailed comparison of oxidation performance of Fe_3Al with and without Nd and Pr in air in the temperature range of $800\text{--}1100^\circ\text{C}$. The results based on specimen weight gain and microstructural characterizations indicated that Nd and Pr additions significantly improved the oxidation resistance of these alloys.

The oxidation behavior of a Fe₃Al and Fe₃AlNdPr intermetallic alloys in still air at 800, 900, 1000 and 1100°C followed a parabolic kinetic behavior.

The kinetic constants for Fe₃Al intermetallic alloys without the addition of Nd and Pr were about twenty times higher than those with these elements regardless the temperature.

The activation energies for this system were $Q_{\text{Fe}_3\text{Al}}=52$ and $Q_{\text{Fe}_3\text{AlNdPr}}=63$ KJ/mol

Nd and Pr additions improved the adherence of the $\alpha\text{-Al}_2\text{O}_3$ scale.

The morphology of the oxides formed on specimens with and without REEs varies significantly from fine-grained, platelet-like and ridges-like to convoluted oxide.

REFERENCES

1. C. Sykes and J. Bampfyld: *J. Iron Steel Inst.*, 1934, vol. 130, pp.389-418.
2. G. Webband and A. Lefort: *Symp. Proc. Fatigue and Fracture of Ordered Intermetallic Materials: I*, TMS, Warrandale, PA, 1994, p.103.
3. C.T. Liu, J.O. Stiegler, F.H. Froes, *Ordered intermetallics*, 10th ed. *Metals Handbook*, vol. 2, ASM, Metals Park, USA, 1990, pp. 913–943.
4. C.T. Liu, K.S. Kumar, *Ordered intermetallic alloys*, part 1, nickel and iron aluminides, *J. Metals* 45(1993) 38–44.
5. C.T. Liu, C.G. McKamey, E.H. Lee, Environmental effects on room temperature ductility and fracture mode in Fe₃Al alloys, *Scripta Metall.* 24 (1990) 385–390.
6. C.T. Liu, C.G. McKamey, E.H. Lee, An environmental effect as the major cause room temperature embrittlement in FeAl, *Scripta Metall.* 23 (1996) 875–880.
7. J.L. Smialek, J. Doychak, and D.J. Gaydosh: in *Oxidation of High-Temperature Intermetallics*, T. Grobstein and J. Doychak, eds., TMS, Warrandale, PA, 1989, p. 83.
8. J.H. Schneibel: *Mater. Sci. Eng.*, 1992, vol. A153, p. 684.
9. S. Zeng, X.R. Nutt, and E.J. Lavernia: *Metall. Mater. Trans.*, 1994, vol. A26, p. 817.
10. R.G. Baligidad, U. Prakash, and A. Radha Krishna: *Mater. Sci. Eng.*, 1997, vol. A230, p. 188.
11. B.A. Pint, P.F. Tortorelli, and I.G. Wright: *Mater. Corr.*, 1996, vol.47, pp. 663-74.
12. B.A. Pint, P.F. Tortorelli, and I.G. Wright: *Mater. High Temp.*, 1997, vol. 15, p. 613.
13. Morris MA, George O, Morris DG. *Mater Sci Eng* 1998; A258:99.

14. Inden G, Pepperhoff W. *Z Metallkd* 1990; 81:770.
15. Binary alloys phase diagrams. 2nd ed. ASM International; 1996. On CD Rom.
16. Marcinkowski MJ, Brown N. *J Appl Phys* 1962; 33:537.
17. Karlık M. *Mater Sci Eng* 1997; A234-236:212.
18. Liu W, Rosner H, Langmaack E, Gemperle A, Gemperlova J, Pesicka J, et al. *Mater Sci Eng* 1998; A258:15.
19. Yoshimi K, Hanada S, Onuma T, Yoo MH. *Phil Mag A* 1996; 73:443.
20. Morris DG, Requejo LM, Muñoz-Morris MA. *Intermetallics* 2005; 13:862.
21. I. G. Wright, B. A. Pint, and P. F. Tortorelli, *Oxidation of Metals* 55, 333 (2001).
22. N. Babu, R. Balasubramaniam, A. Ghosh. *High Temperature Oxidation of Fe₃Al-based iron aluminides in oxygen. Corrosion Science* 43 (2001) 2239–2254.
23. Piotr Juzon, Marta Ziemnicka, Sebastien Chevalier, Kazimierz Przybylski, Jean Pierre Larpin. Improving Fe₃Al alloy resistance against high temperature oxidation by pack cementation process. *Applied Surface Science* 253 (2007) 4928–4934.
24. J. Fedotova, G. Bonnet, F. Pedraza, J. Balmain, S. Dubois, V. Gauthier, M.F. Denanot, N. Ouabadi, A. Letsko, A. Ilyuschenko, A. Akimov. Effect of lamellar microstructure on oxidation kinetics of Fe₃Al sintered by hot isostatic pressing. *Corrosion Science* 50 (2008) 1693–1700.
25. B.A. Pint, J.R. Regina, K. Prubner, L.D. Chitwood, K.B. Alexander. P.F. Tortorelli. Effect of environment on the oxidation of ingot-processed iron aluminides. *Intermetallics* 9 (2001) 735–739.
26. Xinquan Yu, Yangshan Sun. The oxidation improvement of Fe₃Al based alloy with cerium addition at temperature above 1000°C. *Materials Science and Engineering. A363* (2003) 30–39.

CHAPTER 2

HIGH TEMPERATURE OXIDATION BEHAVIOR OF Ni_3Al AND Ni_3AlNdPr INTERMETALLIC ALLOYS.

ABSTRACT

The influence of rare earth elements (REE's) i.e. Neodymium (Nd) and Praseodymium (Pr) on the oxidation behavior of a Ni_3Al intermetallic alloy with and without rare earths has been evaluated, and its role on the oxidation rate and oxide morphology and formation has been discussed. Specimens were isothermally oxidized in air at 800, 900, 1000, and 1100°C during 48 h. It was found that a simultaneous addition (≤ 0.03 wt.%) of both Nd and Pr, reduced the oxidation rate of the Ni_3Al intermetallic alloy. Analysis by scanning electronic microscope (SEM) revealed that the morphology of oxides formed on Ni_3Al intermetallic alloy specimens with and without REE's was very different. For these alloys mainly, aluminum enrichment at the metal/scale interface was observed.

INTRODUCTION

Intermetallic compounds such as nickel aluminides (Ni_3Al and NiAl), iron aluminides (FeAl , and Fe_3Al) and titanium aluminides (TiAl and Ti_3Al) are a class of advanced materials with considerable potential for low and high-temperature application [1–4]. Processing approaches for aluminides include casting, thermomechanical and powder processing of pre-alloyed powder [5]. Because of the potential use of nickel aluminides at high temperatures, it is imperative to understand and study of their oxidation behavior. It was reported that the types of scale (oxide or mixture of oxides) and scale morphology formed on the surface of the alloy during high-temperature oxidation were influenced by both the compositions of the gas and the alloy as well as the reaction temperature [6]. Both thermodynamic and kinetic factors should be considered to understand this complex oxidation process. Thermodynamics governs and predicts the type of oxide that can form under the operating conditions, and for nickel aluminides, the formation of alumina (Al_2O_3), nickel oxide (NiO), and nickel aluminate (NiAl_2O_4)

have been reported to compete with one another, depending on which one is more thermodynamically stable to form at the operating temperature [7–10].

For many years, nickel-aluminum intermetallic has received special interest because of their potentially high oxidation resistance at high temperature. They offer a good alternative for use in automotive parts, chemical processing, and gas turbine technologies since they possess a high melting point, high thermal conductivity, excellent oxidation resistance, low density, and low cost. Other work has suggested that oxidation of nickel aluminides without these oxygen-active elements is worse in air than oxygen, particularly at 1000 and 1100°C, due to internal nitridation below a defective scale. The Ni₃Al alloys produced by ingot-metallurgy processes tended to have worse oxidation behavior, since they had greater spallation than oxide-dispersion-strengthened nickel aluminides of similar composition.[11] Rare-earth elements were originally added to alloys as deoxidizers or, in the form of oxides, as high-temperature strengtheners. For more than 60 years, it has been known that the presence of rare-earth oxides (e.g. CeO₂) dispersed in alloys could also improve oxidation resistance and improve scale adherence. Similar beneficial effects on oxidation behavior have been observed for the addition of small amounts of rare-earth elements in Cr₂O₃ and Al₂O₃ forming alloys. Later, it was found that the addition of oxygen-active elements such as Y, Hf, Th, Zr, Nb and Ti or their stable oxides to metals and high-temperature alloys also improves oxidation resistance and scale adherence.[12] In this work, a study of the oxidation behavior of ingot-metallurgy processes of nickel aluminides with and without Nd plus Pr, in air has been carried out.

EXPERIMENTAL PROCEDURE

Ni-13wt.%Al (Ni₃Al) and Ni-13wt.%Al-0.01wt.%Nd-0.01wt.%Pr (Ni₃AlNdPr), intermetallic ingots were produced by a standard electrical arc furnace with a purified argon atmosphere using high pure Ni, Al, Nd and Pr metals (99.99%). Coupons with the dimensions of 1.0 x 0.5 x 0.1 cm size were sectioned from the cast ingot. The samples were cleaned and degreased. Afterwards, the surfaces

were ground to 1200 grit paper, rinsed with distilled water and degreased with acetone. Each specimen was set on a platinum plate for weight-gain measurements in an electronic microbalance (sensitivity 10^{-6} g). Experiments were conducted in an atmosphere of air, a fixed temperature of 800, 900, 1000 and 1100°C ($\pm 2^{\circ}\text{C}$) and an exposure time of 48 h. The oxidized samples were analyzed using a scanning electron microscope (SEM-Jeol JSM-5800LV microscope) coupled with energy dispersive x-ray spectroscopy (EDS). These techniques are useful in understanding the oxidation phenomena in terms of scale morphology and distribution products.

RESULTS AND DISCUSSION

Structure and Microstructure

In the Ni-Al alloy system, as the Al content is varied, other phases in addition to the γ , γ' , and β appear. A map of all of these phases formed as a function of composition and temperature is called the (equilibrium) phase diagram, shown in Fig. 1. [13] Equilibrium here refers to the fact that the phases in the map remain stable over time when held at appropriate temperatures. Because the diagram shown here describes an alloy of two components only, Ni and Al, it is called a binary phase diagram. The two phases bounding the diagram (in this case face center cubic (fcc) Al and Ni) are called the terminal phases.

Ni crystallizes in a fcc structure. If we alloy Ni by adding Al, several significant changes occur. For up to about 4wt%Al, there is no change in the atomic arrangement of Ni except an occasional Al atom replacing a Ni atom randomly, as in Fig. 2(a). The structure remains essentially like fcc Ni, called the γ phase. As the Al content is increased, it starts selectively replacing the corner atoms (Fig. 2(b)), while the atoms on the cube faces remain Ni. The share of atoms for each cell is 1 Al and 3 Ni, giving the composition Ni_3Al , which is known as the γ' phase. If the alloying addition is continued, eventually at about 25 wt%Al, the crystal structure changes so that the corner atoms remain Ni, while Al enters the center of the cube. The central Al atom belongs to this cell, while the corner atoms are each shared

with eight cells. The overall share is therefore 1 Al and 1 Ni, providing the composition of NiAl, known as the β phase, Fig. 2(c).

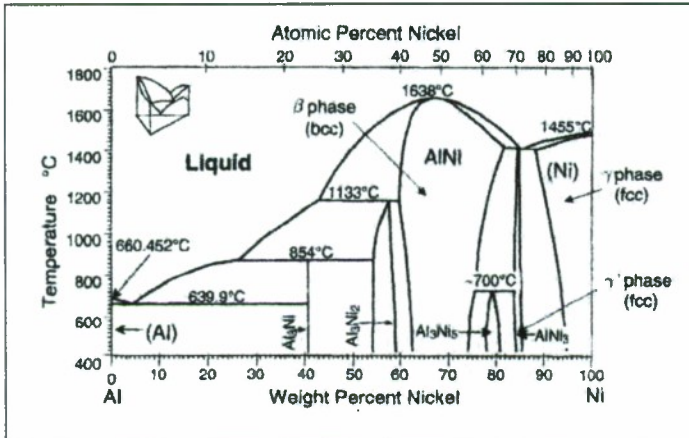


Figure 1. Ni-Al phase diagram. 2nd ed. ASM International; 1996.)

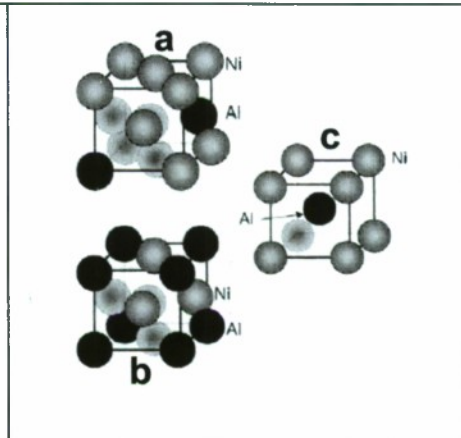


Figure 2. Effect of alloying on crystal structure

Microstructural examination of the compact in the as-cast condition revealed an no homogeneous grain size distribution, Fig. 3, with an average size of about 200 and 100 μ m for as cast Ni₃Al and Ni₃AlNdPr respectively.

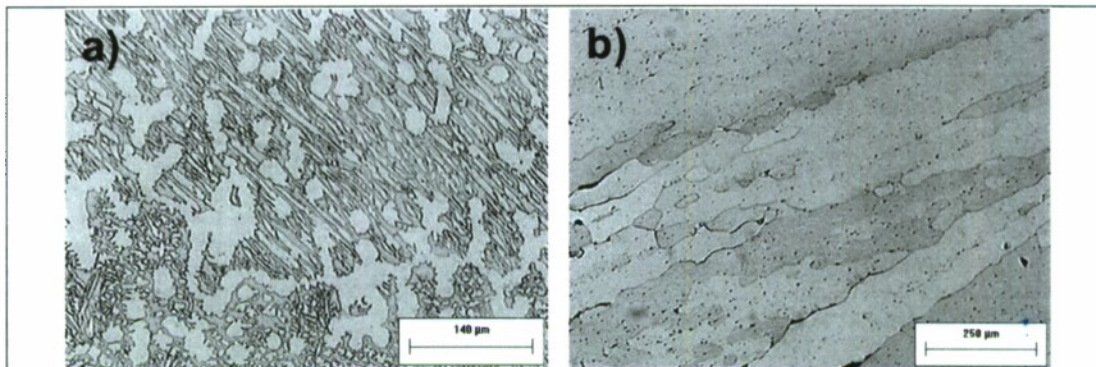


Figure 3. Some aspects of the a) as cast Ni₃Al microstructure and b) as cast Ni₃AlNdPr microstructure

Kinetics

Figures 4 and 5 shows the weight gain per unit area against time for Ni₃Al and Ni₃AlNdPr respectively; in samples oxidized in air at 800, 900, 1000 and 1100°C for a period of 48 hours. In all cases, a parabolic behavior was found and the rate constants derived for all temperatures are shown in table 1.

The kinetic results confirmed the beneficial effect of Nd-Pr addition on the oxidation behavior of the Ni_3Al intermetallic alloys. Thus, the weight change observed for Ni_3AlNdPr at 800, 900, 1000 and 1100°C was negligible (about 0.25, 0.33, 0.41 and 0.48 mg/cm^2 , respectively) as compared to that for Ni_3Al at 800, 900, 1000 and 1100°C (2.15, 4.59, 8.90 and 11.83 mg/cm^2 , respectively). Ni_3Al specimens showed cracking on the scale surface under exposition during 48 h. Regardless the temperature, the kinetic constants in this work were about thirty times lower for the alloys without the addition of Nd and Pr, on the oxidation behavior of Ni_3Al intermetallic alloys. Thus, according with the present results, the addition of Nd-Pr helped to decrease the oxidation kinetics, probably by avoiding massive diffusion of Al towards the intermetallic/environment interface. Values of k_p were calculated from plots of square weight-change data versus time. Activation energy for were determined from the plot of parabolic rate law constants (k_p) in an Arrhenius diagram. The weight gain per unit area as a function of time, i.e. ($\Delta W/A$) versus t , constituted the primary data and curves are shown in fig.4 and 5 for Ni_3Al and Ni_3AlNdPr respectively. The parabolic rate law was first considered as the basis of data processing and interpretation of results in this research work.

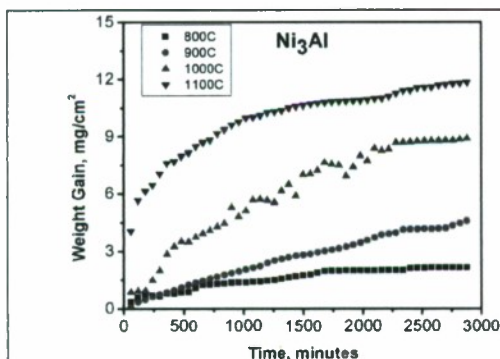


Fig.4. Kinetic data for the isothermal oxidation of Ni_3Al intermetallic alloy during oxidation in air at 800, 900, 1000 and 1100°C during 48h.

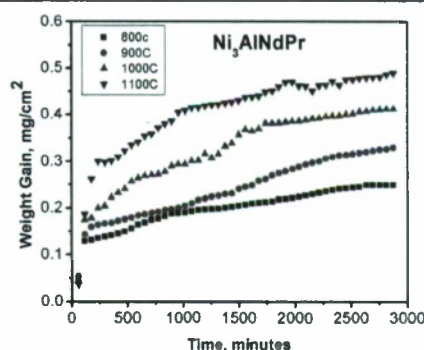


Fig.5. Kinetic data for the isothermal oxidation of Ni_3AlNdPr intermetallic alloy during oxidation in air at 800, 900, 1000 and 1100°C during 48h.

The parabolic rate constant (K_p) is related to the weight gain ($\Delta W/A$) and exposure time (t) by the following relation:

$$(\Delta W/A)^2 = K_p t + c \quad (1)$$

where c is a constant. The rate constant K_p was obtained from the slope of the linear regression-fitted line of $(\Delta W/A)^2$ vs t plot. The rate constants are provided in table 1 for the experiments performed in this study.

Table 1. Oxidation rate constant k_p of Ni_3Al and $Ni_3AlNdPr$ intermetallic alloy at different temperatures

Intermetallic Alloys	$K_p, g^2cm^{-4}s^{-1}$	$K_p, g^2cm^{-4}s^{-1}$	$K_p, g^2cm^{-4}s^{-1}$	$K_p, g^2cm^{-4}s^{-1}$
	800°C	900°C	1000°C	1100°C
Ni_3Al	2.90×10^{-11}	1.29×10^{-10}	5.28×10^{-10}	6.28×10^{-10}
$Ni_3AlNdPr$	4.47×10^{-13}	5.62×10^{-13}	6.45×10^{-13}	9.22×10^{-13}

Fig. 6 shows the change in the experimentally determined values of K_p with the temperature for Ni_3Al and $Ni_3AlNdPr$ intermetallic alloys respectively. It is a normal practice to correlate the overall parabolic rate constant (K_p) and temperature through an Arrhenius-type equation:

$$K_p = K_0 \exp(-Q/RT) \quad (2)$$

Where R is the universal gas constant, K_0 the pre-exponential factor. T is the absolute temperature and Q is the activation energy.

The activation energies for this system were $Q_{Ni_3Al}=132$ and $Q_{Ni_3AlNdPr}=28$ KJ/mol. Babu et al. found an activation energy of 92 kJ/mol for oxidation kinetics of Fe25Al [14]. The activation energy values collected from the present kinetics data are in agreement with Babu's values.

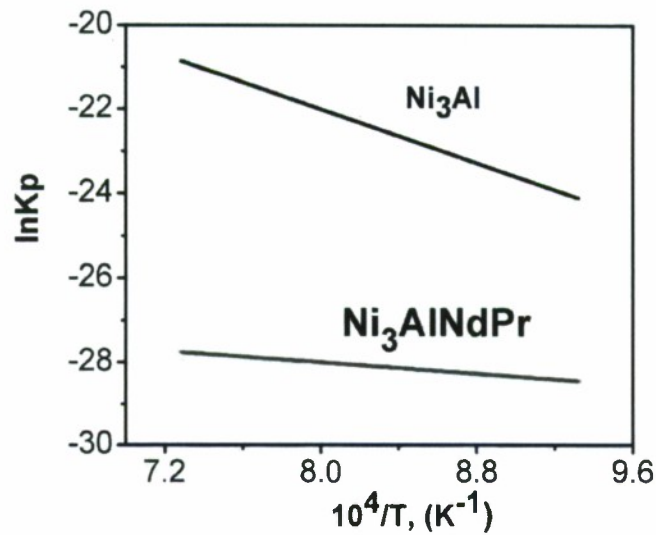
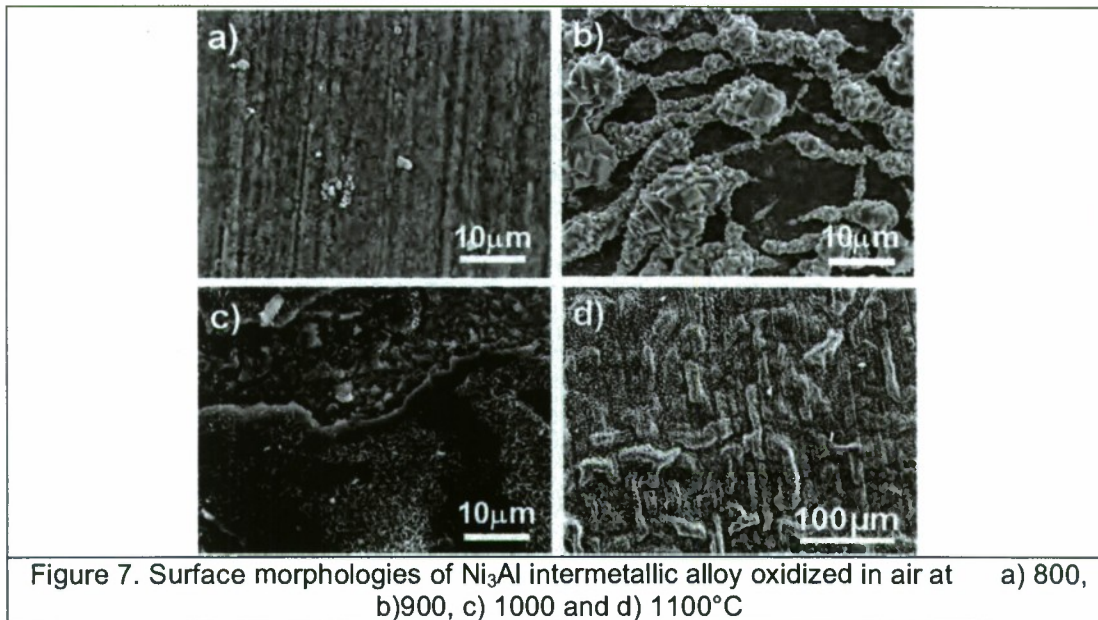


Figure 6. Activation energy for Ni_3Al and $Ni_3AlNdPr$ intermetallic alloys

Morphology

In the present study, it was clearly observed that the nature of the formed scale on the binary intermetallic changed with temperature. This was also evident from morphological observations in the SEM after the Ni_3Al specimens had been oxidized during 48h (fig. 7), Spalling of scale was more pronounced at the lower oxidation temperatures. After oxidation at 800C, the surface oxide morphology consisted mainly of granular oxides (fig. 7a) while, after 900°C oxidation crystal chains-like scales (extrinsic ridges structure) were observed. (fig.7b), at 1000°C oxidation spalling of scales was observed and some plate-like aluminum oxide were founded on the top surface (fig.7c) and convoluted morphology during oxidation at 1100°C for 48 h (fig. 7d). Morphological observations of the oxide layers indicated that the poor oxidation resistance was mainly evidenced by scale failure, especially cracking and severe spallation.



Microalloying of REE's can significantly improve the oxidation resistance of Ni_3Al based alloy. Compared with REE's-free alloys, the oxidation rate of REE's-containing alloys was sharply reduced and slight spallation signs existed on the surfaces of oxide scales. Scales were sometimes granular, ridges-like (fig. 8a, b and c) and convoluted during oxidation at 1100°C for 48 h (fig. 8d). To understand the function of microalloying constituents during the growth of oxide scales, extensive studies have been conducted by many researchers. Graboski and Rehin [15] summarized oxidation behavior of metals and alloys implanted with various elements. They have found that only implanted yttrium has significant beneficial effects on oxidation resistance. Some beneficial effects of additions of Y, Ce, Hf, Y_2O_3 , HfO_2 , and CeO_2 on the development of protective oxide scales were founded by using surface salt-deposit techniques [16] and conventional alloying techniques. [17-22] Some other reactive elements, such as Th, Zr and La, also showed some influence on oxidation behavior; however, only a few studies were conducted on those elements.

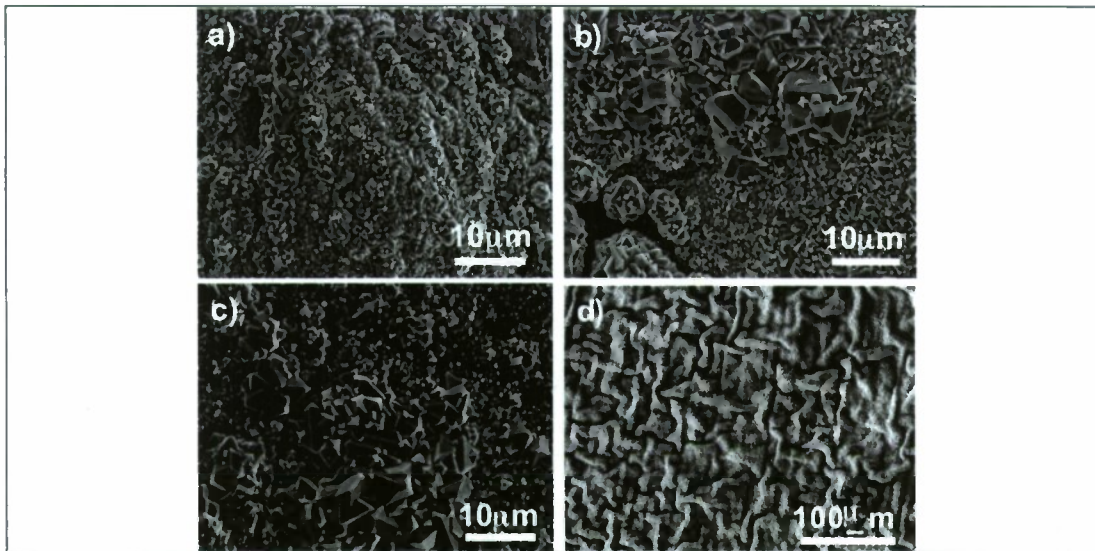


Figure 8. Surface morphologies of Ni_3AlNdPr intermetallic alloy oxidized in air at a) 800, b) 900, c) 1000 and d) 1100°C

In fig. 9 is also shown the backscattered image of the cross-section of Ni_3Al intermetallic alloy oxidized in air at 1100°C during 48h with X-ray maps of Al, Ni and O.

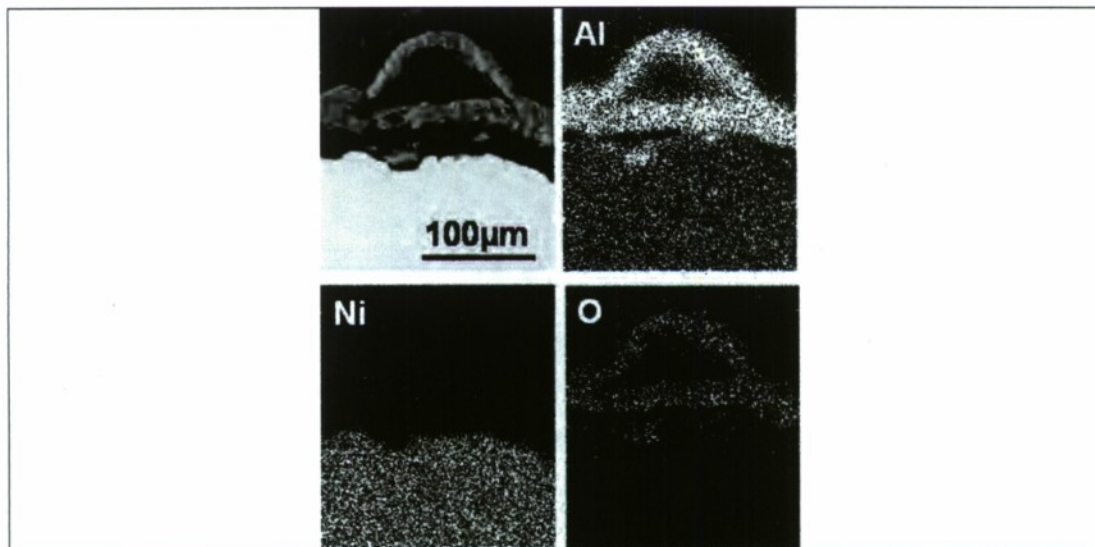
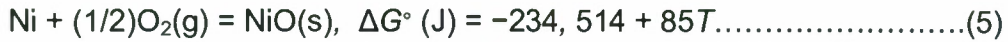
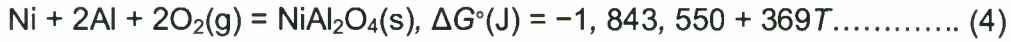
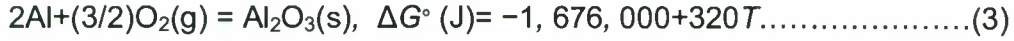


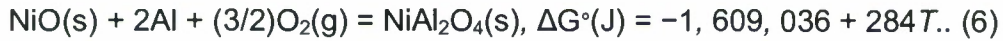
Figure 9. cross-section general view of Ni_3Al alloy oxidized in air at 1100°C during 48h with X-ray maps of Al, Ni and O

There are several potential oxidation reactions, when Ni–Al alloys are kept in oxygen-containing environments at elevated temperatures. The formations of these

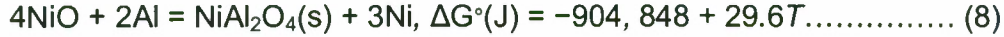
oxides (Al_2O_3 , NiO , and NiAl_2O_4) are governed by their free energies of formation ' ΔG° '; the following reactions are possible [21]:



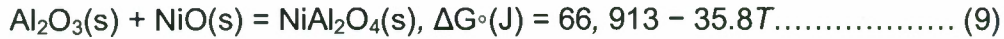
Eqs. (3) and (4) may combine to:



As the oxidation process continues, equilibrium between the alloy surface and the oxide phase is approached and the stability of the oxide nuclei determined by the composition of the alloy at the alloy/oxide interface is based on the following reactions [7]:



Combining Eqs. (7) and (8), we have:



The more negative the free energy of a given oxidation reaction the more spontaneous the reaction will be and the oxide phase resulting from this reaction is said to be more thermodynamically stable. Al_2O_3 and NiAl_2O_4 are considered the most stable oxide phases from the thermodynamic point of view. The alumina may form as a result of an oxidation reaction between Al atoms already present at the surface or diffuses across an existing oxide layer to react with O_2 gas at the oxide–gas interface. The NiAl_2O_4 may result from either the oxidation reaction between Ni and Al or Al and NiO already formed at the surface with the O_2 gas, respectively. Also, the positive ΔG° of NiAl_2O_4 resulting from the chemical reaction between NiO and Al_2O_3 suggest that NiAl_2O_4 would decompose to NiO and Al_2O_3 spontaneously [7].

The morphological observations and microanalyses suggest that Nd plus Pr have an effect on prevention of outward diffusion of cations through the short-circuit paths during oxidation, which prevents cavities forming near substrate–oxide interface, so that the alloy shows a dramatic improvement in scale adhesion. Nd and Pr addition can refine the oxide grains and reduce the formation of nickel or spinel oxides in the alumina scale.

CONCLUSIONS

The present work provided a detailed comparison of the oxidation performance of Ni_3Al with and without Nd and Pr in air in the temperature range of 800–1100°C. The results based on specimen weight gain and microstructural characterizations indicated that Nd and Pr additions significantly improved the oxidation resistance of these alloys.

The oxidation behavior of a Ni_3Al and Ni_3AlNdPr intermetallic alloys in static air at 800, 900, 1000 and 1100°C followed a parabolic kinetic behavior.

The kinetic constants for Ni_3Al intermetallic alloys without the addition of Nd and Pr were about thirty times higher than those with these elements regardless the temperature.

The activation energies for this system were $Q_{\text{Ni}_3\text{Al}} = 132$ and $Q_{\text{Ni}_3\text{AlNdPr}} = 28$ KJ/mol

Nd and Pr additions improved the adherence of the $\alpha\text{-Al}_2\text{O}_3$ scale.

The morphology of the oxides formed on specimens with and without REEs varies significantly from fine-grained, plate-like and ridges-like to convoluted oxide.

REFERENCES

1. V.K. Sikka, M.L. Santella, J.E. Orth, *Mater. Sci. Eng. A* 239–240 (1997) 564–569.
2. V. Shankar Rao, *J. Mater. Sci.* (2004) 4193–4198.
3. D. Zhang, Z. Cai, G. Adam, S. Raynova, Z. Liu, *J. Met.* 56 (2004) 271.
4. J. Lapin, M. Nazmy, *Mater. Sci. Eng. A* 380 (2004) 298–307.
5. S. Deevi, V. Sikka, *Proceeding of the International Symposium on Nickel and Iron Aluminides: Processing, Properties and Applications*, 1997, p.283.
6. J. Gawel, *Oxid. Met.* 30 (3/4) (1988) 139–140.
7. W.H. Lee, R.Y. Lin, *Mater. Chem. Phys.* 77 (2002) 86.
8. K. Natesan, F. Tortorelli, High-temperature corrosion and applications of nickel and iron aluminides in coal-conversion power systems, in: *Proceedings of the International Symposium on Nickel and Iron Aluminides: Processing, Properties, and Applications*, Materials Week 96, Cincinnati, October 7–9, 1996, 1997, pp. 265–280.
9. J.V. Cathcart, *The Oxidation of Nickel–Aluminium and Iron–Aluminium Alloys*, Materials Research Society Symposium Proceeding, vol. 39, 1985, pp. 445–459.
10. B.A. Leyens, I.G. Pint, *Surf. Coat. Tech.* 133–134 (2000) 15–22.
11. *Materials Science and Technology. A Comprehensive Treatment*. Edited by. R.W.Cahn, P. Haasen and E.J. Cramer. Corrosion and Environmental Degradation Vol. II. Wiley- VCH Weinheim. ISBN 3-527-20505-4. Federal Republic of Germany. 2000.
12. S. Taniguchi and T. Shibata, Influence of Si or Ti addition to Fe-23Cr-5Al Alloy Protectiveness of Preformed Al₂O₃ Scale Against Sulfidation, *Trans. Japan, Institute of Metals*. Vol.29, No. 8, pp. 658-664. 1988.
13. *Binary alloys phase diagrams*. 2nd ed. ASM International; 1996. On CD Rom.
14. N. Babu, R. Balasubramaniam, A. Ghosh. High Temperature Oxidation of Fe₃Al-based iron aluminides in oxygen. *Corrosion Science* 43 (2001) 2239–2254.
15. K.S. Graboswski and L.E. Rehin, in *Corrosion of Metals Processed by Directed Energy Beams*. Warrendale, Pa., pp.23-24, 1982.
16. M. Landkof, A.V. Levy, D.H. Boone, R. Gray and E. Yaniv. The Effect of Surface Additives on the oxidation of Chromia Forming Alloys. *Corrosion*. Vol. 41, pp.344-356.1985.
17. H.H. Davis, H.C. Grahman and I.A. Kvernes. Oxidation Behavior of Ni-Cr-1ThO₂ Alloys at 1000 and 1200C. *Oxid. Met.* Vol.3 pp. 431-452. 1971.
18. J. Stringer, B.A. Wilcox and R.I. Jaffee. The High Temperature Oxidation of Ni-20wt.%Cr Alloys Containing Dispersed Oxide Phases. *Oxid. Met.* Vol.5 pp. 11-34. 1972.
19. F.A. Golightly, G.C. Wood and F.H. Stott. Early Stages of Development of α -Al₂O₃ Scales on Fe-Cr-Al and Fe-Cr-Al-Y Alloys at High Temperatures. *Oxid. Met.* Vol.14. pp. 217-234. 1980.
20. T.A. Rannanarayanan, M. Raghavan and R. Petrovic-Luton. Metallic Yttrium Additions to High Temperatura Alloys: Influence of Al₂O₃ Scale Properties. *Oxid. Met.* Vol.22. pp. 83-100. 1984.

21. High-temperature characterization of reactively processed nanostructure nickel aluminide intermetallics. *Journal of Alloys and Compounds* 440 (2007) 178–188.
22. S.O. Moussa, K. Morsi. High-temperature oxidation of reactively processed nickel aluminide intermetallics. *Journal of Alloys and Compounds* 426 (2006) 136–143

CHAPTER 3

HIGH TEMPERATURE OXIDATION BEHAVIOR OF Ti_3Al AND Ti_3AlNdPr INTERMETALLIC ALLOYS.

ABSTRACT

The influence of rare earth elements (REE's) i.e. Neodymium (Nd) and Praseodymium (Pr) on the oxidation behavior of a Ti_3Al intermetallic alloy with and without rare earths has been evaluated, and its role on the oxidation rate and oxide morphology and formation is discussed. Specimens were isothermally oxidized in air at 800, 900, 1000, and 1100°C for 48 h. It was found that a simultaneous addition ($\leq 0.03\text{wt.}\%$) of both Nd and Pr, reduced the oxidation rate of the Ti_3Al intermetallic alloy. Analysis by scanning electron microscopy (SEM) revealed that the morphology of oxides formed on Ti_3Al intermetallic alloy specimens with and without REE's was very different. For these alloys mainly, aluminum enrichment at the metal/scale interface was observed.

INTRODUCTION

There are several potential applications that have been identified for TiAl-based alloys in the aerospace, automotive and turbine power generation markets. Aircraft engine manufacturers are pursuing the implementation of these alloys in aircraft engines. The progress in machine building, in particular, in the aerospace industry upon designing next-generation engines, requires new structural materials that can provide a higher level of service properties compared to the existing materials and/or a decrease in the construction weight due to the use of low-density materials. Therefore, it is interesting to use light alloys based on the intermetallic phases $\gamma\text{-TiAl} + \alpha_2\text{-Ti}_3\text{Al}$ as structural materials, since they have a high specific strength, stiffness, creep resistance, and heat resistance at elevated temperatures (600–900°C) [1]. For example, the use of $\gamma + \alpha_2$ alloys as a structural material for the parts of the hot path in a gas-turbine engine instead of nickel superalloys,

which have a significantly higher density, could substantially increase the thrust/weight ratio of the aircraft.

Recent extensive engine tests of components of TiAl-based alloys such as low-pressure turbine blades have revealed that no serious limitations exist to aircraft engine applications of TiAl-based alloys [2, 3]. The automotive community is pursuing the qualification and introduction of exhaust valves and turbocharger turbine wheels of TiAl-based alloys for automotive engines. Very recently TiAl turbocharger turbine wheels have started to be used for commercial cars of a special type [4]. Thus, these high-temperature structural aluminides are entering the first phase of structural applications. In parallel to these recent advances in the research and development for structural applications, considerable progress has been made in the basic research of high-temperature intermetallic compounds. First, it should be pointed out that our understanding of deformation and creep mechanisms and property/microstructure relationships in TiAl-based alloys is substantially deepened. There has been a decade of good interaction between the fundamental research and the industry communities in the field of TiAl-based alloys and such interaction is believed to have played an important role for progress in the research and development of structural applications for TiAl-based alloys.

Intermetallic compound phases identified in Ti-Al alloys, $\text{Ti}_3\text{Al}(\alpha_2)$, $\text{TiAl}(\gamma)$, Al_2Ti and Al_3Ti phases are stable at room temperature and their mechanical properties have been investigated using single-phase specimens. TiAl-based alloys with two-phase structures consisting of the major γ and minor α_2 phases are the most intensively studied materials among these aluminides and their alloys. There are two reasons for this. Firstly, their low density, strength and modulus retention at high temperatures, some tensile ductility at room temperature, and reasonably good oxidation resistance are very attractive as a new class of light-weight high-temperature materials for structural applications. Secondly, TiAl-based alloys can be processed more or less similarly to metals and alloys through conventional manufacturing processes such as ingot melting, casting, forging, precision casting and machining on almost conventional equipment [1-5].

The good oxidation resistance of these materials is based on their ability to develop a protective alumina layer (Al_2O_3) on their surface in many high-temperature environments. Because alloys based on TiAl and Ti_3Al form Al_2O_3 during exposure to oxidizing gases, they typically display low oxidation rates when compared to iron-based and other alloys that do not form alumina in similar conditions. Recent research showed that the rare earth element Y can refine microstructure and improve oxidation resistance of TiAl alloys [6,7]. Grain size reached nearly 60–80 μm by YAl₂ phase segregation at grain boundaries preventing grain growth [6,8], other work has suggested that oxidation of titanium aluminides without oxygen-active elements is worse in air than oxygen, particularly at 1000 and 1100°C, due to internal nitridation below a defective scale. The TiAl alloys produced by ingot-metallurgy processes tended to have worse oxidation behavior, since they had greater spallation than oxide-dispersion-strengthened Titanium aluminides of similar composition. In this work, a study of the oxidation behavior of ingot-metallurgy processes titanium aluminides in air has been carried out.

EXPERIMENTAL PROCEDURE

Ti-18wt.%Al (Ti_3Al) and Ti-18wt.%Al-0.01wt.%Nd-0.01wt.%Pr (Ti_3AlNdPr), intermetallic alloys were prepared from high purity Ti, Al, Nd and Pr elements (99.99%) in an electrical arc furnace using a purified argon atmosphere, from which rectangular strips of approximately 1.0 x 0.5 x 0.1 cm size were sectioned. The samples were cleaned and degreased. Afterwards, the surfaces were ground to 1200 grit paper, rinsed with distilled water and degreased with acetone. Each specimen was set on a platinum plate for weight-gain measurements in an electronic microbalance (sensitivity 10^{-6}g). Experiments were conducted in an atmosphere of air, a fixed temperature of 800, 900, 1000 and 1100°C (+ 2°C) and an exposure time of 48 h. The oxidized samples were analyzed using a scanning electron microscope (SEM- Jeol JSM-5800LV microscope) coupled with energy dispersive x-ray spectroscopy (EDS). These techniques are useful in

understanding the oxidation phenomena in terms of scale morphology and distribution products.

RESULTS AND DISCUSSION

Structure and Microstructure

Figure 1, shows the binary equilibrium phase diagram of Ti-Al [9]. Ti_3Al intermetallic with the D0_{19} structure meets the α_2 phase and enters into the composition of many more complex intermetallic used as high-temperature alloys. However, like many intermetallic, Ti_3Al is of low room-temperature ductility and strength and so can not be applied as a refractory material. The strength and ductility of single-crystalline Ti_3Al exhibit high orientation dependence. The γ and α_2 lamellae in the lamellar microstructures are stacked such that a $\{111\}\gamma$ plane is parallel to $(0001)\alpha_2$ and the closely packed directions on $\{111\}\gamma$ are parallel to those on $(0001)\alpha_2$: However, the $[110]$ direction and the other two $[101]$ and $[011]$ directions on (111) in the γ phase are not equivalent to each other because of the tetragonal L1_0 structure of the γ phase [Fig. 2(a)] while directions of $\langle 11\text{--}20 \rangle$ on the basal plane in the α phase (h.c.p.) and α_2 phase (hexagonal D0_{19}) are all equivalent [Fig. 2(b)]. Thus, when the γ phase precipitates from the aparent phase, the L1_0 structure can be formed in six orientation variants corresponding to the six possible orientations of the $[110]$ direction along a reference $\langle 11\text{--}20 \rangle$ direction of the α phase and thus of the α_2 phase [10].

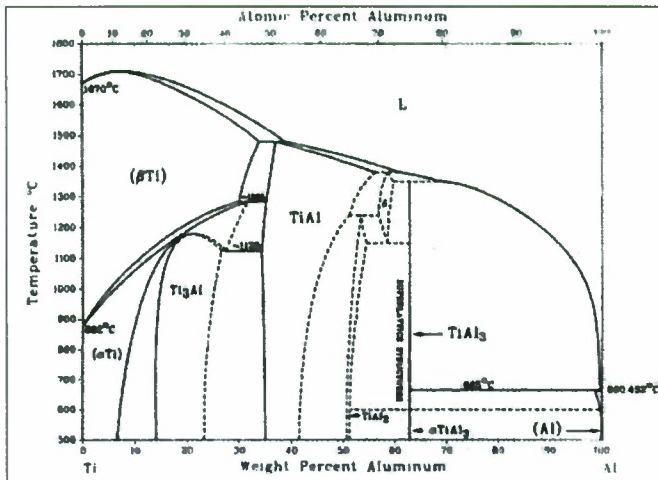


Figure 1. Equilibrium phase diagram of Ti-Al (9)

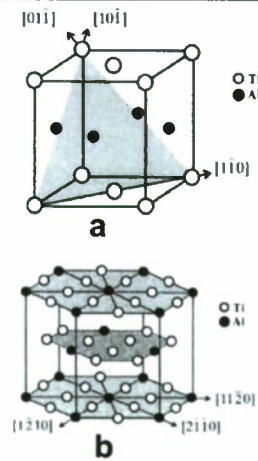


Fig. 2. Crystal structures of the (a) $L1_0$ and (b) $D0_{19}$ types.

Figure 3, shows the typical microstructure of the alloy in the laboratory ingots. Both ingots have a lamellar microstructure, which is characteristic of cast $\gamma+\alpha_2$ alloys and is represented by alternating γ and α_2 lamellae. Microstructure of the Ti_3Al intermetallic alloy without REEs (Fig. 3a) has a “parquet” shape with a big grain size. Besides, microstructure of the $Ti_3AlNdPr$ as cast alloy with REE’s has small grain size (Fig. 3b).

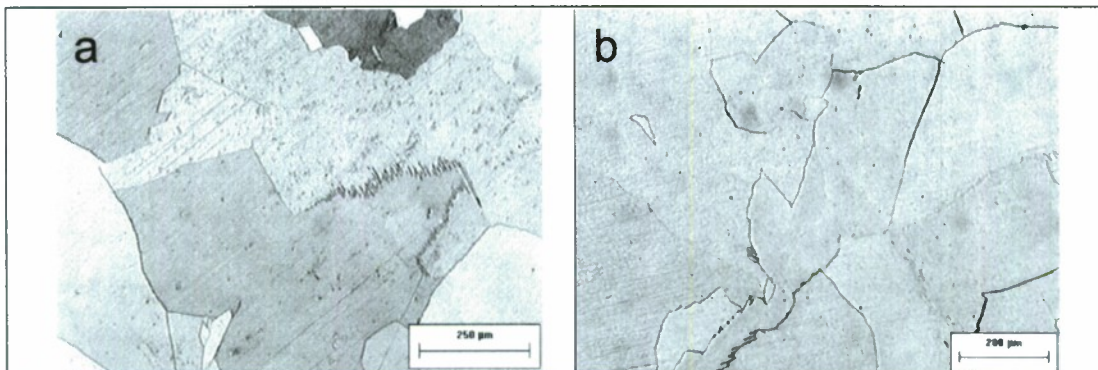


Figure 3. Some aspects of microstructures of a) Ti_3Al as cast, b) $Ti_3AlNdPr$ as cast

Kinetics

Figures 4 and 5 shows the weight gain per unit area against time for Ti_3Al and $Ti_3AlNdPr$ respectively; in samples oxidized in air at 800, 900, 1000 and 1100°C for

a period of 48 hours. In all cases, a parabolic behavior was found and the rate constants derived for all temperatures are shown in table 1.

The kinetic results confirmed the beneficial effect of Nd-Pr addition on the oxidation behavior of the Ti_3Al intermetallic alloys. Thus, the weight change observed for $Ti_3AlNdPr$ at 800, 900, 1000 and 1100°C was negligible (about 0.25, 0.32, 0.50 and 0.78 mg/cm², respectively) as compared to that for Ti_3Al at 800, 900, 1000 and 1100°C (3.43, 11.86, 33.28 and 49.07 mg/cm², respectively). Regard the temperature, the kinetic constants in this work were about thirteen to sixty times lower for the alloys without the addition of Nd and Pr, on the oxidation behavior of Ti_3Al intermetallic alloys. Thus, according with the present results, the addition of Nd-Pr helped to decrease the oxidation kinetics, probably by avoiding massive diffusion of Al towards the intermetallic/environment interface. Values of k_p were calculated from plots of square weight-change data versus time. Activation energy for were determined from the plot of parabolic rate law constants (k_p) in an Arrhenius diagram. The weight gain per unit area as a function of time, i.e. ($\Delta W/A$) versus t , constituted the primary data and curves are shown in fig.4 and 5 for Ti_3Al and $Ti_3AlNdPr$ respectively. The parabolic rate law was first considered as the basis of data processing and interpretation of results in this research work.

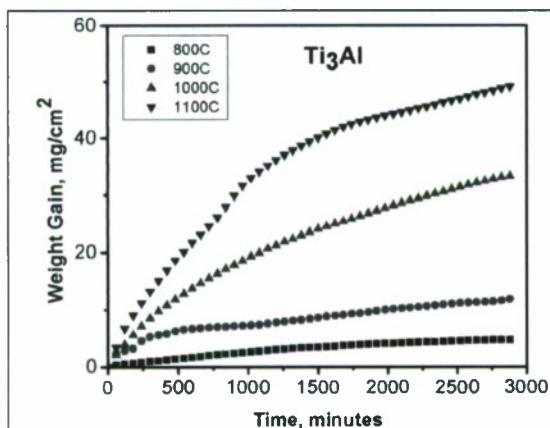


Fig.4. Kinetic data for the isothermal oxidation of Ti_3Al intermetallic alloy during oxidation at 800, 900, 1000 and 1100°C, in air for 48h.

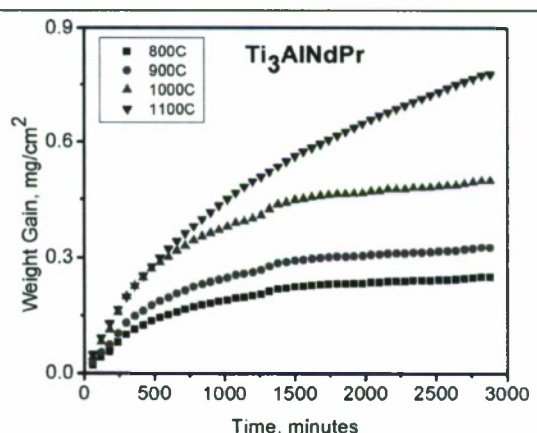


Fig.5. Kinetic data for the isothermal oxidation of $Ti_3AlNdPr$ intermetallic alloy during oxidation at 800, 900, 1000 and 1100°C, in air for 48h.

The parabolic rate constant (K_p) is related to the weight gain ($\Delta W/A$) and exposure time (t) by the following relation:

$$(\Delta W/A)^2 = K_p t + c \quad (1)$$

where c is a constant. The rate constant K_p was obtained from the slope of the linear regression-fitted line of $(\Delta W/A)^2$ vs t plot. The rate constants are provided in table 1 for the experiments performed in this study.

Table 1. Oxidation rate constant k_p of Ti_3Al and $Ti_3AlNdPr$ Intermetallic alloys at different temperatures.

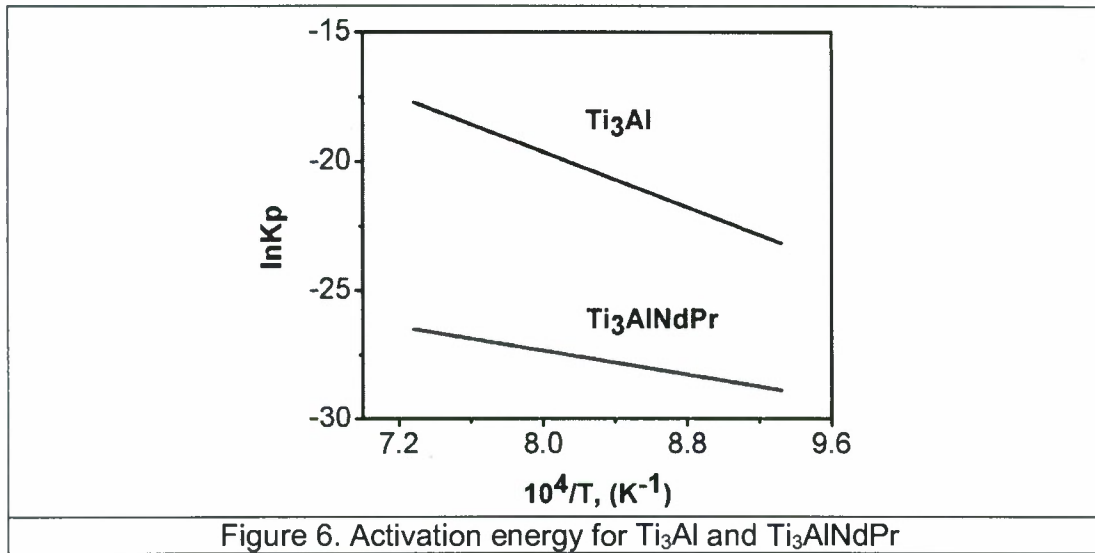
Intermetallic Alloys	$K_p, g^2cm^{-4}s^{-1}$	$K_p, g^2cm^{-4}s^{-1}$	$K_p, g^2cm^{-4}s^{-1}$	$K_p, g^2cm^{-4}s^{-1}$
	800°C	900°C	1000°C	1100°C
Ti_3Al	7.65×10^{-11}	7.47×10^{-10}	6.75×10^{-9}	1.50×10^{-8}
$Ti_3AlNdPr$	3.48×10^{-13}	5.93×10^{-13}	1.40×10^{-12}	3.71×10^{-12}

Fig. 6 shows the change in the experimentally determined values of K_p with the temperature for Ti_3Al and $Ti_3AlNdPr$ intermetallic alloys respectively. It is a normal practice to correlate the overall parabolic rate constant (K_p) and temperature through an Arrhenius-type equation:

$$K_p = K_0 \exp(-Q/RT) \quad (2)$$

Where R is the universal gas constant, K_0 the pre-exponential factor. T is the absolute temperature and Q is the activation energy.

The activation energies for this system were $Q_{Ti_3Al}=223$ and $Q_{Ti_3AlNdPr}=96$ KJ/mol. The values appear somewhat different than the values generally obtained for alumina-formation kinetics around $250 kJmol^{-1}$ [11]. Babu et al. found an activation energy of 92 kJ/mol for oxidation kinetics of Fe25Al [12]. The activation energy values collected from the present kinetics data are in agreement with Babu's values.

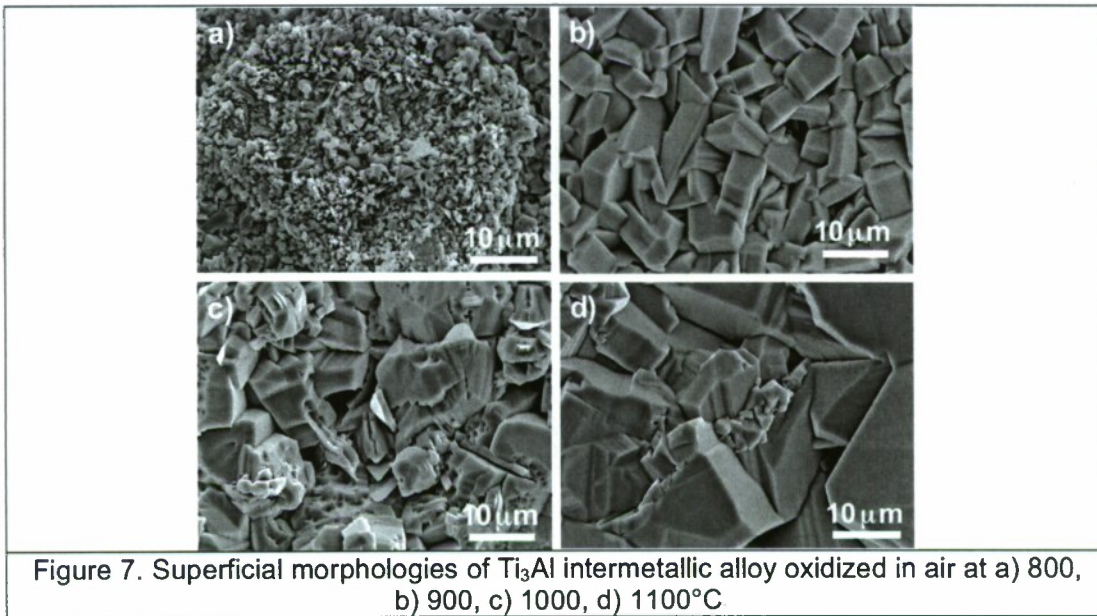


Morphology

In the present study, it was clearly observed that the nature of the formed scale on the binary intermetallic alloy do not presented changed with temperature at 900, 1000 and 1100°C. This was also evident from morphological observations in the SEM after the Ti_3Al specimens had been oxidized during 48h (fig. 7b,c,d), while, after 900°C oxidation the scale consist mainly of granular and plate-like oxides (fig. 7a). The oxidation characteristics of titanium aluminides at high temperatures are a major concern. In general, unlike Ni-Al alloys, a protective Al_2O_3 layer does not form on all the Ti-Al system because both Ti and Al form oxides of very similar stability. Aluminum forms a very slow growing $\alpha-Al_2O_3$, while titanium forms several oxides (TiO , TiO_2 , Ti_2O_3 , etc.), which have relatively high growth rates. It has been observed that a protective continuous layer of alumina is formed on Ti-Al alloys containing more than the stoichiometric amount of Al. $TiAl_3$ is the only compound on which a protective, continuous $\alpha-Al_2O_3$ was found to exist over a wide temperature range. [13–16] A nonprotective TiO was found to be the major oxide constituent on the surface of Ti_3Al at elevated temperatures.[17,18] In the case of a $TiAl$ stoichiometric compound, Ti-rich scales were formed at elevated temperatures resulting in an increase in the parabolic rate constant [17] by several orders of magnitude. Meier *et al.*[19] studied the oxidation behavior of $TiAl$ in air

and oxygen and observed that TiAl does not form a protective layer of α -Al₂O₃ but forms scales composed of TiO₂ and Al₂O₃. Their results indicate that the alloys in the Al-rich portion of the TiAl field formed a protective layer over the temperature range 1100°C to 1300°C.

In this study, isothermal oxidation of Ti-18wt.%Al alloy was studied in air over the temperature range of 800 to 1100°C. Oxidation rate constants were obtained from the weight gain curves using the parabolic law. The oxidation product was a mixture of TiO₂ and Al₂O₃ at 900, 1000 and 1100°C. While, after 800°C oxidation the external scale was not formed instead some distributed aluminum oxide nodules were formed (fig.8a). The rate of oxidation was rapid at 1000 and 1100°C for Ti₃Al intermetallic alloys without REE's.



Microalloying of REE's can significantly improve the oxidation resistance of Ti₃Al based alloy. Compared with REE's-free alloys, the oxidation rate of REE's-containing alloys was sharply reduced and not spallation signs existed on the surfaces of oxide scales. Scales were always granular-like (fig. 8a to d) at all the temperatures.

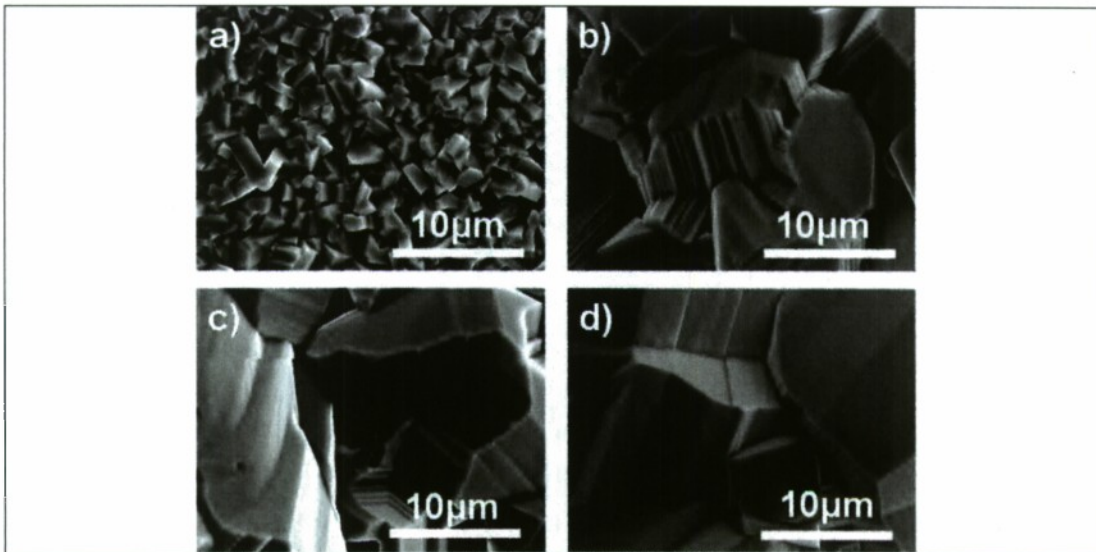


Figure 8. Superficial morphologies of Ti_3AlNdPr intermetallic alloy oxidized in air at a) 800, b) 900, c) 1000, d) 1100°C

CONCLUSIONS

The present work provided a detailed comparison of oxidation performance of Ti_3Al with and without Nd and Pr in air in the temperature range of 800–1100°C. The results based on specimen weight gain and microstructural characterizations indicated that Nd and Pr additions significantly improved the oxidation resistance of these alloys.

The oxidation behavior of a Ti_3Al and Ti_3AlNdPr intermetallic alloys in still air at 800, 900, 1000 and 1100°C, followed a parabolic kinetic behavior.

The kinetic constants for Ti_3Al intermetallic alloys without the addition of Nd and Pr were about forty times higher than those with these elements regardless the temperature.

The activation energies for this system were $Q_{\text{Ti}_3\text{Al}}=223$ and $Q_{\text{Ti}_3\text{AlNdPr}}=96$ KJ/mol. Nd and Pr additions improved the adherence of the TiO_2 and $\alpha\text{-Al}_2\text{O}_3$ scale.

The morphology of the oxides formed on specimens with and without REEs does not vary in shape, but the sizes have been change with the temperature.

REFERENCES

1. D. M. Dimiduk, "Gamma Titanium Aluminides Alloys—An Assessment within the Competition of Aerospace Structural Materials," *Mater. Sci. Eng. A* **263**, 281–288 (1999).
2. Austin, C. M. and Kelly, T. J., in *Structural Intermetallics*, ed. R. Darolia, J. J. Lewandowski, C. T. Liu, P. L. Martin, D. B. Miracle and M. V. Nathal. TMS, Warrendale, PA, 1993, p. 143.
3. Austin, C. M., Kelly, T. J., McAllister, K. G. and Chesnutt, J. C., in *Structural Intermetallics 1997*, ed. M. V. Nathal, R. Darolia, C. T. Liu, P. L. Martin, D. B. Miracle, R. Wagner and M. Yamaguchi. TMS, Warrendale, PA, 1997, p. 413.
4. M. Yamaguchi, H. Inui and K. ITO. *High-Temperature Structural Intermetallics. Acta Mater.* **48** (2000) 307-322.
5. London, B. and Kelly, T. J., in *Microstructure/Property Relationships in Titanium Aluminides*, ed. Y.-W. Kim and R. R. Boyer. TMS, Warrendale, PA, 1992, p. 285.
6. B.H. Li, F.T. Kong, Y.Y. Chen, *J. Rare Earths* **24** (2006) 352.
7. Y.Wu, K. Hagihara, Y. Umakoshi, *Intermetallics* **12** (2004) 519.
8. F.T. Kong, Y.Y. Chen, B.H. Li. Influence of yttrium on the high temperature deformability of TiAl alloys. *Materials Science and Engineering A. Volume 499, Issues 1-2, 15 January 2009, Pages 53-57*
9. *Binary alloys phase diagrams*. 2nd ed. ASM International; 1996. On CD Rom.
10. Yamaguchi, M. and Inui, H., in *Structural Intermetallics 1993*, ed. R. Darolia, J. J. Lewandowski, C. T. Liu, P. L. Martin, D. B. Miracle and M. V. Nathal. TMS, Warrendale, PA, 1993, p. 12.
11. I. G. Wright, B. A. Pint, and P. F. Tortorelli, *Oxidation of Metals* **55**, 333 (2001).
12. N. Babu, R. Balasubramaniam, A. Ghosh. *High Temperature Oxidation of Fe3Al-based iron aluminides in oxygen. Corrosion Science* **43** (2001) 2239–2254.
13. N. Birks, G.H. Meier, and F.S. Pettit: *JOM*, 1994, vol. 46, pp. 42-46.
14. J. Subrahmanyam: *J. Mater. Sci.*, 1989, vol. 23, pp. 1906-10.
15. J.L. Smialek: *Corr. Sci.*, 1993, vol. 35 (5–8), pp. 1199-1208.
16. R.G. Reddy and X. Wen: *EPD Congr. '97*, TMS, Warrendale, PA, 1997, pp. 47-54.
17. X. Wen and R.G. Reddy: *Processing and Fabrication of Advanced Materials*, TMS, Warrendale, PA, 1996, pp. 379-89.
18. G. Welsch and A.I. Kahveci: in *Oxidation of High-Temperature Intermetallics*, T. Grobstein and J. Doychak, eds., TMS, Cleveland, OH, 1998, pp. 207-18.
19. G.H. Meier, D. Appalonia, R.A. Perkins, and K.T. Chiang: *Oxidation of High-Temperature Intermetallics*, T. Grobstein and J. Doychak, eds., TMS, Cleveland, OH, 1988, pp. 185-93.

CHAPTER 4

HIGH TEMPERATURE OXIDATION BEHAVIOR OF FeAl AND FeAlNdPr INTERMETALLIC ALLOYS.

ABSTRACT

The influence of rare earth elements (REE's) i.e. Neodymium (Nd) and Praseodymium (Pr) on the oxidation behavior of a FeAl intermetallic alloy with and without rare earths has been evaluated, and its role on the oxidation rate and oxide morphology and formation is discussed. Specimens were isothermally oxidized in air at 800, 900, 1000, and 1100°C for 48 h. It was found that a simultaneous addition (≤ 0.03 wt.%) of both Nd and Pr, reduced the oxidation rate of the FeAl intermetallic alloy. Analysis by scanning electron microscopy (SEM) revealed that the morphology of oxides formed on FeAl intermetallic alloy specimens with and without REE's was very different. For these alloys mainly, aluminum enrichment at the metal/scale interface was observed.

INTRODUCTION

For more than 50 years, iron-aluminum intermetallic have received special interest because of their potentially high oxidation resistance at high temperature.[1] They offer a good alternative for use in automotive parts, chemical processing, and gas turbine technologies since they possess a high melting point, high thermal conductivity, excellent oxidation resistance, low density, and low cost.[2]

Iron aluminides, based around the stoichiometric compositions of Fe_3Al and FeAl, offer excellent resistance to oxidation and sulphidation at high temperatures, with low material cost and density than austenitic and ferritic stainless steels [3,4]. They contain enough aluminum to form a thin film of aluminum oxide (in oxidizing environments) that is often compact and protective. They possess relatively high specific strengths and suitable mechanical properties at elevated temperatures. They have, therefore, undergone extensive development, in the recent past, exclusively for high temperature applications. However, their potential use as

structural materials at elevated temperatures has been hindered by limited ductility at room temperature and sharp drop in strength above 600°C. It is well established that the poor room temperature ductility of iron aluminides is due to hydrogen embrittlement [5,6]. Considerable efforts have been devoted to understand and improve their mechanical properties

Iron aluminides are receiving special attention because they have a good yielding point between 600 and 800°C, and even up to 1000°C when they are alloyed with low expansion fibers such as alumina (Al_2O_3).[7] The charpy impact energy is satisfactory at room temperature, and, depending on the grain size, the FeAl(40 at.%) offers a yielding point between 250 and 600 MPa, which can be increased with additions of Hf or B.[8] Also, ingot iron aluminides have a lower density (5.6 g/cm³) compared that for stainless steels and some nickel-based alloys, and a relatively high melting point (1237°C). Their main disadvantage is their poor ductility at room temperature. In the last few years, some new processing routes have been tried to improve their ductility[9] together with the addition of fibers and some microalloying elements.[10] A method that has been used successfully has been spraying, which avoids macrosegregation and minimizes microsegregation.

The good oxidation resistance of these materials is based on their ability to develop a protective alumina layer (Al_2O_3) on their surface in many high-temperature environments. Because alloys based on Fe_3Al and FeAl form Al_2O_3 during exposure to oxidizing gases, they typically display low oxidation rates when compared to iron-based and other alloys that do not form alumina in similar conditions. Other work has suggested that oxidation of iron aluminides without these oxygen-active elements is worse in air than oxygen, particularly at 1000 and 1100°C, due to internal nitridation below a defective scale. The FeAl alloys produced by ingot-metallurgy processes tended to have worse oxidation behavior, since they had greater spallation than oxide-dispersion-strengthened iron aluminides of similar composition.[11,12]. In this work, a study of the oxidation behavior of ingot-metallurgy processes iron aluminides in air has been carried out.

EXPERIMENTAL PROCEDURE

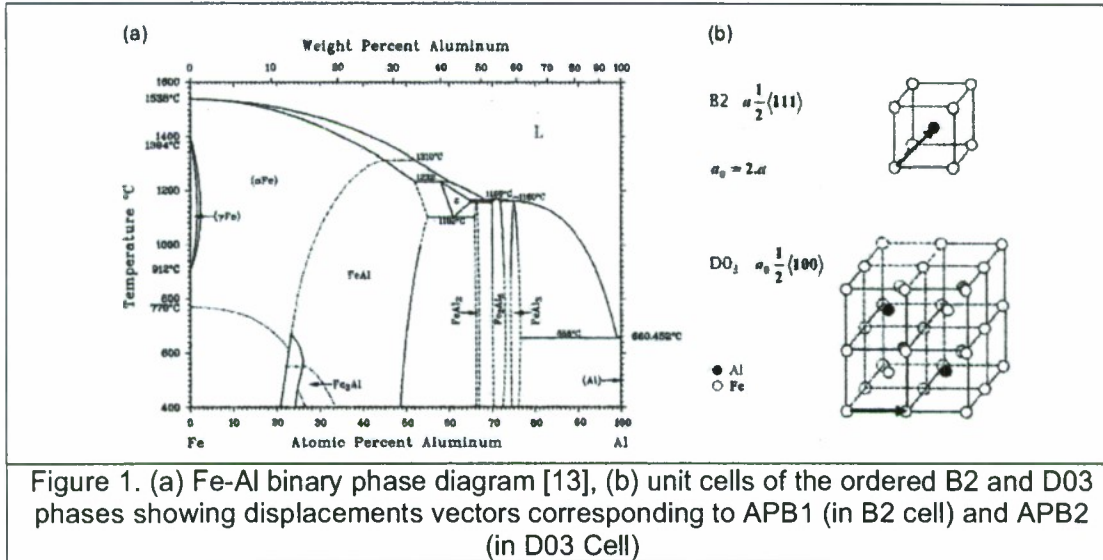
Fe-28wt.%Al (FeAl) and Fe-28wt.%Al-0.01wt.%Nd-0.01wt.%Pr (FeAlNdPr), intermetallic alloys were prepared from high purity Fe, Al, Nd and Pr elements (99.99%) in an electrical arc furnace using a purified argon atmosphere, from which rectangular strips of approximately 1.0 x 0.5 x 0.1 cm size were sectioned. The samples were cleaned and degreased. Afterwards, the surfaces were ground to 1200 grit paper, rinsed with distilled water and degreased with acetone. Each specimen was set on a platinum plate for weight-gain measurements in an electronic microbalance (sensitivity 10^{-6} g). Experiments were conducted in an atmosphere of air, a fixed temperature of 800, 900, 1000 and 1100°C (+ 2°C) and an exposure time of 48 h. The oxidized samples were analyzed using a scanning electron microscope (SEM- Jeol JSM-5800LV microscope) coupled with energy dispersive x-ray spectroscopy (EDS). These techniques are useful in understanding the oxidation phenomena in terms of scale morphology and distribution products.

RESULTS AND DISCUSSION

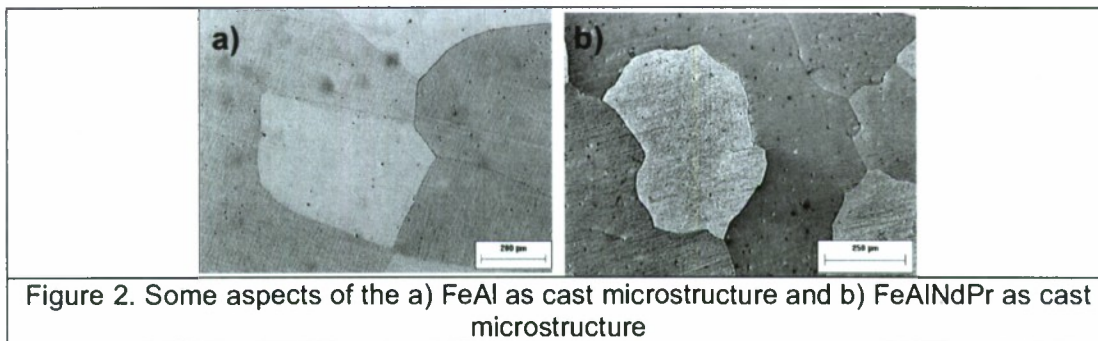
Structure and Microstructure

Iron aluminides exhibit ordered-disorder transformations and large concentrations of defects that depend on temperature and composition [13,14]. In the Fe-rich portion of the FeAl binary diagram exist the disordered A2 and the ordered B2 (FeAl) and D03 (Fe₃Al) phases [15], as shown in Fig. 1a. It is accepted since long that the ordering transformations begin with the formation of small ordered nuclei, which eventually grow until they occupy the entire volume of the crystal, resulting in an anti-phase domain structure that is usually characterised by transmission electron microscopy [16]. Different types of antiphase boundaries are present in the ordered alloys depending on their structure. In B2 ordered alloys only one type of antiphase boundary is found, the B2-type APB (or APB1) that is formed through the A2→B2 ordering transformation and that has a fault vector $\frac{1}{2}\langle 111 \rangle$ (where $\frac{1}{2}$

is the lattice parameter of the B2 unit cell). In ordered D0₃ two types of anti-phase boundaries can appear: the APB1 that forms as above, with a fault vector $\frac{a_0}{4}\langle 111 \rangle$ (where a_0 is the lattice parameter of the D0₃ unit cell) and the D0₃-type APB (or APB2) related to the B2→D0₃ transformation with a fault vector $\frac{a_0}{2}\langle 100 \rangle$ [17-19]. The unit cell and the fault vectors are shown in figure 1b.



Microstructural examination of the compact in the as-cast condition revealed an no homogeneous grain size distribution, Fig. 2, with an average size of about 400 and 280μm for as cast FeAl and FeAlNdPr respectively.



Kinetics

Figures 3 and 4 shows the weight gain per unit area against time for FeAl and FeAlNdPr respectively; in samples oxidized in air at 800, 900, 1000 and 1100°C for

a period of 48 hours. In all cases, a parabolic behavior was found and the rate constants derived for all temperatures are shown in table 1.

The kinetic results confirm the beneficial effect of Nd-Pr addition on the oxidation behavior of the FeAl intermetallic alloys. Thus, the weight change observed for FeAlNdPr at 800, 900, 1000 and 1100°C was negligible (about 0.13, 0.20, 0.30 and 0.36 mg/cm², respectively) as compared to that of FeAl at 800, 900, 1000 and 1100°C (3.00, 4.86, 7.07 and 9.55 mg/cm², respectively). FeAl specimens showed cracking on the scale surface under exposition for 48 h. Irrespective of temperature, the kinetic constants in this work are about twenty times below the ones without the addition of Nd and Pr, on the oxidation behavior of FeAl intermetallic alloys. Thus, according with the present results, the addition of Nd-Pr helps to decrease the oxidation kinetics, probably by avoiding massive diffusion of Al towards the intermetallic/environment interface.

The isothermal oxidation behavior is reported together with the morphology of the oxidation products formed on the FeAl intermetallics. The results are discussed in terms of the oxidation kinetics and the negative or positive influence of the reactive elements. Though the intermetallics based on the system FeAl have shown good resistance against isothermal oxidation at high temperature, in previous studies it has been observed the spalling of oxide scale formed on this type of intermetallics [20]. Further, it has been reported that the alumina scale formed on the FeAl (40at.%Al) alloy has cracked considerably during oxidation tests between 900 and 1100 °C. Similar results have been observed in intermetallics with additions of B and Al₂O₃ oxidized isothermally at 1100 °C [21]. The results of the weight gain plots indicate that the process of oxidation did follow a parabolic behavior.

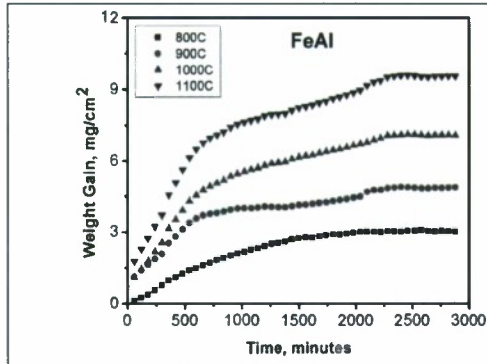


Fig.3. Kinetic data for the isothermal oxidation of FeAl intermetallic alloy during oxidation at 800, 900, 1000 and 1100°C for 48h.

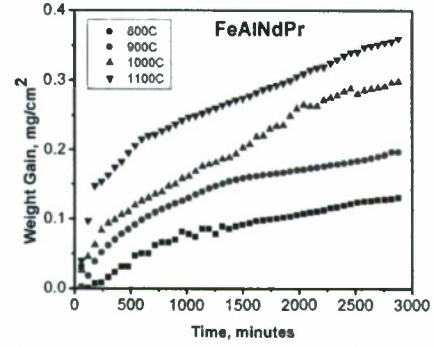


Fig.4. Kinetic data for the isothermal oxidation of FeAlNdPr intermetallic alloy during oxidation at 800, 900, 1000 and 1100°C for 48h.

The parabolic rate constant (K_p) is related to the weight gain ($\Delta W/A$) and exposure time (t) by the following relation:

$$(\Delta W/A)^2 = K_p t + c \quad (1)$$

where c is a constant. The rate constant K_p was obtained from the slope of the linear regression-fitted line of $(\Delta W/A)^2$ vs t plot. The rate constants are provided in table 1 for the experiments performed in this study.

Table 1. Oxidation rate constant k_p of alloy at different temperatures

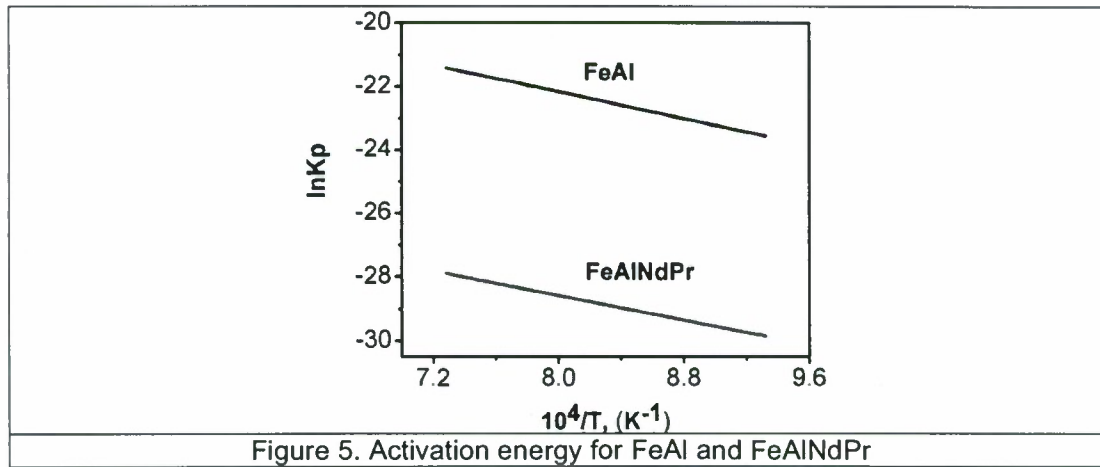
Intermetallic Alloys	$K_p, g^2cm^{-4}s^{-1}$	$K_p, g^2cm^{-4}s^{-1}$	$K_p, g^2cm^{-4}s^{-1}$	$K_p, g^2cm^{-4}s^{-1}$
	800°C	900°C	1000°C	1100°C
FeAl	6.17×10^{-11}	1.20×10^{-10}	2.90×10^{-10}	5.02×10^{-10}
FeAlNdPr	1.05×10^{-13}	2.22×10^{-13}	5.57×10^{-13}	6.5×10^{-13}

Fig. 5 shows the change in the experimentally determined values of K_p with the temperature for FeAl and FeAlNdPr intermetallic alloys respectively. It is a normal practice to correlate the overall parabolic rate constant (K_p) and temperature through an Arrhenius-type equation:

$$K_p = K_o \exp(-Q/RT) \quad (2)$$

Where R is the universal gas constant, K_0 the pre-exponential factor. T is the absolute temperature and Q is the activation energy.

The activation energies for this system were $Q_{\text{FeAl}}=88$ and $Q_{\text{FeAlNdPr}}=79$ KJ/mol. Babu et al. found an activation energy of 92 kJ/mol for oxidation kinetics of Fe25Al [22]. The activation energy values collected from the present kinetics data are in agreement with Babu's values.



Morphology

In the present study, it was clearly observed that the nature of the formed scale on the binary intermetallic alloy changed with temperature. This was also evident from morphological observations in the SEM after the FeAl specimens had been oxidized during 48h (fig. 6), Spalling of scale was more pronounced at 900 and 1100°C oxidation temperatures. After oxidation at 800°C, the surface oxide morphology consisted mainly of conic-like oxides with some granular oxides in a few places (fig. 6).

Iron aluminides depend on the formation of an alumina scale for their oxidation and corrosion resistance. At low concentrations of Al, internal oxidation of Al occurs and Fe_2O_3 and Fe_3O_4 form on the exterior of the alloys. At intermediate Al concentrations, although a transient alumina layer is formed, it tends to be disrupted by iron nodules. Approximately 15 at% Al must be added to Fe to

produce a continuous layer of Al_2O_3 during oxidation. Small Cr additions reduce the aluminum requirement, but Ni additions require increased amounts of Al to avoid the formation of nodules of Fe-aluminum rich oxides that disrupt the alumina scale. In the case of FeAl intermetallic alloy oxidized at 800 and 900°C it can be seen an external scale of iron oxide and under this scale a rich aluminum oxide was found (fig. 6).

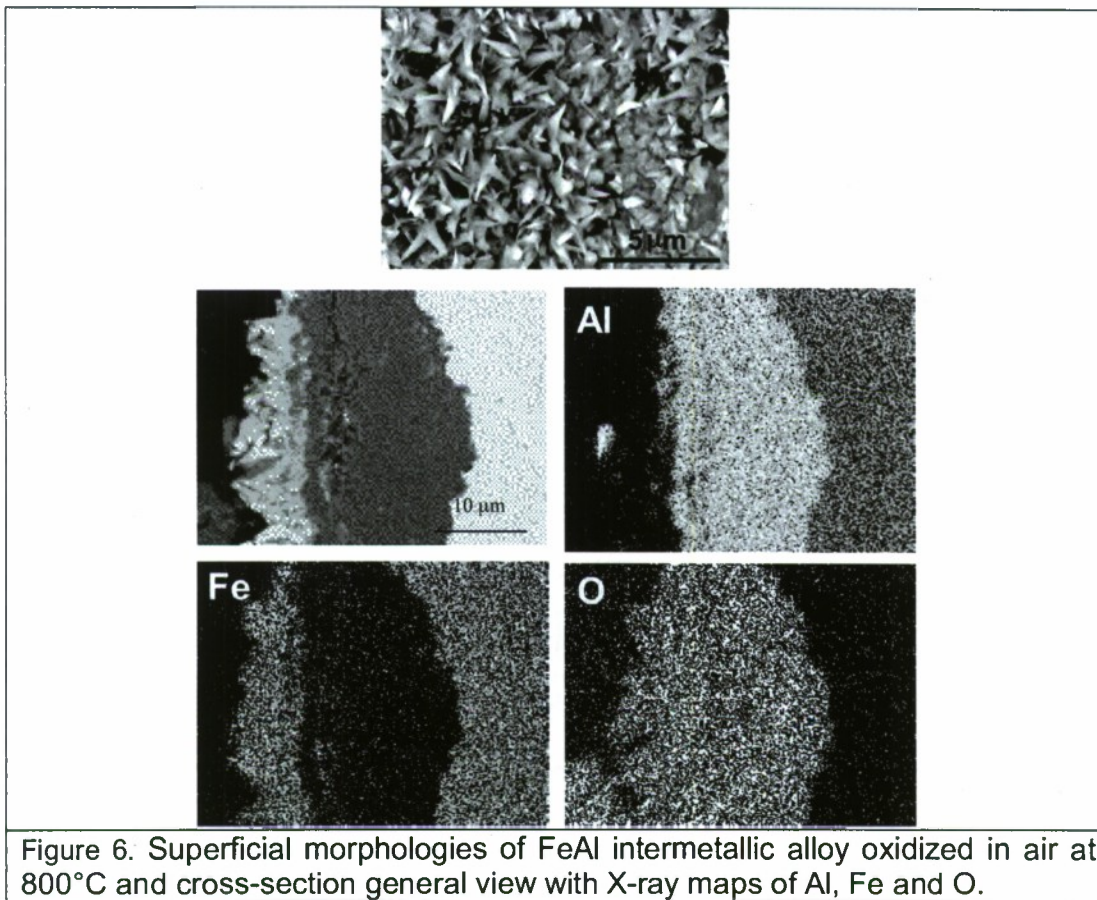


Figure 6. Superficial morphologies of FeAl intermetallic alloy oxidized in air at 800°C and cross-section general view with X-ray maps of Al, Fe and O.

Microalloying of REE's can improve the oxidation resistance of FeAl based alloy significantly. Compared with REE's-free alloys, the oxidation rate of REE's-containing alloys was sharply reduced and slight spallation signs existed on the surfaces of oxide scales. Scales are sometimes smooth at 800°C and convoluted at 1100°C oxidized in air during 48 h (fig. 7). In fig. 7 is also shown the

backscattered image of the cross-section of FeAlNdPr intermetallic alloy oxidized in air at 800°C with X-ray maps of Al, Fe and O.

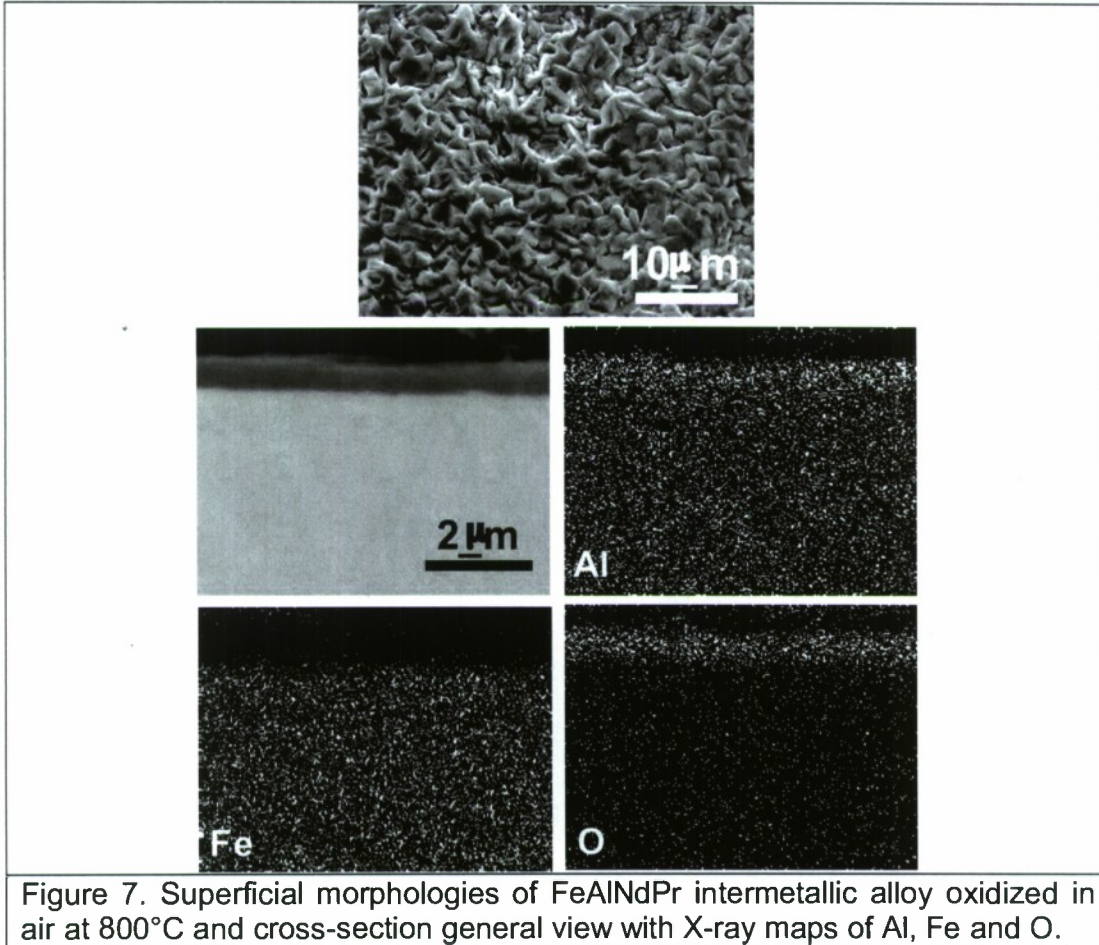


Figure 7. Superficial morphologies of FeAlNdPr intermetallic alloy oxidized in air at 800°C and cross-section general view with X-ray maps of Al, Fe and O.

Fig. 8. Show the line profile of FeAlNdPr intermetallic alloy oxidized at 1100°C during 48h. The alumina containing very little iron equilibrates with Fe-Al alloys over their whole composition range. The values for the dissociation pressure of α - Al_2O_3 coexisting with the binary alloys can be determined by the following reaction:



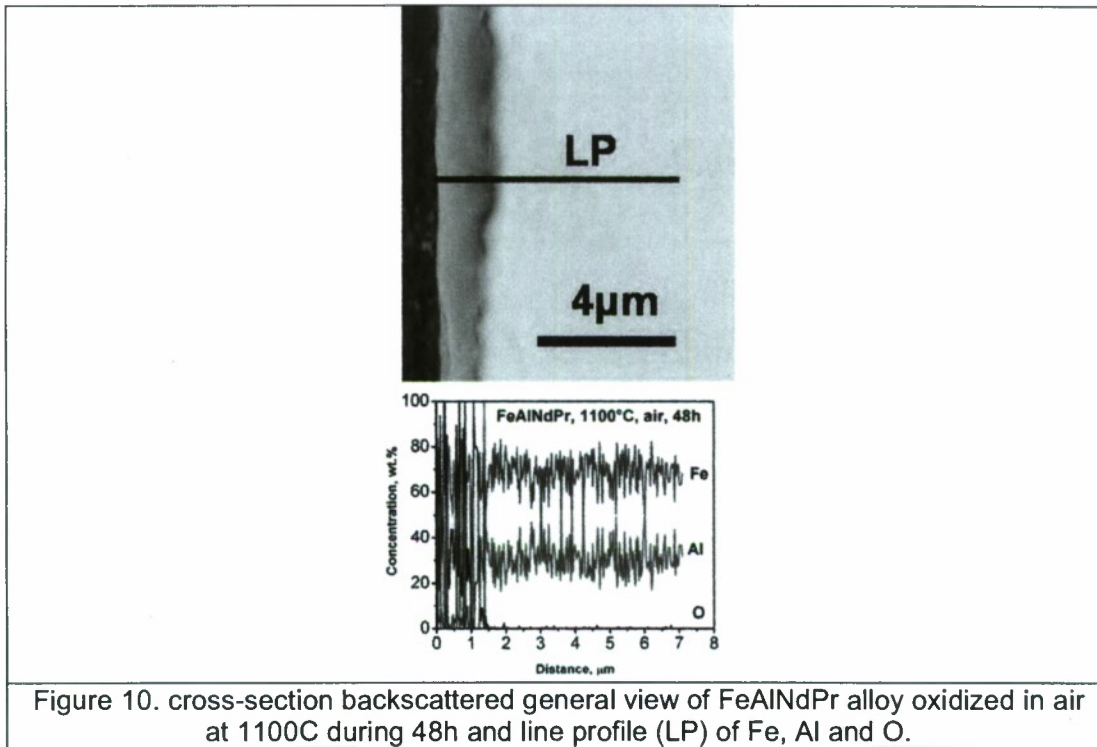
For which

$$P_{\text{O}_2} = [\text{alloy} + \text{alumina}] = a_{\text{Al}}^{-2/3} \exp\left(\frac{2\Delta G_f^\circ}{3RT}\right) = 2.425 \times 10^{-21} \text{ atm}$$

where:

a_{Al} = is the aluminum activity in the alloy = 1.7×10^{-2} at 1273 K [12]
 ΔG_f° = is the standard free energy of formation of alumina = -840 kJ/mol at 1273 K
 T = test temperature = 1273 K (1000 °C)
 R = gas constant = 8.314472 J/mol K

On the other hand, previous studies have demonstrated that for a binary Fe-Al alloy, it is needed between 16 to 19 at.%Al to suppress the internal oxidation and the growth of iron oxides at 800-900 °C, so that only a scale of Al_2O_3 is formed [23]. Whereas Rynnikov [24] mentions that 30 at.%Al is necessary for a suitable protection between 900 and 1100 °C. Finally, Tortorelli et al. [25] showed that Al_2O_3 is the main external oxide in alloys with Al content more than 15 wt.%. In this study was found an external protective scale of Al_2O_3 for the FeAlNdPr intermetallic alloy at all the working temperatures.



CONCLUSIONS

The present work provided a detailed comparison of oxidation performance of FeAl with and without Nd and Pr in air at the temperature range of 800–1100 °C. The

results based on specimen weight gain and microstructural characterizations indicated that Nd and Pr additions significantly improved the oxidation resistance of these alloys.

The oxidation behavior of a FeAl and FeAlNdPr intermetallic alloys in still air at 800, 900, 1000 and 1100°C followed a parabolic kinetic behavior.

The kinetic constants for FeAl intermetallic alloys without the addition of Nd and Pr were about twenty times higher than those with these elements regardless the temperature.

The activation energies for this system were $Q_{\text{FeAl}}=88$ and $Q_{\text{FeAlNdPr}}=79$ KJ/mol

Nd and Pr additions improved the adherence of the $\alpha\text{-Al}_2\text{O}_3$ scale.

The morphology of the oxides formed on specimens with and without REEs varies significantly from fine-grained, platelet-like and ridges-like to convoluted oxide.

REFERENCES

1. C. Sykes and J. Bampfylde: *J. Iron Steel Inst.*, 1934, vol. 130, pp.389-418.
2. G. Webband and A. Lefort: *Symp. Proc. Fatigue and Fracture of Ordered Intermetallic Materials: I*, TMS, Warrandale, PA, 1994, p.103.
3. C.T. Liu, J.O. Stiegler, F.H. Froes, *Ordered intermetallics*, 10th ed. *Metals Handbook*, vol. 2, ASM, Metals Park, USA, 1990, pp. 913-943.
4. C.T. Liu, K.S. Kumar, *Ordered intermetallic alloys*, part 1, nickel and iron aluminides, *J. Metals* 45(1993) 38-44.
5. C.T. Liu, C.G. McKamey, E.H. Lee, Environmental effects on room temperature ductility and fracture mode in Fe₃Al alloys, *Scripta Metall.* 24 (1990) 385-390.
6. C.T. Liu, C.G. McKamey, E.H. Lee, An environmental effect as the major cause room temperature embrittlement in FeAl, *Scripta Metall.* 23 (1996) 875-880.
7. J.L. Smialek, J. Doychak, and D.J. Gaydosh: in *Oxidation of High-Temperature Intermetallics*, T. Grobstein and J. Doychak, eds., TMS, Warrandale, PA, 1989, p. 83.
8. J.H. Schneibel: *Mater. Sci. Eng.*, 1992, vol. A153, p. 684.
9. S. Zeng, X.R. Nutt, and E.J. Lavernia: *Metall. Mater. Trans.*, 1994, vol. A26, p. 817.
10. R.G. Baligidad, U. Prakash, and A. Radha Krishna: *Mater. Sci. Eng.*, 1997, vol. A230, p. 188.

11. B.A. Pint, P.F. Tortorelli, and I.G. Wright: *Mater. Corr.*, 1996, vol.47, pp. 663-74.
12. B.A. Pint, P.F. Tortorelli, and I.G. Wright: *Mater. High Temp.*, 1997, vol. 15, p. 613.
13. Morris MA, George O, Morris DG. *Mater Sci Eng* 1998;A258:99.
14. Inden G, Pepperhoff W. *Z Metallkd* 1990;81:770.
15. Binary alloys phase diagrams. 2nd ed. ASM International; 1996. On CD Rom.
16. Marcinkowski MJ, Brown N. *J Appl Phys* 1962;33:537.
17. Karlik M. *Mater Sci Eng* 1997; A234e236:212.
18. Liu W, Rosner H, Langmaack E, Gemperle A, Gemperlova J, Pesicka J, et al. *Mater Sci Eng* 1998;A258:15.
19. Yoshimi K, Hanada S, Onuma T, Yoo MH. *Phil Mag A* 1996;73:443.
20. Xu C. H., Gao W. and Li S. 2001. Oxidation behavior of FeAl intermetallics- The effect of Y on the scale spallation resistance. *Corrosion Science* 43, pp. 671-688.
21. Natesan K., Klug K., Renuagh D. Veal B. W. and Grimsditch M. Microstructural and mechanical characterization of alumina scales thermally developed on iron aluminides alloys. ANL/FE-96/01.
22. N. Babu, R. Balasubramaniam, A. Ghosh. High Temperature Oxidation of Fe3Al-based iron aluminides in oxygen. *Corrosion Science* 43 (2001) 2239–2254.
23. Brady M. P., Pint B. A. Tortorelli P. F. Wright I. G. and Hanrahan R. J. Jr. 2002. High Temperature Oxidation and Corrosion of Intermetallics. Chapter 6. From Corrosion and Environmental Degradation, edited by M. Schütze. Published By Wiley-VCH Verlag W.
24. Ryl'nikov B. S., Arkhangelskaya G. V. and Lyubetskaya L. V. *Protection Metals* 17:290(1981).
25. Tortorelli P. F. and DeVan J. H. 1992. Behavior of iron aluminides in oxidizing and sulfidizing environments. *Materials Science and Engineering A53*, pp. 573-577.

CHAPTER 5

HIGH TEMPERATURE OXIDATION BEHAVIOR OF NiAl AND NiAlNdPr INTERMETALLIC ALLOYS.

ABSTRACT

The influence of rare earth elements (REE's) i.e. Neodymium (Nd) and Praseodymium (Pr) on the oxidation behavior of a NiAl intermetallic alloy with and without rare earths has been evaluated, and its role on the oxidation rate and oxide morphology and formation is discussed. Specimens were isothermally oxidized in air at 800, 900, 1000, and 1100°C for 48 h. It was found that a simultaneous addition (≤ 0.03 wt.%) of both Nd or Pr, reduced the oxidation rate of the NiAl intermetallic alloy. Analysis by scanning electronic microscope (SEM) revealed that the morphology of oxides formed on NiAl intermetallic alloy specimens with and without REE's was very different. For these alloys mainly, aluminum enrichment at the metal/scale interface was observed.

INTRODUCTION

Intermetallic compounds such as nickel aluminides (NiAl and Ni₃Al), iron aluminides (FeAl, and Fe₃Al) and titanium aluminides (TiAl and Ti₃Al) are a class of advanced materials with considerable potential for low and high-temperature application [1–5]. Processing approaches for aluminides include casting, thermomechanical and powder processing of pre-alloyed powder [6]. Because of the potential use of nickel aluminides at high temperatures, it is imperative to understand and study their oxidation behavior. It was reported that the types of scale (oxide or mixture of oxides) and scale morphology formed on the surface of the alloy during high-temperature oxidation were influenced by both the compositions of the gas and the alloy as well as the reaction temperature [7]. Both thermodynamic and kinetic factors should be considered to understand this complex oxidation process. Thermodynamics governs and predicts the type of oxide that can form under the operating conditions, and for nickel aluminides, the formation of alumina (Al₂O₃), nickel oxide (NiO), and nickel aluminate (NiAl₂O₄)

have been reported to compete with one another, depending on which one is more thermodynamically stable to form at the operating temperature [8–11].

For many years, nickel-aluminum intermetallic have received special interest because of their potentially high oxidation resistance at high temperature.[1] They offer a good alternative for use in automotive parts, chemical processing, and gas turbine technologies since they possess a high melting point, high thermal conductivity, excellent oxidation resistance, low density, and low cost.[2]. Other work has suggested that oxidation of nickel aluminides without these oxygen-active elements is worse in air than oxygen, particularly at 1000 and 1100°C, due to internal nitridation below a defective scale. The Ni₃Al alloys produced by ingot-metallurgy processes tended to have worse oxidation behavior, since they had greater spallation than oxide-dispersion-strengthened nickel aluminides of similar composition.[7] In this work, a study of the oxidation behavior of ingot-metallurgy processes of nickel aluminides in air has been carried out.

EXPERIMENTAL PROCEDURE

Ni-30wt%Al (NiAl) and Ni-30wt%Al-0.01Nd-0.01Pr (NiAlNdPr), intermetallic ingots were produced by a standard electrical arc furnace with a purified argon atmosphere using high pure Ni, Al, Nd and Pr metals (99.99%), Coupons with the dimensions of 1.0 x 0.5 x 0.1 cm size were sectioned from the cast ingot. The samples were cleaned and degreased. Afterwards, the surfaces were ground to 1200 grit paper, rinsed with distilled water and degreased with acetone. Each specimen was set on a platinum plate for weight-gain measurements in an electronic microbalance (sensitivity 10⁻⁶g). Experiments were conducted in an atmosphere of air, a fixed temperature of 800, 900, 1000 and 1100°C (+ 2°C) and an exposure time of 48 h. The oxidized samples were analyzed using a scanning electron microscope (SEM- Jeol JSM-5800LV microscope) coupled with energy dispersive x-ray spectroscopy (EDS). These techniques are useful in

understanding the oxidation phenomena in terms of scale morphology and distribution products.

RESULTS AND DISCUSSION

Structure and Microstructure

In the Ni-Al alloy system, as the Al content is varied, other phases in addition to the γ , γ' , and β appear. A map of all of these phases formed as a function of composition and temperature is called the (equilibrium) phase diagram, shown in Fig. 1, (based on Binary alloys phase diagrams. 2nd ed. ASM International; 1996.). Equilibrium here refers to the fact that the phases in the map remain stable over time when held at appropriate temperatures. Because the diagram shown here describes an alloy of two components only, Ni and Al, it is called a binary phase diagram. The two phases bounding the diagram (in this case fcc Al and Ni) are called the terminal phases.

Ni crystallizes in a face center cubic (fcc) structure. If we alloy Ni by adding Al, several significant changes occur. For up to about 4wt%Al, there is no change in the atomic arrangement of Ni except an occasional Al atom replacing a Ni atom randomly, as in Fig. 2(a). The structure remains essentially like fcc Ni, called the γ phase. As the Al content is increased, it starts selectively replacing the corner atoms (Fig. 2(b)), while the atoms on the cube faces remain Ni. NiAl has the ordered B2 crystal structure, which is derived from the body centered cubic structure by placing all the nickel atoms at the cube corners and the aluminum atoms at the body centers of each unit cell. The central Al atom belongs to this cell, while the corner atoms are each shared with eight cells. The overall share is therefore 1 Al and 1 Ni, providing the composition NiAl, known as the β phase, Fig. 2(c). Nevertheless, due to its high melting point, low density, high thermal conductivity, and good oxidation resistance, NiAl is very attractive as a potential high-temperature structural material. Unfortunately, it suffers from the twin drawback of poor fracture resistance at low temperatures and inadequate strength

at high temperatures, both of which need to be overcome before NiAl will find extensive engineering application.

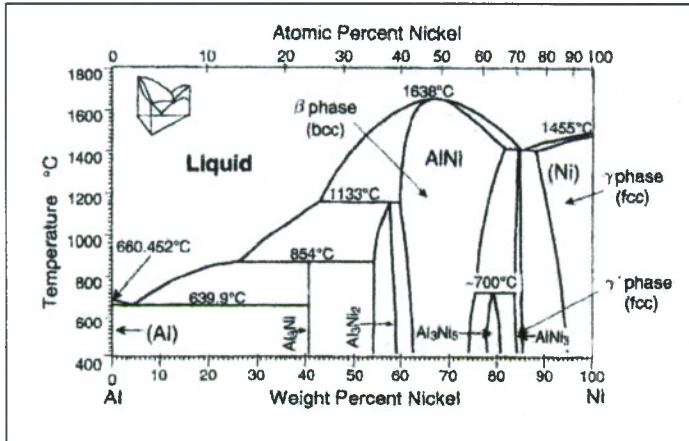


Figure 1. Ni-Al phase diagram. 2nd ed. ASM International; 1996.)

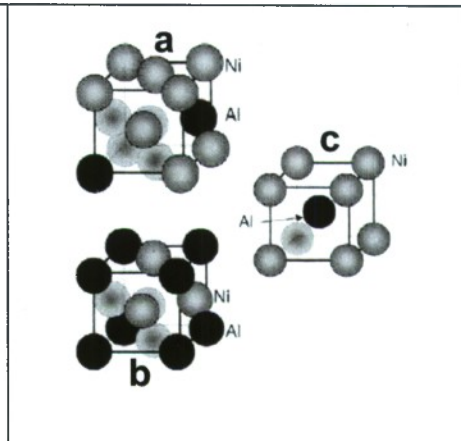


Figure 2. Effect of alloying on crystal structure

Microstructural examination of the compact in the as-cast condition revealed a no homogeneous grain size distribution, Fig. 3, with an average size of about 200 and 400 μm for as cast NiAl and NiAlNdPr respectively.

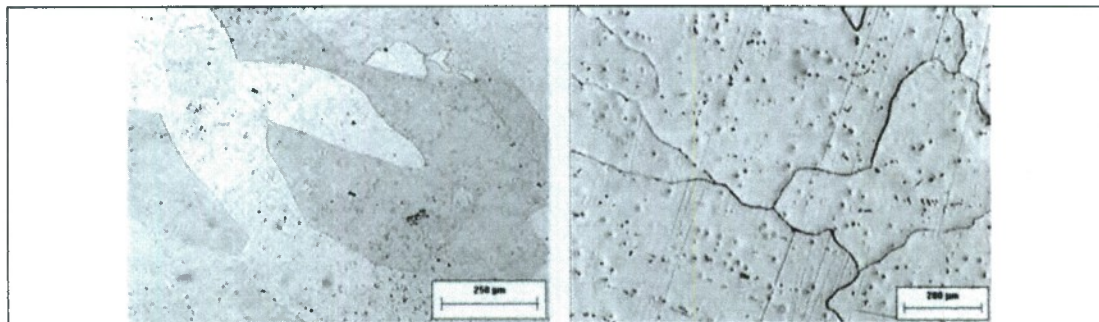


Figure 3. Some aspects of the a) as cast NiAl microstructure and b) as cast NiAlNdPr microstructure

Kinetics

Figures 4 and 5 shows the weight gain per unit area against time for NiAl and NiAlNdPr respectively; in samples oxidized in air at 800, 900, 1000 and 1100°C for a period of 48 hours. In all cases, a parabolic behavior was found and the rate constants derived for all temperatures are shown in table 1.

The kinetic results confirm the beneficial effect of Nd-Pr addition on the oxidation behavior of the NiAl intermetallic alloys. Thus, the weight change observed for NiAlNdPr at 800, 900, 1000 and 1100°C was negligible (about 0.30, 0.33, 0.56 and 0.65 mg/cm², respectively) as compared to that of NiAl at 800, 900, 1000 and 1100°C (3.50, 6.05, 8.6 and 9.80 mg/cm², respectively). NiAl specimens showed cracking on the scale surface under exposition for 48h. Irrespective of temperature, the kinetic constants in this work are about fourteen times below the ones without the addition of Nd and Pr, on the oxidation behavior of NiAl intermetallic alloys. Thus, according with the present results, the addition of Nd-Pr helps to decrease the oxidation kinetics, probably by avoiding massive diffusion of Al towards the intermetallic/environment interface.

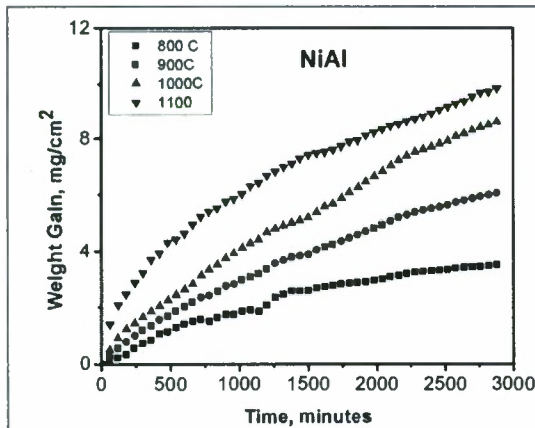


Fig.4. Kinetic data for the isothermal oxidation of NiAl intermetallic alloy during oxidation in air at 800, 900, 1000 and 1100°C for 48h.

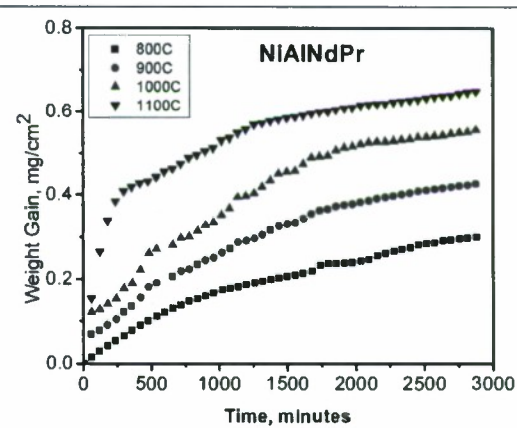


Fig.5. Kinetic data for the isothermal oxidation of NiAlNdPr intermetallic alloy during oxidation in air at 800, 900, 1000 and 1100°C for 48h.

The parabolic rate constant (K_p) is related to the weight gain ($\Delta W/A$) and exposure time (t) by the following relation:

$$(\Delta W/A)^2 = K_p t + c \quad (1)$$

where c is a constant. The rate constant K_p was obtained from the slope of the linear regression-fitted line of $(\Delta W/A)^2$ vs t plot. The rate constants are provided in table 1 for the experiments performed in this study.

Table 1. Oxidation rate constant k_p of NiAl and NiAlNdPr intermetallic alloy at different temperatures.

Intermetallic Alloys	$K_p, g^2cm^{-4}s^{-1}$	$K_p, g^2cm^{-4}s^{-1}$	$K_p, g^2cm^{-4}s^{-1}$	$K_p, g^2cm^{-4}s^{-1}$
	800°C	900°C	1000°C	1100°C
NiAl	7.95×10^{-11}	2.28×10^{-10}	4.55×10^{-10}	5.50×10^{-10}
NiAlNdPr	5.47×10^{-13}	1.14×10^{-12}	1.93×10^{-12}	1.72×10^{-12}

Fig. 6 shows the change in the experimentally determined values of K_p with the temperature for NiAl and NiAlNdPr intermetallic alloys respectively. It is a normal practice to correlate the overall parabolic rate constant (K_p) and temperature through an Arrhenius-type equation:

$$K_p = K_0 \exp(-Q/RT) \quad (2)$$

Where R is the universal gas constant, K_0 the pre-exponential factor. T is the absolute temperature and Q is the activation energy.

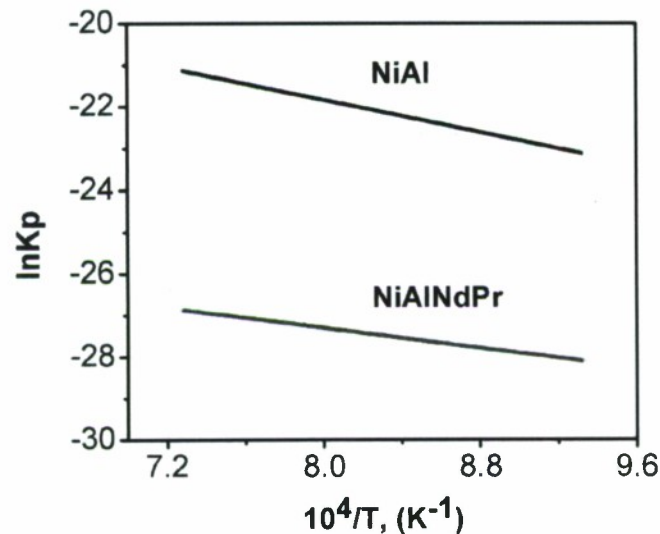


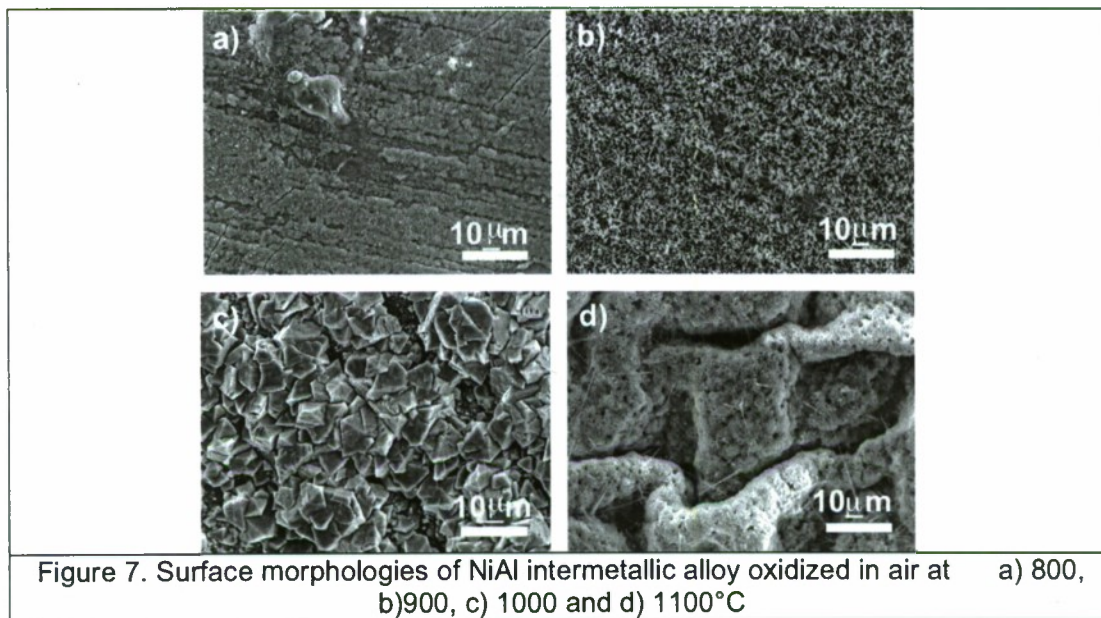
Figure 6. Activation energy for NiAl and NiAlNdPr intermetallic alloys

The activation energies for this system were $Q_{NiAl}=81$ and $Q_{NiAlNdPr}=50$ KJ/mol. Babu et al. found an activation energy of 92 kJ/mol for oxidation kinetics of Fe25Al

[14]. In all cases it can be seen that the smallest kinetics was found in samples with the addition of REEs also the behavior was parabolic, figure 6.

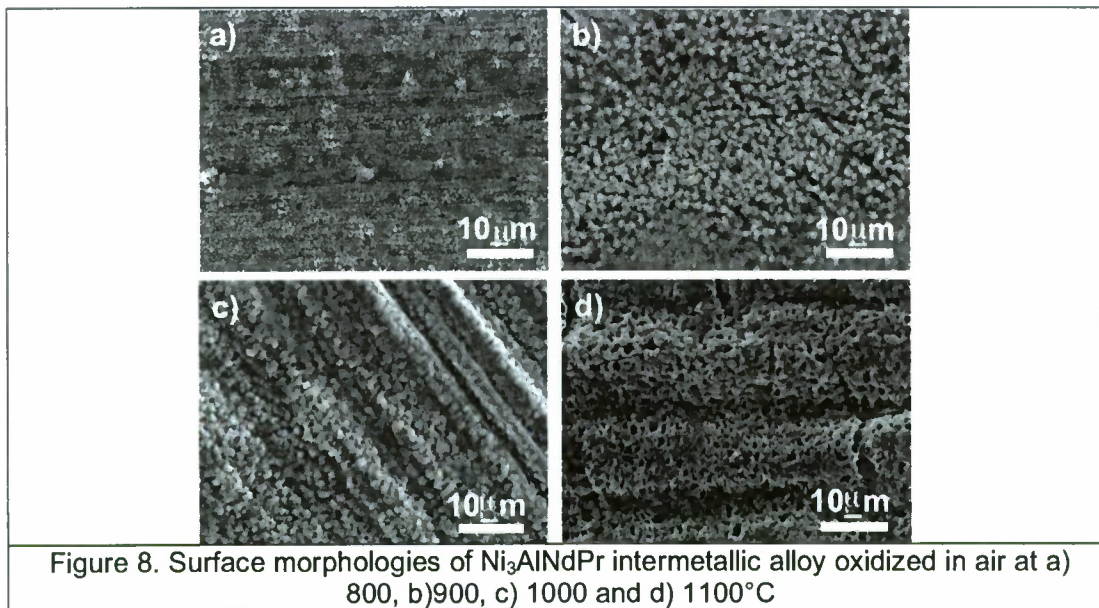
Morphology

In the present study, it was clearly observed that the nature of the formed scale on the binary intermetallic changed with temperature. This was also evident from morphological observations in the SEM after the NiAl specimens had been oxidized during 48h (fig. 7), Spalling of scale was more pronounced at the lower oxidation temperatures. After oxidation at 800C, the surface oxide morphology consisted mainly of granular oxides (fig. 7a) while, after 900°C oxidation crystal chains-like scales (extrinsic ridges structure) were observed. (fig.7b), at 1000°C oxidation spalling of scales was observed and some plate-like aluminum oxide were founded on the top surface (fig.7c) and convoluted morphology during oxidation at 1100°C for 48 h (fig. 7d).



Microalloying of REE's can significantly improve the oxidation resistance of Ni₃Al based alloy. Compared with REE's-free alloys, the oxidation rate of REE's-containing alloys was sharply reduced and slight spallation signs existed on the surfaces of oxide scales, Scales were sometimes granular, ridges-like (fig. 8a, b

and c) and convoluted during oxidation at 1100°C for 48 h (fig. 8d). To understand the function of microalloying constituents during the growth of oxide scales, extensive studies have been conducted by many researchers. Graboski and Rehin [15] summarized oxidation behavior of metals and alloys implanted with various elements. They have found that only implanted yttrium has significant beneficial effects on oxidation resistance. Some beneficial effects of additions of Y, Ce, Hf, Y_2O_3 , HfO_2 , and CeO_2 on the development of protective oxide scales were founded by using surface salt-deposit techniques [16] and conventional alloying techniques. [17-22] Some other reactive elements, such as Th, Zr and La, also showed some influence on oxidation behavior; however, only a few studies were conducted on those elements.



In fig. 9 is shown the backscattered image of the cross-section of $NiAl$ intermetallic alloy oxidized in air at 1100°C during 48h with X-ray maps of Al, Ni and O. In this figure it can be seen a great internal oxidation beneath the convoluted Al_2O_3 oxide.

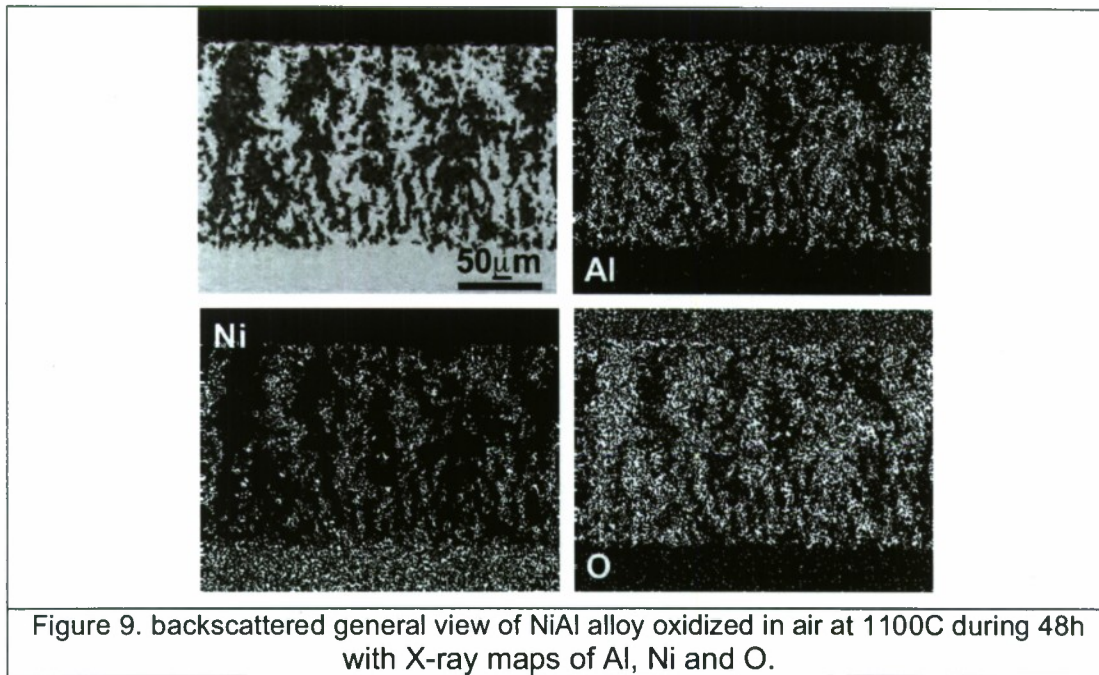
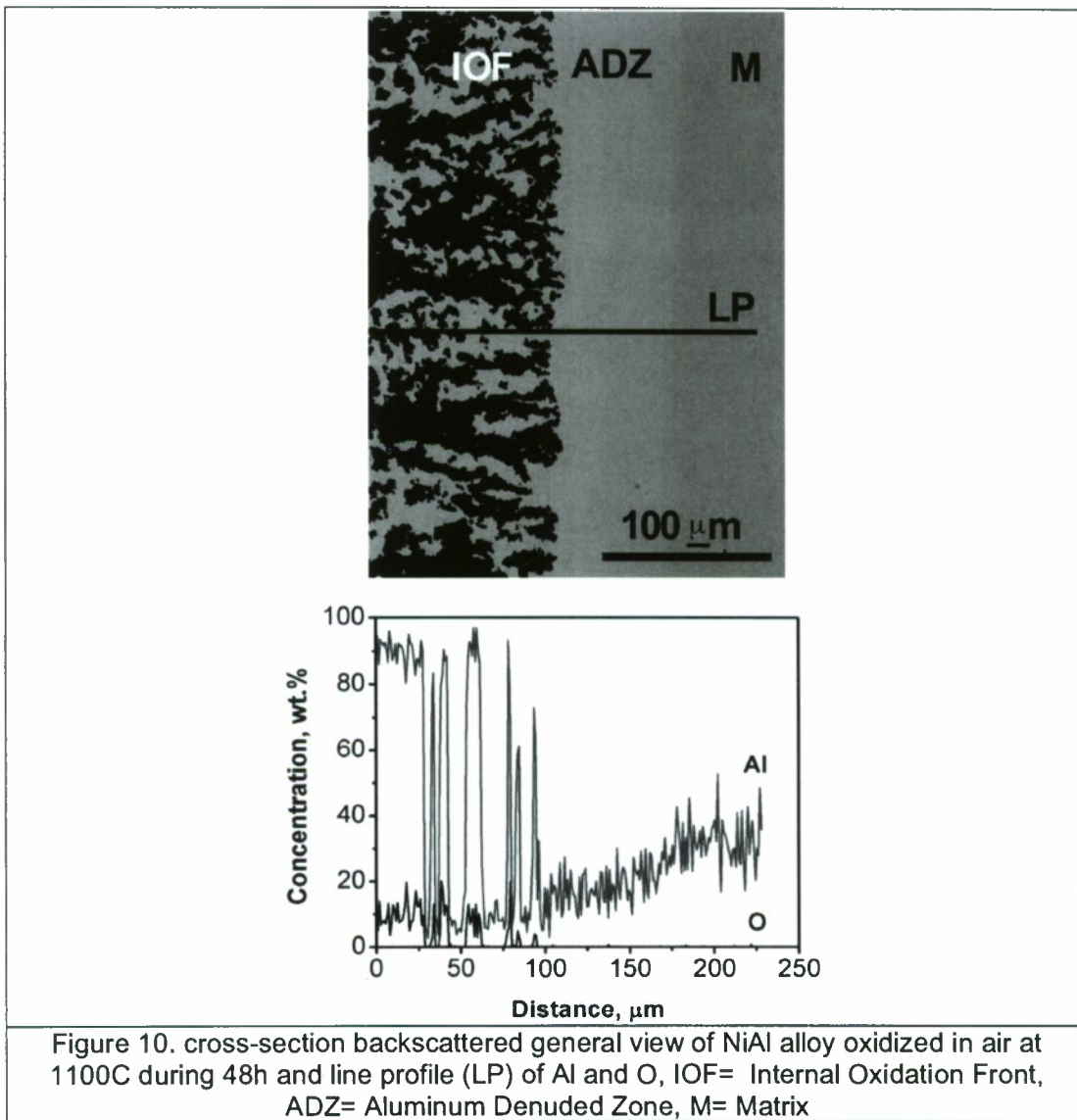
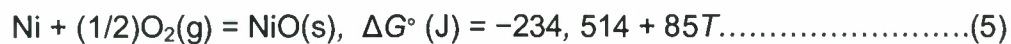
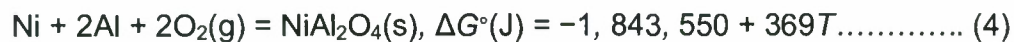
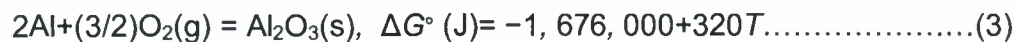


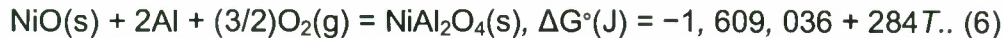
Figure 10 shown the cross-section backscattered general view of NiAl alloy oxidized in air at 1100C during 48h and line profile (LP) of Al and O. In this figure it can be seen three regions the first one is the internal oxidation front (IOF), the second one is an aluminum depleted zone with a 100μm wide and the concentration of Al dropped from 30 to 15 wt.%. the third one is matrix region.



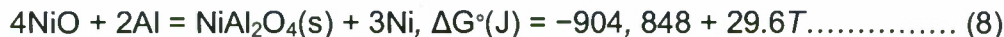
There are several potential oxidation reactions, when Ni–Al alloys are kept in oxygen-containing environments at elevated temperatures. The formations of these oxides (Al_2O_3 , NiO , and NiAl_2O_4) are governed by their free energies of formation ' ΔG° '; the following reactions are possible [21]:



Eqs. (3) and (4) may combine to:



As the oxidation process continues, equilibrium between the alloy surface and the oxide phase is approached and the stability of the oxide nuclei determined by the composition of the alloy at the alloy/oxide interface is based on the following reactions [7]:



Combining Eqs. (7) and (8), we have:



The more negative the free energy of a given oxidation reaction the more spontaneous the reaction will be and the oxide phase resulting from this reaction is said to be more thermodynamically stable. Al_2O_3 and NiAl_2O_4 are considered the most stable oxide phases from the thermodynamic point of view. The alumina may form as a result of an oxidation reaction between Al atoms already present at the surface or diffuses across an existing oxide layer to react with O_2 gas at the oxide–gas interface. The NiAl_2O_4 may result from either the oxidation reaction between Ni and Al or Al and NiO already formed at the surface with the O_2 gas, respectively. Also, the positive ΔG° of NiAl_2O_4 resulting from the chemical reaction between NiO and Al_2O_3 suggest that NiAl_2O_4 would decompose to NiO and Al_2O_3 spontaneously [7].

The morphological observations and microanalyses suggest that Nd plus Pr have an effect on prevention of outward diffusion of cations through the short-circuit paths during oxidation, which prevents cavities forming near substrate–oxide interface, so that the alloy shows a dramatic improvement in scale adhesion. Nd and Pr addition can refine the oxide grains and reduce the formation of nickel or spinel oxides in the alumina scale.

CONCLUSIONS

The present work provided a detailed comparison of the oxidation performance of Ni₃Al with and without Nd and Pr in air in the temperature range of 800–1100°C. The results based on specimen weight gain and microstructural characterizations indicated that Nd and Pr additions significantly improved the oxidation resistance of these alloys.

The oxidation behavior of a NiAl and NiAlNdPr intermetallic alloys in static air at 800, 900, 1000 and 1100°C followed a parabolic kinetic behavior.

The kinetic constants for NiAl intermetallic alloys without the addition of Nd and Pr were about thirty times higher than those with these elements regardless the temperature.

The activation energies for this system were $Q_{\text{NiAl}}=81$ and $Q_{\text{NiAlNdPr}}=50$ KJ/mol

Nd and Pr additions improved the adherence of the α -Al₂O₃ scale.

The morphology of the oxides formed on specimens with and without REEs varies significantly from fine-grained, plate-like and ridges-like to convoluted oxide.

It was found an internal oxidation with an Al depleted region.

REFERENCES

1. V.K. Sikka, M.L. Santella, J.E. Orth, Mater. Sci. Eng. A 239–240 (1997)564–569.
2. V. Shankar Rao, J. Mater. Sci. (2004) 4193–4198.
3. D. Zhang, Z. Cai, G. Adam, S. Raynova, Z. Liu, J. Met. 56 (2004) 271.
4. J. Lapin, M. Nazmy, Mater. Sci. Eng. A 380 (2004) 298–307.
5. S. Deevi, V. Sikka, Proceeding of the International Symposium on Nickel and Iron Aluminides: Processing, Properties and Applications, 1997, p.283.
6. J. Gawel, Oxid. Met. 30 (3/4) (1988) 139–140.
7. W.H. Lee, R.Y. Lin, Mater. Chem. Phys. 77 (2002) 86.

8. K. Natesan, F. Tortorelli, High-temperature corrosion and applications of nickel and iron aluminides in coal-conversion power systems, in: Proceedings of the International Symposium on Nickel and Iron Aluminides: Processing, Properties, and Applications, Materials Week 96, Cincinnati, October 7–9, 1996, 1997, pp. 265–280.
9. J.V. Cathcart, The Oxidation of Nickel–Aluminium and Iron–Aluminium Alloys, Materials Research Society Symposium Proceeding, vol. 39, 1985, pp. 445–459.
10. B.A. Leyens, I.G. Pint, Surf. Coat. Tech. 133–134 (2000) 15–22.
11. Materials Science and Technology. A Comprehensive Treatment. Edited by. R.W.Cahn, P. Haasen and E.J. Cramer. Corrosion and Environmental Degradation Vol. II. Wiley- VCH Weinheim. ISBN 3-527-20505-4. Federal Republic of Germany. 2000.
12. S. Taniguchi and T. Shibata, Influence of Si or Ti addition to Fe-23Cr-5Al Alloy Protectiveness of Preformed Al₂O₃ Scale Against Sulfidation, Trans. Japan, Institute of Metals. Vol.29, No. 8, pp. 658-664. 1988.
13. Binary alloys phase diagrams. 2nd ed. ASM International; 1996. On CD Rom.
14. N. Babu, R. Balasubramaniam, A. Ghosh. High Temperature Oxidation of Fe₃Al-based iron aluminides in oxygen. Corrosion Science 43 (2001) 2239–2254.
15. K.S. Graboswski and L.E. Rehin, in Corrosion of Metals Processed by Directed Energy Beams. Warrendale, Pa., pp.23-24, 1982.
16. M. Landkof, A.V. Levy, D.H. Boone, R. Gray and E. Yaniv. The Effect of Surface Additives on the oxidation of Chromia Forming Alloys. Corrosion. Vol. 41, pp.344-356.1985.
17. H.H. Davis, H.C. Grahman and I.A. Kvernes. Oxidation Behavior of Ni-Cr-1ThO₂ Alloys at 1000 and 1200C. Oxid. Met. Vol.3 pp. 431-452. 1971.
18. J. Stringer, B.A. Wilcox and R.I. Jaffee. The High Temperature Oxidation of Ni-20wt.%Cr Alloys Containing Dispersed Oxide Phases. Oxid. Met. Vol.5 pp. 11-34. 1972.
19. F.A. Golightly, G.C. Wood and F.H. Stott. Early Stages of Development of α -Al₂O₃ Scales on Fe-Cr-Al and Fe-Cr-Al-Y Alloys at High Temperatures. Oxid. Met. Vol.14. pp. 217-234. 1980.
20. T.A. Rannanarayanan, M. Raghavan and R. Petrovic-Luton. Metallic Yttrium Additions to High Temperature Alloys: Influence of Al₂O₃ Scale Properties. Oxid. Met. Vol.22. pp. 83-100. 1984.
21. High-temperature characterization of reactively processed nanostructure nickel aluminide intermetallics. Journal of Alloys and Compounds 440 (2007) 178–188.
22. S.O. Moussa, K. Morsi. High-temperature oxidation of reactively processed nickel aluminide intermetallics. Journal of Alloys and Compounds 426 (2006) 136–143

CHAPTER 6

HIGH TEMPERATURE OXIDATION BEHAVIOR OF TiAl AND TiAlNdPr INTERMETALLIC ALLOYS.

ABSTRACT

The effect of rare earth elements (REE's) i.e. Neodymium (Nd) and Praseodymium (Pr) on the oxidation behavior of a TiAl intermetallic alloy with and without rare earths has been evaluated, and its role on the oxidation rate and oxide morphology and formation is discussed. Specimens were isothermally oxidized in air at 800, 900, 1000, and 1100°C for 48 h. It was found that a simultaneous addition ($\leq 0.03\text{wt.}\%$) of both Nd and Pr, reduced the oxidation rate of the TiAl intermetallic alloy. Analysis by scanning electron microscopy (SEM) revealed that the morphology of oxides formed on TiAl intermetallic alloy specimens with and without REE's was very different. For these alloys mainly, aluminum enrichment at the metal/scale interface was observed.

INTRODUCTION

There are several potential applications that have been identified for TiAl-based alloys in the aerospace, automotive and turbine power generation markets. Aircraft engine manufacturers are pursuing the implementation of these alloys in aircraft engines. The earliest major work on gamma alloy development was initiated by the U.S. Air Force Materials Laboratory. This research, conducted by Pratt and Whitney from 1975-1983, recommended Ti-48Al-1V-(0.1C) as the best alloy composition based on ductility and creep resistance. The second major development program, again initiated by the Air Force and performed by General Electric from 1986-1991 identified a second generation of alloys, Ti-48Al-2(Cr or Mn)-2Nb with improved ductility, strength, and oxidation resistance [1]. In 1993, GE conducted successful engine tests on a full-set wheel of gamma blades, which improved overall confidence in the material [1,2].

The initial processing route for fabrication of gamma components was investment casting. However, this processing route can lead to fluctuations in the Al content of more than ± 2 at.-%, leading to a non-uniform microstructure, and a significant variation in the mechanical properties [3]. Powder metallurgy (P/M) technologies, on the other hand, provide more precise control of composition and microstructure, as well as helping reduce fabrication costs [4, 5]. More recently, developments in P/M methods and alloying combinations have led to the production of prematerial that can be used for sheet rolling [3, 6, 7]. Plansee AG developed an Advanced Sheet Rolling Process (ASRP), which allows processing on a conventional hot-rolling mill at low rolling speeds, producing thin sheet material with homogenous alloy composition [6]. Using this patented process, Plansee produces sheets of 1mm thickness which are commercially available. In addition, small foils with a thickness down to ~ 150 μm have been rolled [6]. Recent extensive engine tests of components of TiAl-based alloys such as low-pressure turbine blades have revealed that no serious limitations exist to aircraft engine applications of TiAl-based alloys [8, 9]. The automotive community is pursuing the qualification and introduction of exhaust valves and turbocharger turbine wheels of TiAl-based alloys for automotive engines. Very recently TiAl turbocharger turbine wheels have started to be used for commercial cars of a special type [10]. Thus, these high-temperature structural aluminides are entering the first phase of structural applications.

Intermetallic compound phases identified in Ti-Al alloys, $\text{Ti}_3\text{Al}(\alpha_2)$, $\text{TiAl}(\gamma)$, Al_2Ti and Al_3Ti phases are stable at room temperature and their mechanical properties have been investigated using single-phase specimens. TiAl-based alloys with two-phase structures consisting of the major γ and minor α_2 phases are the most intensively studied materials among these aluminides and their alloys. There are two reasons for this. Firstly, their low density, strength and modulus retention at high temperatures, some tensile ductility at room temperature, and reasonably good oxidation resistance are very attractive as a new class of light-weight high-temperature materials for structural applications. Secondly, TiAl-based alloys can

be processed more or less similarly to metals and alloys through conventional manufacturing processes such as ingot melting, casting, forging, precision casting and machining on almost conventional equipment [8-11].

The good oxidation resistance of these materials is based on their ability to develop a protective alumina layer (Al_2O_3) on their surface in many high-temperature environments. Because alloys based on TiAl and Ti₃Al form Al_2O_3 during exposure to oxidizing gases, they typically display low oxidation rates when compared to iron-based and other alloys that do not form alumina in similar conditions. Recent research showed that the rare earth element Y can refine microstructure and improve oxidation resistance of TiAl alloys [12-14]. The application properties of TiAl-intermetallics based alloys depend not only upon the chemical composition of the alloy but also on their structures. The microstructure classification of Ti–Al alloys was suggested by Clemens et al. [15]. The structure type can be duplex (fine-grained microstructure) or lamellar (fully lamellar and nearly lamellar) microstructure. Alloy with the duplex structures inhibits good plasticity, however the fully lamellar and nearly lamellar structures are usually coarse-grained, which causes that the alloy has good creep resistance, but at the same times it results in poor ductility, particularly at room temperatures [15,16]. The ductile properties concerned can be achieved by applying various processing methods. Components made of TiAl based alloys can be processed by casting, hot-working as well as powder metallurgical processing methods [17-18].

The heat resistance of these alloys is affected by their operating conditions and the composition of the oxidizing environments. Heat resistance is lower in air, rather than in pure oxygen. This system from the fact that nitrogen present in air highly diffuses into the substrate [19].

Construction elements in a device can operate not only in high temperatures, but also under conditions that require periodical activation and deactivation. Such cyclic oxidation may result in scale spalling and chipping, hence the local or total

loss of the protection layer is provided by intact scale. Therefore, cyclic oxidation testing has become the basis for developing specifications of materials operating at high temperatures.

The TiAl alloys produced by ingot-metallurgy processes tended to have worse oxidation behavior, since they had greater spallation than oxide-dispersion-strengthened Titanium aluminides of similar composition. In this work, a study of the oxidation behavior of ingot-metallurgy processes titanium aluminides in air has been carried out.

EXPERIMENTAL PROCEDURE

Ti-40wt.%Al (TiAl) and Ti-40wt.%Al-0.01wt.%Nd-0.01wt.%Pr (TiAlNdPr), intermetallic alloys were prepared from high purity Ti, Al, Nd and Pr elements (99.99%) in an electrical arc furnace using a purified argon atmosphere, from which rectangular strips of approximately 1.0 x 0.5 x 0.1 cm size were sectioned. The samples were cleaned and degreased. Afterwards, the surfaces were ground to 1200 grit paper, rinsed with distilled water and degreased with acetone. Each specimen was set on a platinum plate for weight-gain measurements in an electronic microbalance (sensitivity 10^{-6} g). Experiments were conducted in an atmosphere of air, a fixed temperature of 800, 900, 1000 and 1100°C (+ 2°C) and an exposure time of 48 h. The oxidized samples were analyzed using a scanning electron microscope (SEM- Jeol JSM-5800LV microscope) coupled with energy dispersive x-ray spectroscopy (EDS). These techniques are useful in understanding the oxidation phenomena in terms of scale morphology and distribution products.

RESULTS AND DISCUSSION

Structure and Microstructure

Figure 1. Shows the binary equilibrium phase diagram of Ti-Al [20]. Most of the research has been focused on the Ti-(45-48)Al (at.%) composition, where balanced properties of fracture toughness, fatigue life, and tensile strength are

achieved. At the binary composition of Ti-47Al the material begins to solidify partially in the two-phase region $L \rightarrow L + \beta$, β being a disordered BCC (body centered cubic) phase. The material then goes through a transformation $L + \beta \rightarrow L + \alpha$, in which α is a disordered HCP (hexagonal closed packed) phase. The γ and α_2 lamellae in the lamellar microstructures are stacked such that a $\{111\}\gamma$ plane is parallel to $(0001)\alpha_2$ and the closely packed directions on $\{111\}\gamma$ are parallel to those on $(0001)\alpha_2$. However, the $[110]$ direction and the other two $[10\bar{1}]$ and $[0\bar{1}1]$ directions on (111) in the γ phase are not equivalent to each other because of the tetragonal $L1_0$ structure of the γ phase [Fig. 2(a)] while directions of $\langle 11\bar{2}0 \rangle$ on the basal plane in the α phase (h.c.p.) and α_2 phase (hexagonal $D0_{19}$) are all equivalent [Fig. 2(b)]. Thus, when the γ phase precipitates from the aparent phase, the $L1_0$ structure can be formed in six orientation variants corresponding to the six possible orientations of the $[110]$ direction along a reference $\langle 11\bar{2}0 \rangle$ direction of the α phase and thus of the α_2 phase [21].

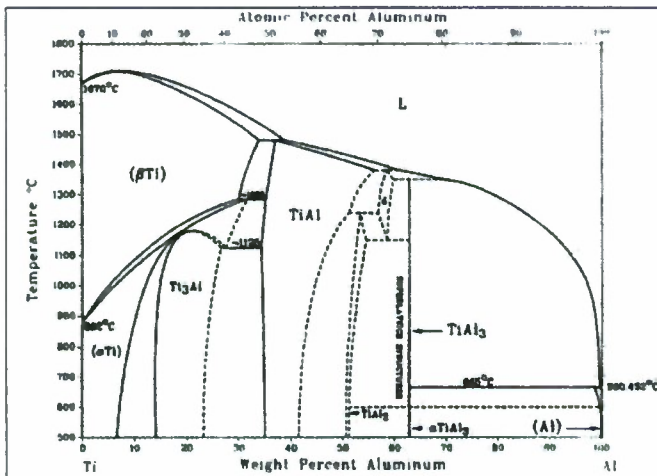


Figure 1. Equilibrium phase diagram of TiAl (20)

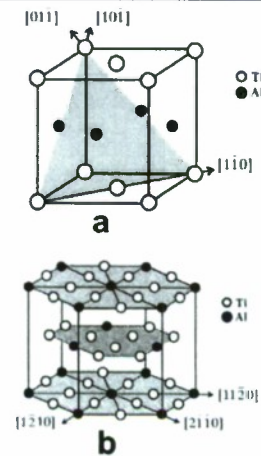


Fig. 2. Crystal structures of the (a) $L1_0$ and (b) $D0_{19}$ types.

Figure 3, shows the typical microstructure of the alloy as cast ingots. Both ingots have a lamellar microstructure, which is characteristic of cast $\gamma + \alpha_2$ alloys and is represented by alternating γ and α_2 lamellae. Microstructure of the TiAl intermetallic alloy without REEs (Fig. 3a) has irregularly coarse grains with some

needle-shaped precipitates. Besides, microstructure of the TiAlNdPr as cast alloy with REE's presented a quite different morphology with small grain size needle-shaped precipitates (Fig. 3b).

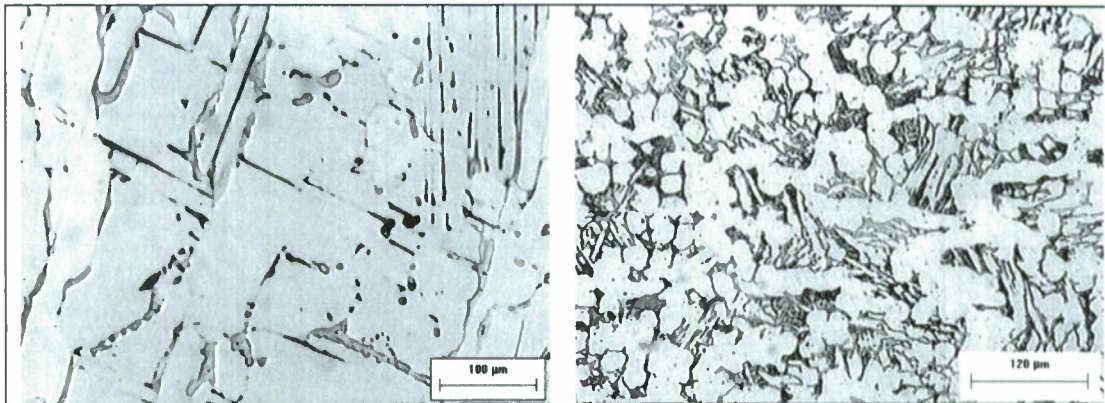


Figure 3. Some aspects of the TiAl and TiAlNdPr intermetallic alloys as cast microstructure

Kinetics

Figures 4 and 5 shows the weight gain per unit area against time for TiAl and TiAlNdPr respectively; in samples oxidized in air at 800, 900, 1000 and 1100°C for a period of 48 hours. In all cases, a parabolic behavior was found and the rate constants derived for all temperatures are shown in table 1.

The kinetic results confirmed the beneficial effect of Nd-Pr addition on the oxidation behavior of the TiAl intermetallic alloys. Thus, the weight change observed for TiAlNdPr at 800, 900, 1000 and 1100°C was negligible (about 0.33, 0.41, 0.57 and 0.70 mg/cm², respectively) as compared to that for TiAl at 800, 900, 1000 and 1100°C (4.50, 8.07, 23.40 and 36.30 mg/cm², respectively). Regardless the temperature the kinetic constants in this work were about forty times lower for the alloys without the addition of Nd and Pr, on the oxidation behavior of TiAl intermetallic alloys. Thus, according with the present results, the addition of Nd-Pr helped to decrease the oxidation kinetics, probably by avoiding massive diffusion of Al towards the intermetallic/environment interface. Values of k_p were calculated from plots of square weight-change data versus time. Activation energy for were determined from the plot of parabolic rate law constants (k_p) in an Arrhenius

diagram. The weight gain per unit area as a function of time, i.e. ($\Delta W/A$) versus t , constituted the primary data and curves are shown in fig.4 and 5 for TiAl and TiAlNdPr respectively. The parabolic rate law was first considered as the basis of data processing and interpretation of results in this research work.

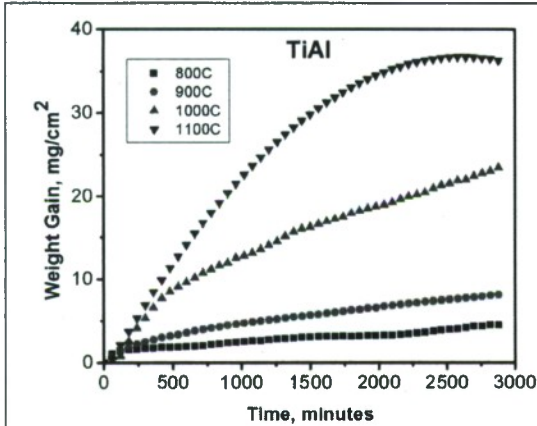


Fig.4. Kinetic data for the isothermal oxidation of TiAl intermetallic alloy during oxidation at 800, 900, 1000 and 1100°C for 48h.

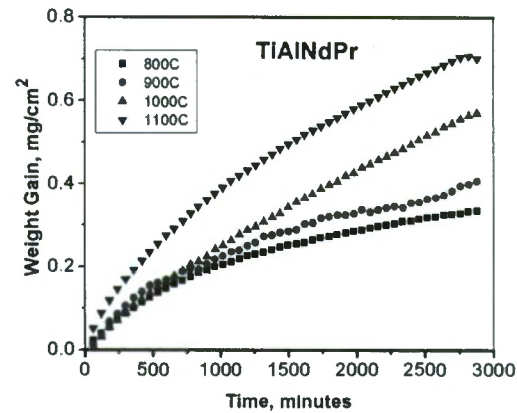


Fig.5. Kinetic data for the isothermal oxidation of TiAlNdPr intermetallic alloy during oxidation at 800, 900, 1000 and 1100°C for 48h.

The parabolic rate constant (K_p) is related to the weight gain ($\Delta W/A$) and exposure time (t) by the following relation:

$$(\Delta W/A)^2 = K_p t + c \quad (1)$$

where c is a constant. The rate constant K_p was obtained from the slope of the linear regression-fitted line of $(\Delta W/A)^2$ vs t plot. The rate constants are provided in table 1 for the experiments performed in this study.

Table 1. Oxidation rate constant k_p of TiAl and TiAlNdPr Intermetallic alloys at different temperatures.

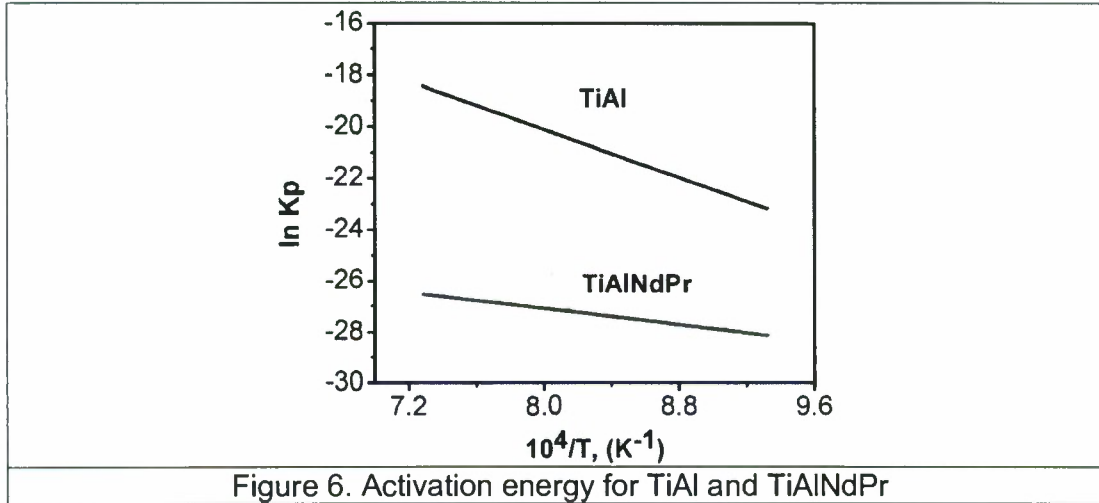
Intermetallic Alloys	$K_p, g^2cm^{-4}s^{-1}$	$K_p, g^2cm^{-4}s^{-1}$	$K_p, g^2cm^{-4}s^{-1}$	$K_p, g^2cm^{-4}s^{-1}$
	800°C	900°C	1000°C	1100°C
TiAl	1.01×10^{-10}	3.78×10^{-10}	3.25×10^{-9}	9.50×10^{-9}
TiAlNdPr	6.78×10^{-13}	9.32×10^{-13}	3.08×10^{-12}	3.12×10^{-12}

Fig. 6 shows the change in the experimentally determined values of K_p with the temperature for TiAl and TiAlNdPr intermetallic alloys respectively. It is a normal practice to correlate the overall parabolic rate constant (K_p) and temperature through an Arrhenius-type equation:

$$K_p = K_0 \exp(-Q/RT) \quad (2)$$

Where R is the universal gas constant, K_0 the pre-exponential factor. T is the absolute temperature and Q is the activation energy.

The activation energies for this system were $Q_{\text{TiAl}}=193$ and $Q_{\text{TiAlNdPr}}=71$ KJ/mol. Babu et al. found an activation energy of 92 kJ/mol for oxidation kinetics of Fe25Al [22]. The activation energy values collected from the present kinetics data are in agreement with Babu's values.

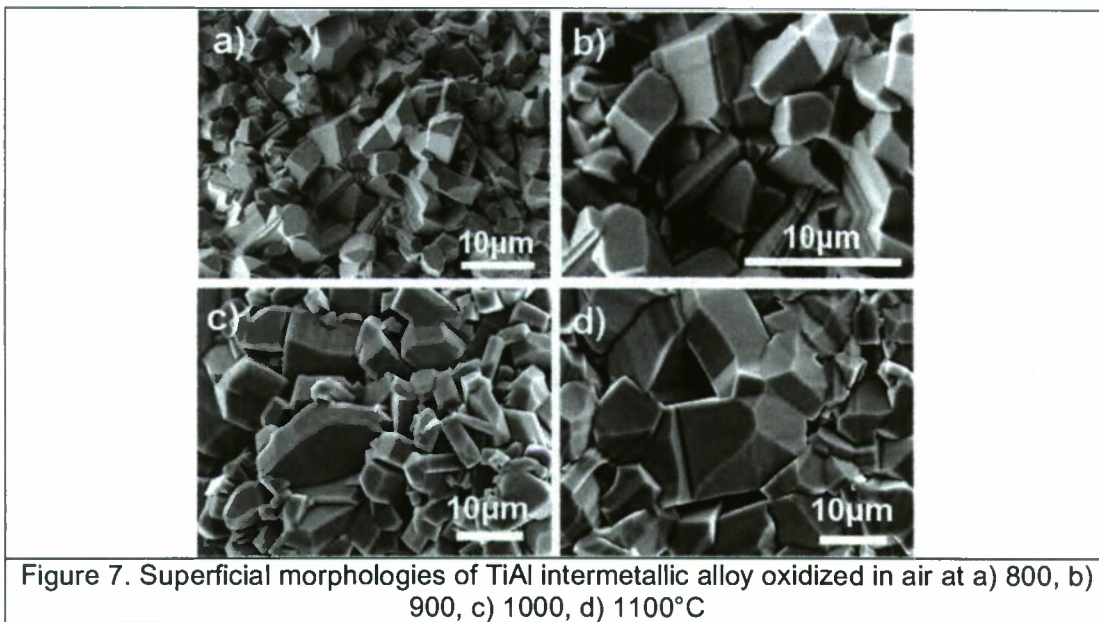


Morphology

In the present study, it was clearly observed that the nature of the formed scale on the binary intermetallic alloy do not presented changed with temperature. This was also evident from morphological observations in the SEM after the TiAl specimens had been oxidized during 48h (fig. 7). The oxidation characteristics of titanium aluminides at high temperatures are a major concern. In general, unlike Ni-Al

alloys, a protective Al_2O_3 layer does not form on all the Ti-Al alloys because both Ti and Al form oxides of very similar stability. Aluminum forms a very slow growing $\alpha\text{-Al}_2\text{O}_3$, while titanium forms several oxides (TiO , TiO_2 , Ti_2O_3 , etc.), which have relatively high growth rates. It has been observed that a protective continuous layer of alumina is formed on Ti-Al alloys containing more than the stoichiometric amount of Al. TiAl_3 is the only compound on which a protective, continuous $\alpha\text{-Al}_2\text{O}_3$ was found to exist over a wide temperature range. [23–26] A nonprotective TiO was found to be the major oxide constituent on the surface of Ti_3Al at elevated temperatures.[27,28] In the case of a TiAl stoichiometric compound, Ti-rich scales were formed at elevated temperatures resulting in an increase in the parabolic rate constant [27] by several orders of magnitude. Meier *et al.*[29] studied the oxidation behavior of TiAl in air and oxygen and observed that TiAl does not form a protective layer of $\alpha\text{-Al}_2\text{O}_3$ but forms scales composed of TiO_2 and Al_2O_3 . Their results indicate that the alloys in the Al-rich portion of the TiAl field formed a protective layer over the temperature range 1100°C to 1300°C.

In this study, isothermal oxidation of Ti-40 wt.%Al alloy was studied in air over the temperature range of 800 to 1100°C. Oxidation rate constants were obtained from the weight gain curves using the parabolic law. The oxidation product was a mixture of TiO_2 and Al_2O_3 at 900, 1000 and 1100°C. While, after 800°C oxidation the external scale was formed of aluminum oxide. The rate of oxidation was rapid at 1000 and 1100°C for TiAl intermetallic alloys without REE's.



Microalloying of REE's can significantly improve the oxidation resistance of TiAl based alloy. Compared with REE's-free alloys, the oxidation rate of REE's-containing alloys was sharply reduced and not spallation signs existed on the surfaces of oxide scales. Scales were always granular-like (fig. 8a to d) at all the temperatures.

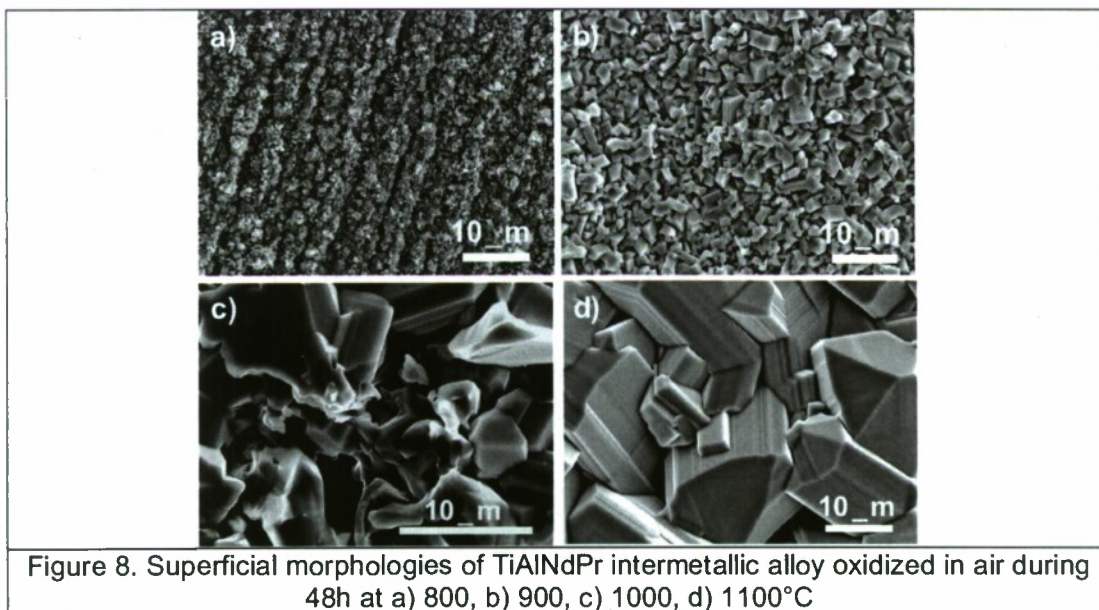


Figure 9 present the cross-section backscattered electron image (BEI) for TiAlNdPr intermetallic alloy oxidized in air at 1100°C during 48h. Also, it can be seen that the energy dispersive spectrums (EDS) for O, Al and Fe have a concentration change trough the cross-section and the grey dark precipitates were aluminum oxides and the grey light were TiO₂.

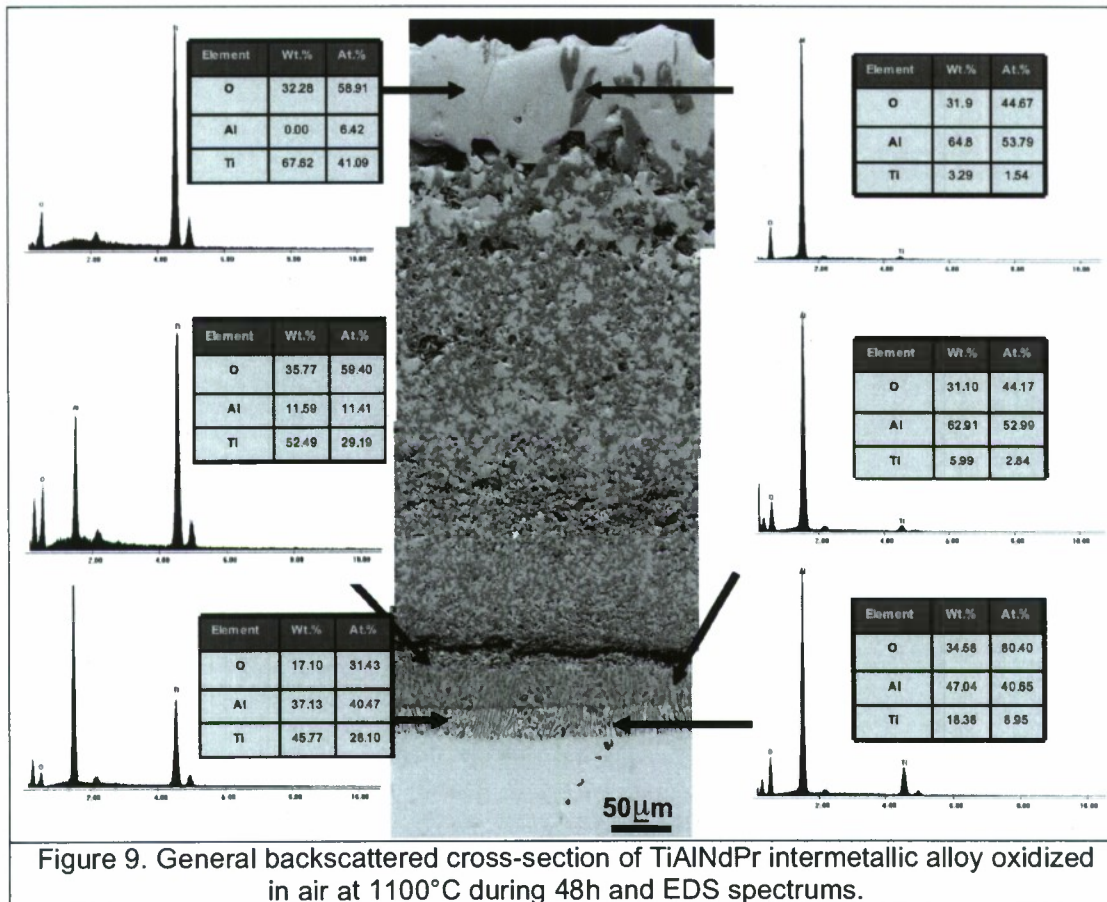


Figure 9. General backscattered cross-section of TiAlNdPr intermetallic alloy oxidized in air at 1100°C during 48h and EDS spectrums.

CONCLUSIONS

The present work provided a detailed comparison of oxidation performance of TiAl with and without Nd and Pr in air in the temperature range of 800–1100°C. The results based on specimen weight gain and microstructural characterizations indicated that Nd and Pr additions significantly improved the oxidation resistance of these alloys.

The oxidation behavior of a TiAl and TiAlNdPr intermetallic alloys in still air at 800, 900, 1000 and 1100°C, followed a parabolic kinetic behavior.

The kinetic constants for TiAl intermetallic alloys without the addition of Nd and Pr were about forty times higher than those with these elements regardless the temperature.

The activation energies for this system were $Q_{\text{TiAl}}=193$ and $Q_{\text{TiAlNdPr}}=71$ KJ/mol

Nd and Pr additions improved the adherence of the TiO_2 and $\alpha\text{-Al}_2\text{O}_3$ scale.

The morphology of the oxides formed on specimens with and without REEs does not vary in shape, However, the sizes have been changed with the temperature.

REFERENCES

1. Kim, Y.W., "Ordered Intermetallic Alloys, Part III: Gamma Titanium Aluminides." *JOM*, 1994. **46**(7): p. 30-39.
2. Kim, Y.-W., "Gamma Titanium Aluminides: Their Status and Future." *JOM*, 1995. **47**(7): p. 39-41.
3. Clemens, H. and H. Kestler, "Processing and Applications of Intermetallic γ -TiAl Based Alloys." *Advanced Engineering Materials*, 2000. **2**(9): p. 551-570.
4. Moll, J.H., C.F. Yolton, and B.J. McTiernan, "P/M Processing of Titanium Aluminides." *International Journal of Powder Metallurgy*, 1990. **26**(2): p. 149-155.
5. Zhao, L., J. Beddoes, P. Au, and W. Wallace, "Evaluations of P/M Gamma Titanium Aluminides." *Advanced Performance Materials*, 1997. **4**: p. 421-434.
6. Clemens, H., H. Kestler, N. Eberhardt, and W. Knabl, "Processing of γ -TiAl Based Alloys on an Industrial Scale," in *Gamma Titanium Aluminides 1999*, Y.W. Kim, D.M. Dimiduk, and M.H. Loretto, Editors. 1999, TMS: Warrendale, PA. p. 209-222.107
7. Seetharaman, V. and S.L. Semiatin, "Microstructures and Tensile Properties of Ti-45.5Al-2Nb-2Cr Rolled Sheets." *Materials Science and Engineering A*, 2001. **299**(1-2): p. 195-209.
8. Austin, C. M., Kelly, T. J., McAllister, K. G. and Chesnutt, J. C., in *Structural Intermetallics 1997*, ed.M. V. Nathal, R. Darolia, C. T. Liu, P. L. Martin, D. B. Miracle, R. Wagner and M. Yamaguchi. TMS, Warrendale, PA, 1997, p. 413.
9. M. Yamaguchi, H. Inui and K. ITO. High-Temperature Structural Intermetallics. *Acta Mater.* 48 (2000) 307-322.
10. London, B. and Kelly, T. J., in *Microstructure/Property Relationships in Titanium Aluminides*, ed. Y.-W. Kim and R. R. Boyer. TMS, Warrendale, PA, 1992, p. 285.
11. B.H. Li, F.T. Kong, Y.Y. Chen, J. Rare Earths 24 (2006) 352.

12. Y.Wu, K. Hagihara, Y. Umakoshi, *Intermetallics* 12 (2004) 519.
13. F.T. Kong, Y.Y. Chen, B.H. Li. Influence of yttrium on the high temperature deformability of TiAl alloys. *Materials Science and Engineering A*. Volume 499, Issues 1-2, 15 January 2009, Pages 53-57
14. J. Małacka, W. Grzesik, A. Hernas. An Investigation on Oxidation Wear Mechanisms of Ti-46Al-7Nb-0.7Cr-0.1Si-0.2Ni Intermetallic-Based Alloys. *Corrosion Science* 52 (2010) 263–272.
15. H. Clemens, H. Kestler, Processing and applications of intermetallics γ -TiAl based alloys, *Advanced Engineering Materials* 2 (9) (2000) 551–570.
16. W. Szkliniarz, A. Kosćielna, The role of heat treatment in manufacturing processes of TiAl intermetallic phase-based alloys, *Materials Engineering* 6(2003) 388–391 (in Polish).
17. G.A. Salshchev, R.M. Imayev, O.N. Senkov, V.M. Imayev, N.K. Gabdullin, M.R. Shagiev, A.V. Kuznetsov, F.H. Froes, Formation of a submicrocrystalline structure in TiAl and Ti3Al intermetallics by hot working, *Materials Science and Engineering A286* (2000) 236–243.
18. M. Thomas, J.L. Raviart, F. Popoff, Cast and PM processing development in gamma aluminides, *Intermetallics* 13 (2005) 944–951.
19. J.M. Rakowski, F.S. Pettit, G.H. Meier, The effect of nitrogen on the oxidation of γ -TiAl, *Scripta Metallurgica of Materialia* 33 (6) (1995) 997–1003.
20. Binary alloys phase diagrams. 2nd ed. ASM International; 1996. On CD Rom.
21. Yamaguchi, M. and Inui, H., in *Structural Intermetallics* 1993, ed. R. Darolia, J. J. Lewandowski, C. T. Liu, P. L. Martin, D. B. Miracle and M. V. Nathal. TMS, Warrendale, PA, 1993, p. 127.
22. N. Babu, R. Balasubramaniam, A. Ghosh. High Temperature Oxidation of Fe3Al-based iron aluminides in oxygen. *Corrosion Science* 43 (2001) 2239–2254.
23. N. Birks, G.H. Meier, and F.S. Pettit: *JOM*, 1994, vol. 46, pp. 42-46.
24. J. Subrahmanyam: *J. Mater. Sci.*, 1989, vol. 23, pp. 1906-10.
25. J.L. Smialek: *Corr. Sci.*, 1993, vol. 35 (5–8), pp. 1199-1208.
26. R.G. Reddy and X. Wen: *EPD Congr. '97*, TMS, Warrendale, PA, 1997, pp. 47-54.
27. X. Wen and R.G. Reddy: *Processing and Fabrication of Advanced Materials*, TMS, Warrendale, PA, 1996, pp. 379-89.
28. G. Welsch and A.I. Kahveci: in *Oxidation of High-Temperature Intermetallics*, T. Grobstein and J. Doychak, eds., TMS, Cleveland, OH, 1998, pp. 207-18.
29. G.H. Meier, D. Appalonia, R.A. Perkins, and K.T. Chiang: *Oxidation of High-Temperature Intermetallics*, T. Grobstein and J. Doychak, eds., TMS, Cleveland, OH, 1988, pp. 185-93.

CHAPTER 7

CORROSION BEHAVIOR OF ALLOY 718 IN MOLTEN SALTS AT HIGH TEMPERATURE

ABSTRACT

The corrosion behavior in molten salts of Inconel 718 (IN 718) superalloy was investigated by Electrochemical Impedance Spectroscopy (EIS). The corrosion test temperatures used were salt melting points of Na_2SO_4 , $80\text{V}_2\text{O}_5\text{-}20\text{Na}_2\text{SO}_4$, NaVO_3 and natural ash (collected in a power plant). Different experimental runs were made attempting to establish the material behavior. The results showed that the corrosion process was controlled by activation and in some cases by diffusion. The aggressiveness of the salts increased with temperature, as indicated for the corrosion rates values derived. On the whole, the corrosion rates were somewhat similar at the lowest test temperatures. However at 588°C the $80\text{V}_2\text{O}_5\text{-}20\text{Na}_2\text{SO}_4$ salt showed a much higher corrosion rate than that recorded for Na_2SO_4 or natural ash. The results obtained from electrochemical measurements correlated well with those corrosion degradation observed by SEM, and comments on the behavior found are made.

INTRODUCTION

It is widely recognized that high temperature corrosion is a major cause of materials degradation in industrial processes involving gases or molten salts at high temperature. Apart from the traditional weight change technique to evaluate the degree of deterioration, good progress has been done by using electrochemical techniques. Electrochemical impedance spectroscopy (EIS) is technique which has been widely used in the study of aqueous corrosion, and has proved effective in determining and understanding reaction mechanisms and kinetics of corrosion processes. Only a limited number of EIS investigations conducted during molten-salt corrosion have been reported [1-11].

Farrell et al. [1] have employed the impedance technique to study the corrosion behavior of Nimonic 75 in Na_2SO_4 and in Na_2SO_4 -1%NaCl at 750°C and 900°C. They observed that the shape of the impedance spectra has the characteristics of a diffusion-controlled reaction, which results because of the separation of the specimen from the gaseous environment by sample exposure to molten salts. By comparing the impedance at a fixed low frequency (50 mHz), the authors concluded that the corrosion rate was higher at 900°C than at 750°C or when sodium chloride was added to sodium sulfate. Gao et al. [2] also used this technique to ascertain the corrosion rate of Ni-Co alloys in Na_2SO_4 +10%NaCl. They observed a decline in the double layer resistance due to spallation of the oxide scale. Wu and Rapp [3] studied the hot corrosion of preoxidized Ni by a thin-fused Na_2SO_4 film at 1200°K (927°C) in a catalyzed 0.1%SO₂-O₂ gas mixture. By varying the specimen purity and preoxidation conditions for Ni, three distinct features of hot corrosion (passive, pseudo-passive, and active) were observed. Wu [5] further measured the double-layer capacitance at the preoxidized Ni/fused Na_2SO_4 interface. Similarly Wu et al. [4] have evaluated the corrosion resistance of commercial alloys in a Na_2SO_4 -Li₂SO₄ salt mixture at 700°C by EIS and by weight loss, finding some degree of correlation among the techniques used. Wu [5] measured the double-layer capacitance at the preoxidized Ni/fused Na_2SO_4 interface. Recently, Zeng et al. [6], have proposed four electrochemical impedance models for the responses of Pt, Ni₃Al and FeAl in molten-salt systems at the open-circuit potential. Zeng [6] concluded that for Pt in molten (Li, K)₂CO₃ at 650°C the charge transfer was the rate limiting process; the corrosion of Ni₃Al in (Li, Na, K)₂SO₄ at 700°C presented characteristics of a diffusion-controlled reaction owing to the formation of non-protective scale, and for FeAl, the data presented different behavior with time, initially being influenced by a diffusion rate-controlling process from the observance of double capacitance loops at the beginning due to formation of protective scale. In this work, the hot corrosion resistance of IN 718 was evaluated by EIS from 588°C to 900°C in order to ascertain the possible mechanisms controlling the rate of corrosion processes in Na_2SO_4 , 80V₂O₅-20Na₂SO₄, NaVO₃, and natural ash.

EXPERIMENTAL METHOD

Test samples of IN 718 alloy were prepared from a stock of mill-certified IN 718 rod (see Table I for alloy composition). Cylindrical specimens of 7mm diameter and 15 mm length were cut and polished with grit paper up to grade 800. The samples were then degreased well with acetone and then rinsed with ethanol. After drying, the specimens were stored in polyethylene zip-lock bags. The details of the experimental set-up for the electrochemical cell used in this work are given elsewhere [7]. Basically, the cell is composed of a quartz crucible 60 mm in height and 21.6 mm in internal diameter. Important elements here are: a) a reference electrode made of a platinum wire of 0.5 mm in diameter inside a quartz tube in contact with the molten salt of study (several other reference electrodes systems were tested, but this one gave the best stability response); b) an auxiliary electrode made of a platinum wire of 0.5 mm in diameter inside a mullite tube and filled with a refractory cement, and c) a IN 718 working electrode inside a mullite tube and filled with the same cement. In order to obtain electrical contact with the IN 718 working electrode a stainless steel wire (sheathed in the mullite tube) was spotwelded. A thermocouple sheathed with a quartz tube was immersed inside the test environment to monitor the temperature of each test. The corrosive atmosphere in the sealed cell was composed of Na_2SO_4 , $80\text{V}_2\text{O}_5\text{-}20\text{Na}_2\text{SO}_4$, NaVO_3 , or natural ash with melting points of 892°C , 587°C , 629°C and 756°C , respectively (see table II) and static air. A furnace capable of reaching 1100°C was used for all the tests. Impedance measurements were taken 0.5 hours after the corrosion potential was stabilized. The range of used frequencies was from 10 KHz up to 0.001 Hz, and the amplitude wave of excitement signal was of ± 10 mV with respect to the free corrosion potential. The temperatures used were 892°C , 587°C , 629°C and 756°C . After exposure to the environment, selected specimens were mounted and polished to be observed and analyzed in the Scanning electronic microscope (SEM).

Ni	Cr	Fe	Nb	Mo	Ti	Al	Mn	Si	Cu	C
54.21	19.13	17.64	4.50	3.09	0.85	0.21	0.05	0.25	0.03	0.04

Table I. Chemical composition of 718 alloy (% wt)

Salts	Melting Point
Na_2SO_4	892°C
NaVO_3	629°C
80 wt% V_2O_5 -20 wt% Na_2SO_4	587°C
Natural Ash (V_2O_5 , $\text{Na}_2\text{O} \cdot \text{V}_2\text{O}_4 \cdot 5\text{V}_2\text{O}_5$ and $\text{NaV}_6\text{O}_{15}$)	756°C

Table II. Melting point of the work salts

RESULTS AND DISCUSSION

Figure 1 shows the electrical resistivity, R_e , of Na_2SO_4 , NaVO_3 , 80 V_2O_5 -20 Na_2SO_4 , and natural ash as a function of temperature. The R_e values fall sharply when the temperature is increased from 500°C to 900°C. Above 750°C the resistivity was constant with a value of about 5 k-ohms. It is known that the lower the resistivity the higher the conductivity. This is important in order to obtain good electrical response.

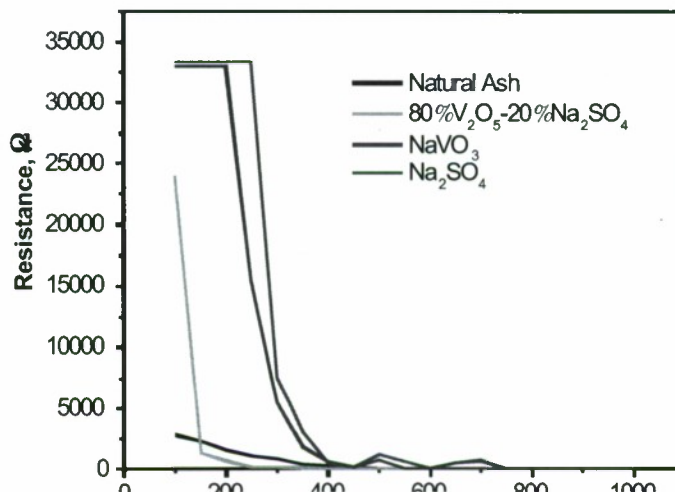


Figure 1. Resistivity of Na_2SO_4 , NaVO_3 , $80\text{V}_2\text{O}_5\text{-}20\text{Na}_2\text{SO}_4$ and natural ash a function of temperature

The test salts (Na_2SO_4 , NaVO_3 , $80\text{V}_2\text{O}_5\text{-}20\text{Na}_2\text{SO}_4$, and natural ash) were identified by X-ray diffraction with the X-ray diffractometer Siemens D5000. This analysis was carried out at the respective melting point temperatures, and at 50°C below each respective melting point of the relative salt. The aim of the X-ray diffraction was to identify the possible compounds that are generated at high temperatures for each salt and discern which compounds are more aggressive. Figure 2 shows the diffraction patterns and the identified compounds after heating salts under static air in the range of temperature of this study. Intensities correspond to compounds with a great variety of stoichiometries, as is shown in table III. In the case of NaVO_3 , $80\text{V}_2\text{O}_5\text{-}20\text{Na}_2\text{SO}_4$ and natural ash salts Intensities correspond to compounds of stoichiometry of $\text{Na}_2\text{O}\cdot\text{V}_2\text{O}_4\cdot\text{V}_2\text{O}_5$ and $5\text{Na}_2\text{O}\cdot\text{V}_2\text{O}_4\cdot 11\text{V}_2\text{O}_5$. In previous studies, it has been demonstrated that the corrosiveness shown by the different types of vanadates compounds is a function of its oxygen absorption capacity [8,12]. Particularly, two identified phases, $\text{Na}_2\text{O}\cdot\text{V}_2\text{O}_4\cdot\text{V}_2\text{O}_5$ and $5\text{Na}_2\text{O}\cdot\text{V}_2\text{O}_4\cdot 11\text{V}_2\text{O}_5$ are found among the vanadium compounds with the greatest oxygen absorption capacity as it is observed of the results of Greenert [14]. Cunningham and Brasunas [13], who reported that the $\text{Na}_2\text{O}\cdot\text{V}_2\text{O}_4\cdot\text{V}_2\text{O}_5$ compounds are more corrosive than the

$5\text{Na}_2\text{O} \cdot \text{V}_2\text{O}_4 \cdot 11\text{V}_2\text{O}_5$. Thus, the presence of these compounds will increase the corrosiveness of the salt.

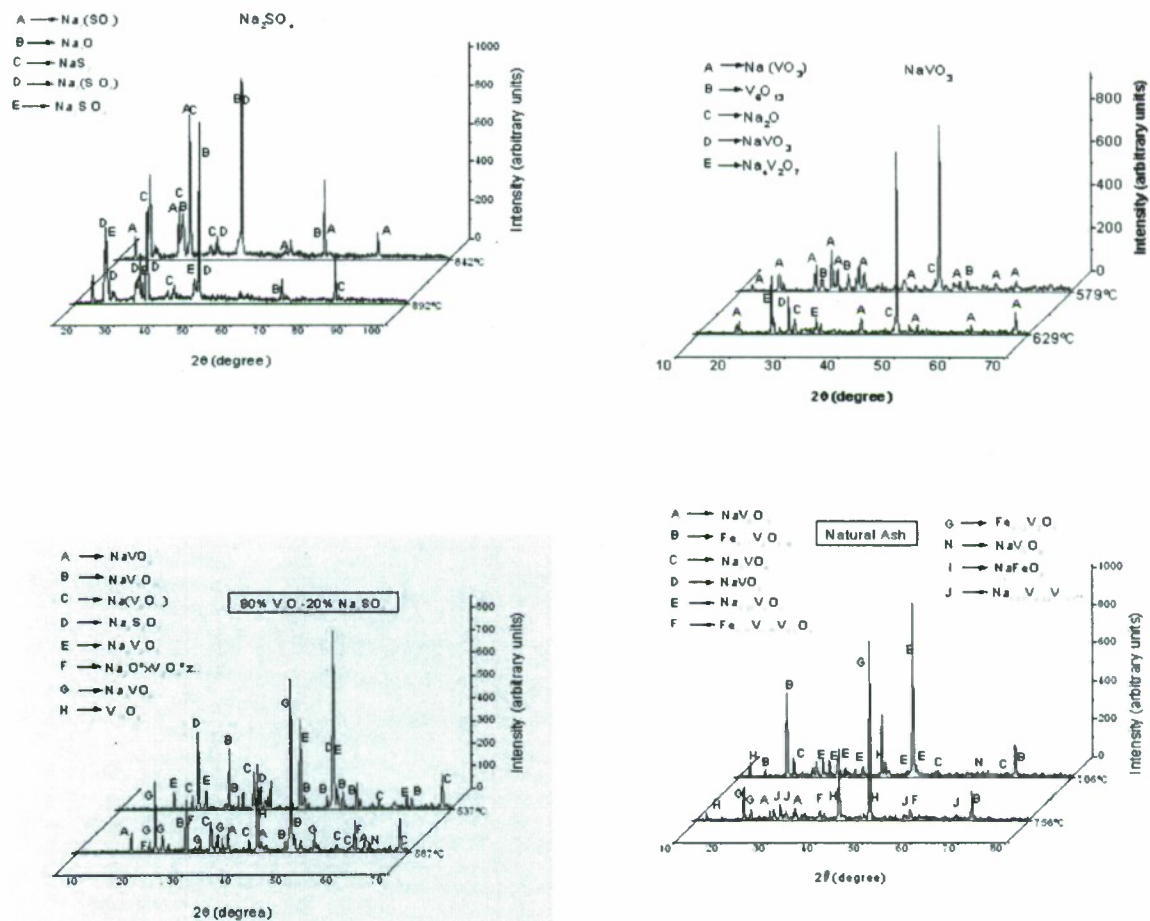


Figure 2. X-ray diffraction of the salts of work

Table III. Compounds found on the work salts at different temperatures.

Salt	Temperature °C	Compounds
Na ₂ SO ₄	842	Na ₂ (SO ₃), Na ₂ O, NaS ₂ , Na ₂ (SO ₄)
	892	Na ₂ O, NaS ₂ , Na ₂ (SO ₄), Na ₂ SO ₄
NaVO ₃	579	Na(VO ₃), V ₆ O ₁₃ , Na ₂ O
	629	Na(VO ₃), Na ₂ O, NaVO ₃ , Na ₄ V ₂ O ₇
80V ₂ O ₅ -20Na ₂ SO ₄	537	NaV ₆ O ₁₅ , Na(V ₆ O ₁₁), Na ₂ S ₂ O ₅ , Na ₄ V ₂ O ₇
	587	NaVO ₂ , NaV ₆ O ₁₅ , Na(V ₆ O ₁₁), 5Na ₂ O.V ₂ O ₄ .11V ₂ O ₅ , Na ₃ VO ₄ , V ₁₆ O ₃
Natural Ash	706	Fe _{0.11} V ₂ O _{5.16} , Na ₃ VO ₄ , Na _{0.33} V ₂ O ₅
	756	NaV ₆ O ₁₅ , Fe _{0.11} V ₂ O _{5.16} , Fe _{0.75} V _{0.75} V _{0.5} O ₄ , Fe _{0.12} V ₂ O ₅ , NaV ₃ O ₈ , Na _{0.33} V _{0.33} V _{1.67}

Fig.3 a) shows the Nyquist plots obtained for IN 718 in pure Na₂SO₄ at the different temperatures. At 50° C below the melting point, 842° C, a capacitive-like, depressed semicircle can be observed at high frequencies but at low frequencies both the real and imaginary parts describe a straight line, indicating that the corrosion process is under a mixed control: by charge transfer at high frequencies, and by diffusion control at low frequencies, diffusion of the aggressive species through the salt layer which is not melt. As the salt temperature is increased, the impedance data describe depressed, capacitive-like semicircles, with their axis in the real axis, and with their diameter decreasing as the temperature increases. This is due to the fact that at these temperatures the working salt is melted, so the diffusion of ions through it is

much easier and their transport is the rate controlling step and there is now an increased mobility of ionic charge carriers [8]. The diameter of the semicircle is

associated with the polarization resistance and thus the corrosion rate. The larger the semicircle diameter, the lower the corrosion rate. Thus, we can see that the corrosion rate increases with temperature. On the other hand, Fig. 3 b) shows the Bode diagram in the Phase angle-frequency format. It can be seen that there is one peak at 1000 Hz for 842 and 942°C and at 100 Hz for 892°C. The presence of only peaks means that no protective film is formed at any temperature and this is the reason of the increase in the corrosion rate with temperature.

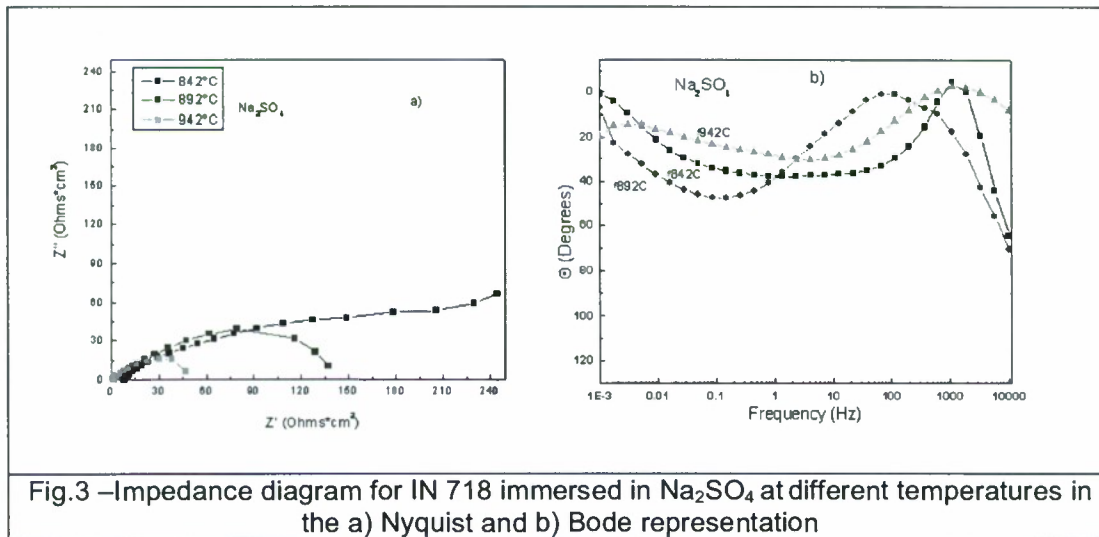


Fig.3 –Impedance diagram for IN 718 immersed in Na_2SO_4 at different temperatures in the a) Nyquist and b) Bode representation

Fig. 4 a) shows the impedance data in the Nyquist format for IN 718 superalloy exposed to NaVO_3 at its melting temperature (629°C), 579 and 679°C. This figure shows that the impedance data describe capacitive-like, depressed semicircles, with its axis in the real axis. The semicircle diameter decreases as the temperature increases, indicating that the corrosion rate increases with temperature. The shape of the semicircle indicates that the corrosion process is under charge transfer control. The Bode diagram in this case, Fig.4 b), shows only one peak around 300 Hz regardless the working temperature, indicating

that there is not the formation of a protective layer, since, in this case, a second peak should have been observed at a different frequency.

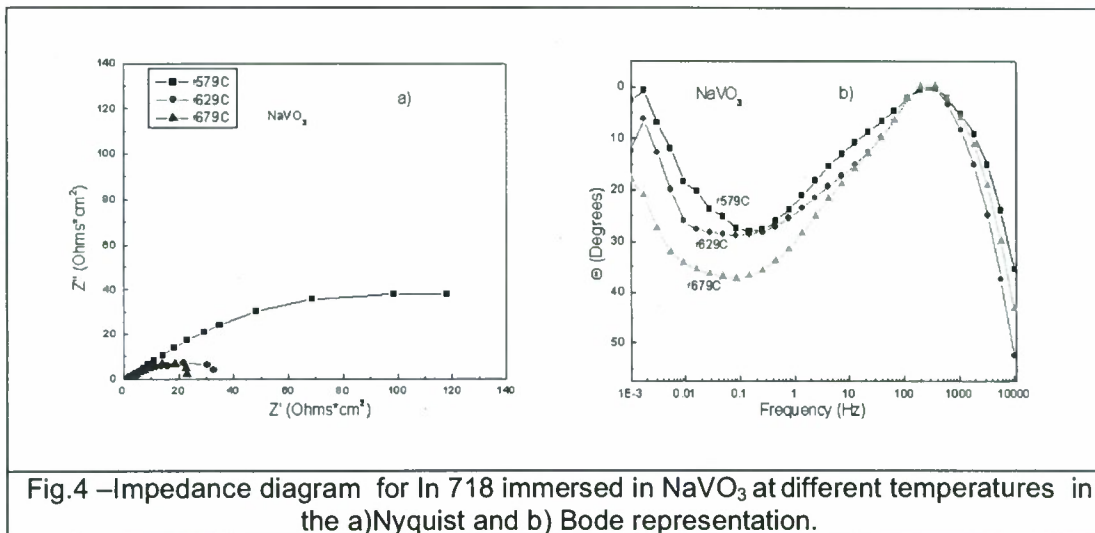


Fig.4 –Impedance diagram for In 718 immersed in NaVO_3 at different temperatures in the a)Nyquist and b) Bode representation.

When superalloy IN 718 was exposed to the $80\text{V}_2\text{O}_5+20\text{Na}_2\text{SO}_4$ mixture at its melting temperature (587°C) 637 and 687°C, the Nyquist data describe, once again, capacitive-like, depressed semicircles, with its centre in the real axis, Fig. 5 a). Unlike the previous cases, this time the semicircle diameter increased when the temperature increased, indicating that the corrosion rate decreased with temperature. The Bode diagram, Fig. 5 b), showed only one peak around 300 Hz at 537°C, but at 637 and 687°C, there seems to be a superposition of two peaks: one at 300 Hz and another one around 1 Hz. The existence of two peaks means that a protective salt layer has been formed on the alloy surface, which could explain the increase in the semicircle diameter in the Nyquist diagrams, and thus, a decrease in the corrosion rate as temperature increases.

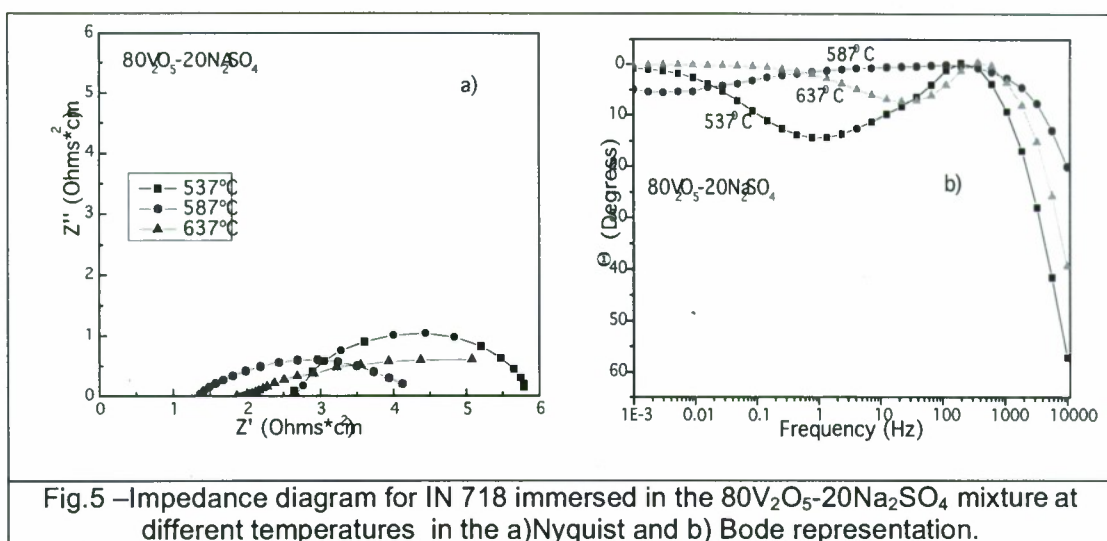
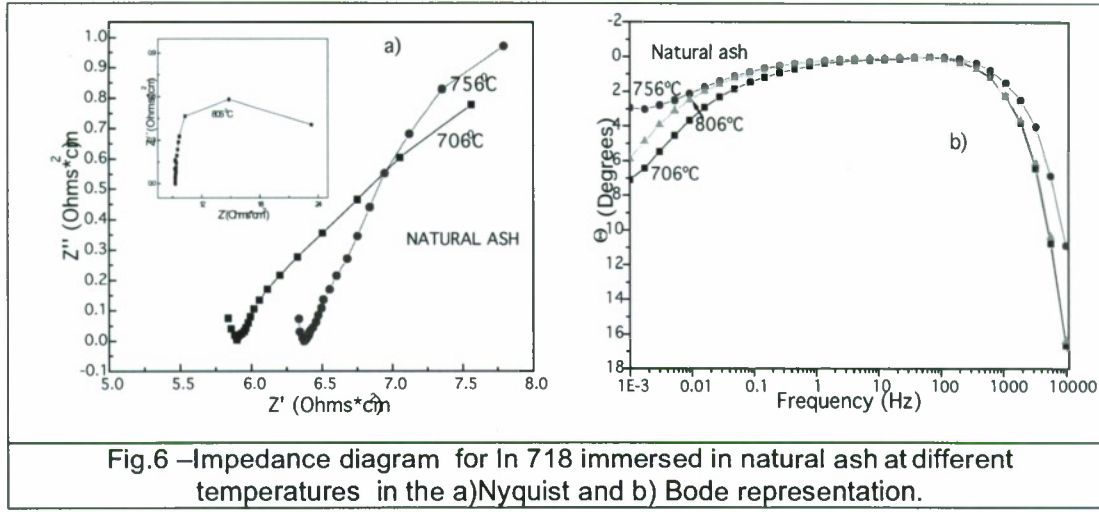


Fig.5 –Impedance diagram for IN 718 immersed in the 80V₂O₅-20Na₂SO₄ mixture at different temperatures in the a)Nyquist and b) Bode representation.

Finally, Fig. 6 a) shows the Nyquist diagram for In 718 exposed to the natural ash at 706, 756 (meeting point) and 806°C. It can be seen that, at 706, 756°C, the data describe a small, high frequency, capacitive-like semicircle and a large low frequency semicircle, with their centers at the real axis and with diameter decreasing with the temperature. The emergence of a large capacitive low frequency semicircle may be related to the formation of a protective scale on the alloy surface. At 806°C, only a semicircle is observed. Thus, it can be seen that the corrosion rate decreases as the temperature increases. The Bode diagram, Fig. 6 b), showed only one peak around 300 Hz at 537°C, but at 637 and 687°C, there seems to be a superposition of two peaks: one at 300 Hz and another one around 1 Hz. The existence of two peaks means that a protective salt layer has been formed on the alloy surface, which could explain the increase in the semicircle diameter in the Nyquist diagrams, and thus, a decrease in the corrosion rate as temperature increases.



Electric circuits can be used to simulate impedance data. Thus, the following elements are to be expected in the equivalent circuit model: R_f represents the resistance of the salt layer, C_f is its capacitance in parallel; R_{ct} represents the charge transfer resistance; W represents the Warburg impedance and C_{dl} represents the double layer capacitance; finally, R_s represents the salt resistance. However, one has to account for the inhomogeneity of the salt film coating system. When a non-ideal frequency response is present, it is

commonly accepted to employ distributed circuit elements in an equivalent circuit. The most widely used is constant phase element (CPE), which has a non-integer power dependence on the frequency. The impedance of a CPE is described by the expression:

$$Z_{CPE} = Y^{-1} (i\omega)^{-n} \quad (1)$$

where Y is a proportional factor, j is $\sqrt{-1}$, ω is $2\pi f$ and n has the meaning of a phase shift [15]. Often CPE is used in a model in place of a capacitor to

compensate for non-homogeneity in the system. This created the overall equivalent circuit model shown in Figure 7

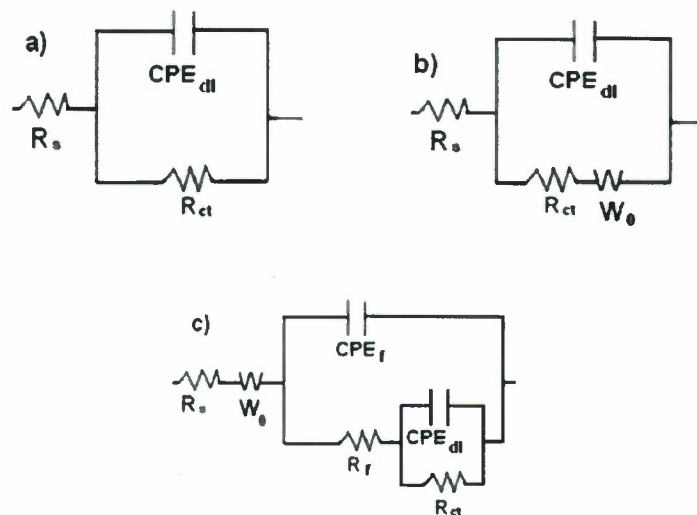


Figure 7. Equivalent electric circuits to simulate the EIS results for IN 718 exposed to molten salts when the corrosion process is a) under charge transfer control, b) when it is under charge transfer and diffusion control, and c) when the alloy is covered with a protective salt layer.

Table 4. - Circuit parameters used for the simulation of the impedance data.

Salt	Temperature (°C)	R_s ($\Omega \cdot \text{cm}^2$)	R_{ct} ($\Omega \cdot \text{cm}^2$)	C_{dl} (F)
Na ₂ SO ₄	842	8.16	311.0	0.00906
Na ₂ SO ₄	892	1.09	145.8	0.012
Na ₂ SO ₄	942	0.62	48.8	0.173
NaVO ₃	579	2.30	193.0	0.044
NaVO ₃	629	2.32	34.7	0.051
NaVO ₃	679	1.41	23.7	0.118
80 wt%V ₂ O ₅ +20 wt%Na ₂ SO ₄	537	2.62	3.25	0.021
80 wt%V ₂ O ₅ +20 wt%Na ₂ SO ₄	587	1.30	3.3	0.14
80 wt%V ₂ O ₅ +20 wt%Na ₂ SO ₄	637	1.91	5.4	0.647
Natural Ash	706	5.89	4.1	3.74
Natural Ash	756	6.39	4.9	7.23
Natural Ash	806	9.21	6.5	0.157

Figure 8 shows a micrograph of IN 718 corroded in pure Na_2SO_4 at 892°C together with elemental energy dispersive spectroscopy (EDS) mappings of Cr, O, Fe, Ni and S. It can be noticed that Cr and O are mainly distributed outside the alloy, perhaps forming a chromium oxide, Cr_2O_3 layer, and that sulphur has penetrated into the alloying, producing internal sulphides. Something very similar can be observed for IN 718 exposed to the natural ash at 756°C , Figure 9, where the distribution of Cr and O outside the alloy is evident, forming, perhaps, a Cr_2O_3 layer, which has been dissolved by the molten ash, since the presence of vanadium inside the alloy is notorious.

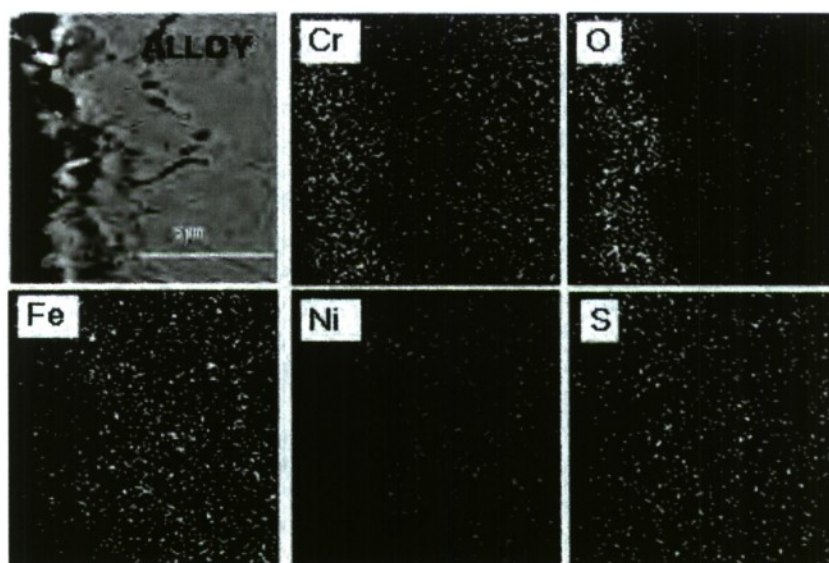


Figure 8. SEM image of IN 718 corroded in Na_2SO_4 at 892°C and EDS map of Cr, O, Fe, Ni and S.

As it can be seen on the X-ray mappings shown on Fig. 9, this oxide layer corresponds to a corrosion product formed mainly by O, Cr and V, and it may be to a compound including chromium oxide Cr_2O_3 , the most common oxide found in Cr-containing alloys at high temperature, and a V-containing compound. Because the corrosion reactions in molten salts are controlled by a process of oxidation of the metal and reduction of the salts, the relative activity of the molten salts with the metal is important, since the corrosion potential of the metal frequently is controlled by the impurities in the molten salt or gas phase,

which increases the rate of cathodic reaction or in the change of the basicity or acidity of the molten mixture. These could make the dissolution of the adherent scale on the metal. The dissolution can be taken by two mechanisms, either by local dissolution or by selective dissolution of the different components of the oxide. In the first case, the growth of the protective oxide will be smaller than in the case of gas corrosion, and the resulting corrosion rate will be bigger. For the other case, if selective dissolution takes place, then the structure and integrity of the scale is damaged by the loss of some elements or components and it is manifested with cracking and spalling of the scale.

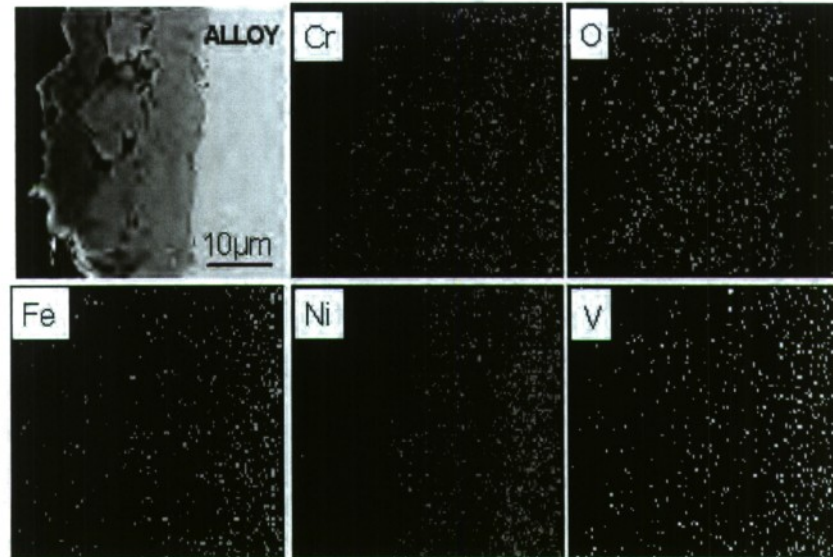
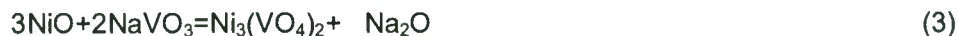


Figure 9. SEM image of IN 718 corroded in Natural ash at 756°C and EDS maps of Cr, O, Fe, Ni and V

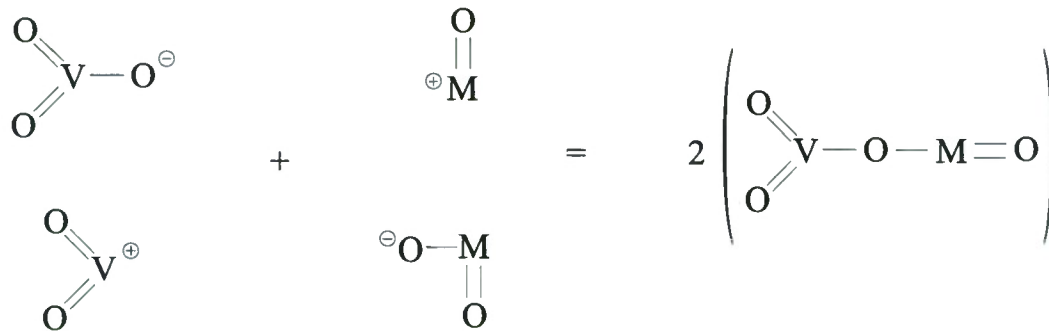
For Cr, the main compounds included both chromium vanadates and chromium oxides, but some other compounds were found such as Fe_2O_3 and NiO . These compounds could have been formed according to next equations:



where the main ion is metavanadate (VO_3^-), which comes from the dissolution of NaVO_3 . However, when V_2O_5 is the corrosive agent, the metavanadate ion is present and the dissociation of V_2O_5 is according to:



Based on this, the dissolution of protective oxides can be explained as:



Thus, the dissociation of V_2O_5 allow us to explain the increase in the corrosion rate due to the fact that the species involved in the corrosion process are metavanadate ions, produced by the dissociation of NaVO_3 according to equations 2, 3 and 4, which do not depend upon the salt basicity, and metavanadate ions and VO_2^+ cation due to the dissociation of V_2O_5 according to equation 5, which do not depend upon the salt basicity. These dissolution reactions could have been destroyed the formed oxides on the alloy surface and induced its destruction at high temperatures. The presence of Na_2SO_4 changes the salt basicity, since this salt has two components: Na_2O (basic) and SO_3 (acidic), the melting point of the mixture, and the corrosion rate. In addition, the presence of sulfur increases the corrosion rate since now there is a new phenomenon, the sulfidation of the alloy. Na_2SO_4 dissolves any formed oxide, either by basic or acidic dissolution, releasing sulfur, which penetrates into the metal, producing internal sulfidation, increasing the corrosion rate.

Based on the above analysis, the corrosion process of IN 718 superalloy into the molten salts may be summarized as follows: the hot corrosion occurred by

oxidation of Ni and Cr at the anodic site and formed Ni^{2+} (NiO) and Cr^{3+} (Cr_2O_3) ions, while at the cathodic site O_2 is reduced to O^{2-} and V^{5+} to V^{4+} . Metal ions like Ni^{2+} and Cr^{3+} react with the oxide ions to form the metal oxides. As a result, the oxygen concentration was increased at the surface of the metal and then oxygen diffused inward and formed oxides. Metal oxides detected by X-ray

diffraction is a clear indication of electrochemical reactions during the hot corrosion process. The presence of VO_2 indicates that vanadium has been reduced from V^{5+} in the NaVO_3 salt to V^{4+} , and it is a strong evidence that the proposed cathodic reaction is taking place, and, therefore It proves, again that hot corrosion of IN 718 alloy is electrochemical in nature. Probably the Cr_2O_3 layer reacted with V and formed a compound, to which C_{ox} and R_{ox} represents. In a series array, a smaller semicircle in the Nyquist plot at high frequency was associated to the alloy corrosion resistance mainly due to activity in the metal scale interface (given by C_{dl} in parallel with R_t).

CONCLUSIONS

The Nyquist plots, in general, present processes in which the activation, charge transfer mechanism was dominant, with the exception of Na_2SO_4 at 842°C and 679°C for NaVO_3 where, in addition to the activation there is also diffusion.

The least aggressive salt was the synthetic Na_2SO_4 salt at temperature of experimentation, while the most aggressive was in the presence of $80\text{V}_2\text{O}_5$ - $20\text{Na}_2\text{SO}_4$ salt.

The corrosion rate in Na_2SO_4 and NaVO_3 increases with increasing temperature around the melting point.

By contrast, in $80\text{V}_2\text{O}_5$ - $20\text{Na}_2\text{SO}_4$ and natural ash, as the temperature rises around the melting point, the corrosion rate decreases. This is due to a change in the basicity or acidity of the salt due to the presence of different ions (VO_3^- , Na_2O , SO_3 , etc.) which increase the salt corrosivity.

REFERENCES

- [1] D. M. Farrell, W.K. Cox, F.H. Stott, D.A. Eden, J.L. Dawson and G.C. Wood, *High Temp. Technol.*, Feb. (1985), 16-21.
- [2] G. Gao, F.H. Stott, J. L. Dawson and D.M. Farrell, *Oxid. Metals*, 33, (1990), p.79.
- [3] Y.M. Wu and R.A. Rapp, *J. Electrochem. Soc.*, Vol. 138, (1991), pp.2683-2690.
- [4] C.Xiang Wu, A. Nishikata and T. Tsuru, *High Temper. Advanc. Mater. and Protec. Coat.*, (1992), pp.221
- [5] Y.M Wu, *Electrochem. Soc. Vol. 138* (1991), pp. 2342
- [6] C.L. Zeng, W. Wang, W.T. Wu, *Corros. Sci. Vol. 43* (2001), p.p. 787
- [7] F.M. Almeraya-Calderon. Ph. D. Thesis. Centro de Investigación en Materiales Avanzados. S. C., Chihuahua, Chi, México. 1998.
- [8]. D. M. Farrell, W.K. Cox, J.L. Dawson, P.D.W. Bottomley, *UK Corrosion 89*, Blackpool, UK (1989).
- [9]. D. M. Farrell, F.H. Stott, G. Rochinni, and A. Colombo, *Mat. High Temp.*, Vol. 10, No.1, (1992), pp11
- [10]. S. Gitangaly, S. Prakash, S. Sing, *Brit. Corrosion J.*, Vol.37, No.1, (2002), pp 56
- [11]. U. Rammelt, L.M. Duc, W. Pleith *J. Appl. Electrochem.* 35(2005) 1225
- [12] A.Wong-Moreno, Y. Mujica-Martinez, L. Martinez, *Corrosion '94, NACE International Paper 185*, 1994, p. 185/1.
- [13] G.W. Cunningham, A.de S. Brasunas, *Corrosion* 12 (1956) 389t.
- [14] W.J. Greenert, *Corrosion* 18 (1962) 575.
- [15] C.L. Zenga,, J. Li., *Electrochimica Acta.* 50 (2005) 5533–5538